Field and Numerical Studies of an Arctic Highway Embankment Compacted with Frozen Fill over Permafrost

by

Aron Piamsalee

A Thesis submitted to the Faculty of Graduate Studies of
The University of Manitoba
In partial fulfilment of the requirements of the degree of

MASTER OF SCIENCE

Department of Civil Engineering
University of Manitoba
Winnipeg

Abstract

Highway embankments in the arctic regions are constructed only in winter because 1) for ease in moving fill materials, 2) to preserve the permafrost, and 3) to minimize environmental impact. This means that the fill is often frozen during compaction. There is uncertainty about the performance of embankments in the arctic regions that are compacted with fill that is initially frozen and then experiences natural thawing during subsequent summers. In addition, typical 'cut and fill' techniques for highway construction are not suitable in the arctic. Avoiding the use of cuts protects permafrost terrain along the highway alignment. To comply with vertical road geometry requirements, embankment fill heights can exceed 10m. High fills cause problems of excessive deformations, side-slope sloughing and embankment cracking. This study aims to improve our understanding on the behaviour of high fill embankments in the arctic.

Research is being undertaken to study the performance of two test sections the newly-constructed Inuvik-Tuktoyaktuk Highway in the Northwest Territories, Canada. Both sections were instrumented with thermistor strings to monitor temperatures at different locations in the embankment fill and foundation soil and ShapeAccelArrays to monitor lateral and vertical displacements at its midslopes. One of these sections is reinforced with layers of wicking woven geotextiles on its side slopes to primarily provide reinforcement against lateral movements and a drainage path for the water during the thawing season. The geotextile has been instrumented with strain gauges to determine the mobilized loads along the length of reinforcement.

This study will only look into the performance of the unreinforced section. Numerical modeling of the embankment temperatures and deformations was calibrated with measurements from the field instrumentation over the first thawing season. The calibrated numerical model was used to investigate important factors affecting the performance of the embankment during and shortly after construction.

Acknowledgements

I would like to thank Dr. Marolo Alfaro for the opportunity to be part of this research project. His technical advice was invaluable over the course of my research. I also like to thank him at a personal level for his encouragement and guidance in my studies.

I would also like to thank my co-advisor Dr. Lukas Arenson for his valuable input and expertise on this research project.

A special thanks goes to my colleague Earl De Guzman, who worked tirelessly on the instrumentation preparation, fieldwork, and laboratory testing as part of this study. Kerry Lynch also provided much needed assistance with the fieldwork at the test site.

Financial support is also acknowledged, via Dr. Alfaro, from the University of Manitoba.

Finally, I would like to acknowledge the support and encouragement received from my family, and especially my wife Vanessa. I truly appreciate their sacrifices, patience, and love throughout.

Table of Contents

List of Figures

List of Appendices

1 Introduction

1.1 Background

Permafrost covers much of northern Canada, including remote areas requiring highway access. Several challenges exist in both the design and construction of highways constructed with frozen compacted fill over areas of permafrost. Design of such highway embankments must consider the risk of permafrost degradation and climate warming. Preservation of the permafrost is an important design principle and can be accomplished through placement of embankment fill to act as insulation to the underlying permafrost. During the thawing season following winter construction, fill materials which were placed and compacted in a frozen state are subject to thawing and undergo thaw settlement. Understanding the magnitude of thaw settlements and lateral movements is invaluable in assessing the stability of the embankment and in determining required fill quantities in new highway constructions.

The need for improved understanding on the factors affecting the performance of embankments constructed using compacted frozen fill in regions of continuous permafrost is the focus of this study.

1.2 Study Overview

The focus of this study is the instrumented sections of the Inuvik-Tuktoyaktuk Highway in the Northwest Territories. Temperatures and deformations of the embankment were recorded and analysed over the first thawing season following the embankment construction.

The research program consisted of 1) construction and instrumentation of the test embankment, 2) data collection, 3) laboratory testing, 4) review of the project setting and environment, and 5) numerical modelling.

1.3 Research Objectives and Scope

The primary goal of the ITH study is to improve the understanding of the processes related to the performance of embankments constructed using compacted frozen fill in regions of continuous permafrost.

The following objectives were identified to meet this primary goal:

1) Construction of test sections, installation of instrumentation and monitoring.
2) Estimate the dry density of the embankment fill compacted in a frozen state, using observations during construction, laboratory testing, and literature review.
3) Develop and calibrate numerical models with field data and laboratory test results.
4) Investigate important factors affecting the performance of the embankment during and shortly after construction.

Given the uniqueness of the ITH test site as an instrumented highway embankment constructed with frozen fill in an area of continuous permafrost, a secondary goal of this thesis was to establish a baseline of information for ongoing current and future research at this site. This includes the information presented in this thesis on the characterization and background information related to the test site, as well as details on construction and instrumentation of the embankment. Electronic files made by the author but not included in this thesis including construction CAD drawings, instrumentation details, photographs, and numerical models have been provided to the author's supervisor, Dr. Marolo Alfaro. It is hoped that ongoing and future research by others will build upon and improve on the understanding gained as part of this study.

The scope of this thesis is limited to a review of background information from the site and surrounding area, observations made during construction, and data acquired from the instrumentation. While the test embankment included both geotextile-reinforced, and unreinforced (control) test sections; this thesis focuses only on the control test section without geotextile reinforcement. Secondly, this research focuses only on the performance of the test embankment during the first thawing season following construction of the test embankment, and does not include numerical modelling nor analysis of data collected after

that period. Finally, the research only focuses on the component of deformation associated with thaw consolidation, and does not include a review of creep deformation associated with the frozen soils.

1.4 Thesis Organization

This thesis is organized into 7 chapters including this introduction. Chapter 2 consists of a literature review to provide background information and assists in the comprehension in the remainder of this thesis. Justification for research is also provided at the end of the chapter. Chapter 3 discusses the field study including details of the embankment and the project setting. Chapter 4 discusses the laboratory testing that was conducted on the soil samples recovered from the field investigation. Together with a review of laboratory test results from literature, important properties of the embankment fill are estimated. Chapter 5 analyzes the instrumentation data collected from site. Chapter 6 consists of the thermal and deformation modelling of the embankment. Chapter 7 includes a summary of the work completed, conclusions made from the study, and recommendations for future research.

2 Literature Review

2.1 Introduction

This chapter includes background information on different aspects of frozen soil including permafrost and the ground thermal regime, heat transfer, mechanical behaviour, compaction and thaw settlement characteristics. The literature review section ends by describing some cold regions construction challenges and practices, and a justification for the current research. While the chapter is intended to guide the chapters to follow, it also includes specific references to be looked back upon from the later chapters.

2.2 Frozen Soil and Permafrost

Soil in a frozen state is a complex, multiphase system of various constituents. The primary constituents in frozen soil are the solid mineral particles, ice, liquid water, and gases. The behaviour of frozen soils is influenced by the physicochemical properties of those constituents, and the complex interactions between them. Included in the many factors affecting the behaviour of frozen soils are particle mineralogy, particle size, specific surface area, temperature, and ice content (Tsytovich, 1975, pp. 21-23), (Andersland & Landanyi, 2004, pp. 110-111).

Ground that is perennially frozen is termed permafrost, and is formally defined as ground that remains at or below 0 °C for at least two years (French, 1996). Permafrost exists over vast areas of the globe, concentrated primarily surrounding the north and south poles, and in high altitude regions as alpine permafrost (French, 1996). Within a region, permafrost can be characterized as “continuous”, meaning it occurs everywhere within that region; or as “discontinuous”, meaning it occurs only in some areas (Andersland & Landanyi, 2004). The research site location falls within a region of continuous permafrost.

2.3 Ground Thermal Regime

A typical ground temperature profile in a region of continuous permafrost is shown in Figure 2-1. Temperature fluctuations at the earth's surface are related to the diurnal and seasonal temperature changes (Pollack, 1993). The maximum and minimum temperatures at ground surface are represented by T_{max} and T_{min} in Figure 2-1. As heat from the surface is transferred to the ground, the amplitude of temperature variations at the surface diminish exponentially with depth (Pollack, 1993). The limits of the annual maximum and minimum temperatures with depth create what is known as a "trumpet curve". The point at which surface temperature fluctuations are no longer observed is termed the *depth of mean zero annual amplitude* (DMZAA). Values for the typical DMZAA have been reported within ranges from 10 to 20 m (Farouki, 1986), (Pollack, 1993), (Andersland & Landanyi, 2004).

The active layer is the zone near the ground surface which experiences freezing and thawing annually. The thickness of the active layer can vary from 15 cm to over 1 m (Andersland & Landanyi, 2004). Below the active layer is the permafrost, which remains perennially frozen. As shown in Figure 2-1, annual temperature fluctuations can still occur within the permafrost layer, above the DMZAA. Below the DMZAA, ground temperatures increase with depth due to heat from the earth's interior, quantified as the geothermal heat flux, Q. The rate of temperature increase with increasing depth is defined as the geothermal gradient, dT/dz. At depth, the temperature eventually reverts above 0 °C, representing the bottom of the permafrost layer. The thickness of the permafrost layer can range from as little as several centimetres to several hundred metres (Andersland & Landanyi, 2004).

A linear geothermal gradient is indicative of a stable energy balance, while departures from linearity are indicative of climate change. A study of deep borehole temperature data in areas of permafrost along the Alaskan arctic coast showed the presence of climate warming, as evidenced by non-linear temperature profile in the upper 100 m (Lachenbruch & Marshall, 1986). Climate change is further discussed in section 3.2.3.2.

2.4 Heat Transfer in Frozen and Unfrozen Soils

2.4.1 Mechanisms of Heat Transfer

The predominant mechanism of heat transfer through most soils is conduction. Conduction occurs through contacts between solid grains, portions of solid grains and fluid-filled pore spaces in series, or directly through fluid. (Farouki, 1986, p. 6).

Other mechanisms of heat transfer can predominate in very specific conditions, influenced by the soil particle size and degree of saturation. For example, convection by air or water can occur through porous coarse gravel or crushed rock (Johansen, 1975, p. 44).

Advective heat transfer describes the mechanism of heat transfer through the bulk flow of fluid. Advection can dominate heat transfer processes in cases where the flow of water occurs over or through soils. Examples highlighting the importance of advection on the degradation of permafrost have been studied in both natural settings, such as on Bylot Island, Nunavut (Fortier, et al., 2007); and on infrastructure, as in the test embankment constructed in Beaver Creek, Yukon (De Grandpré, et al., 2012). While advection was not deemed a primary mechanism for the thawing of the ITH embankment fill over the first thawing season in this study, advection should be considered in future long term performance studies of the highway embankment, as it can have a significant effect on thawing of permafrost soils.

2.4.2 Key Parameters of Conduction

The governing equations for heat conduction are presented later in the thermal modelling section. The key parameters of heat capacity, thermal conductivity, and latent heat of fusion are reviewed in this section as they relate to heat conduction in the study problem.

Heat capacity is a property representing a material's ability to internally store heat energy, and is quantified by the amount of heat required to raise the temperature of the material by one degree (Johnston, 1981). Materials with a low heat capacity will undergo large temperature changes when a given amount of heat energy is added or removed, while high heat capacity materials will exhibit smaller temperature changes. The heat capacity of a

soil can be directly calculated from the component heat capacities of the soil constituents, and their representative volume or mass fractions.

Thermal conductivity is the property representing the rate at which heat travels through a material. The unique physical and chemical properties of ice and water play an important role in the thermal conductivity of soils in frozen and unfrozen states (Farouki, 1986). Unlike heat capacity, the thermal conductivity of a soil cannot be directly calculated from the thermal conductivities of the soil constituents. This is because the thermal conductivity of soils is also dictated by a variety of other factors including particle shape and gradation, water and ice content, density, and porosity (Farouki, 1986) (Harlan & Nixon, 1978). Soil minerology, notably the quartz content also can have a significant impact on thermal conductivity.

Values for the heat capacity and thermal conductivity of various soil constituents are presented in Table 2-1. As shown, there are considerable differences in the heat capacity and thermal conductivity values amongst the different soil constituents. This provides insight of how changes in temperature, moisture content, and density will affect the overall thermal properties of the soil.

Table 2-1: Heat Capacities and Thermal Conductivities of Soil Constituents

Soil Constituent	Volumetric Heat Capacity [kJ/m³/°C]	Thermal Conductivity [W/m/°C]
Quartz	1930	8.4
Many Soil Minerals (approximate average)	1930	2.9
Soil Organic Matter (approximate average)	2510	0.25
Water (0°C)	4217	0.56
Ice (0°C)	1881	2.21
Air (10°C)	1.25	0.026

Values from (Andersland & Landanyi, 2004) and (Farouki, 1986)

For example, since the volumetric heat capacity of water is higher than ice, more heat is required to increase the temperature of a given volume of thawed soil compared to a frozen soil. Similarly, moist soils will tend to have higher heat capacities than dry soils, because of the contribution of water's high heat capacity; and densely compacted soils will tend to have higher heat capacities than loose soils, because of the much higher heat capacity of soil minerals compared to air.

Thermal conductivities of frozen soils will generally be higher than unfrozen soil, because of the higher thermal conductivity in ice compared to water. As previously mentioned, factors beyond the constituent thermal conductivities affect a soil's overall thermal conductivity. Heat conduction through soil relies heavily on contact between the soil particles. The thermal conductivity is thereby increased when interparticle contacts are enhanced by the presence of adsorbed pore water or ice at the contact points, and tight packing of the particles. The addition of fines to a granular soil can also increase the soil's overall thermal conductivity by creating a thermal bridge between the larger granular particles (Farouki, 1986).

Average thermal conductivities for unfrozen and frozen soils as a function of water content and dry density were developed by Harlan & Nixon, based off earlier experimental studies by Kersten (1949) (Harlan & Nixon, 1978). The relationships are presented graphically in Figure 2-2 for sand and gravel, Figure 2-3 for silt and clay, and Figure 2-4 for peat.

Latent heat of fusion is the amount of heat energy absorbed during the phase change from solid to liquid. The latent heat of fusion of water is 337.7 kJ/kg, representing the amount of energy required to melt ice to water (Andersland & Landanyi, 2004, p. 52). The implication for frozen soils is that at ground temperatures just below 0° C, a considerable amount of energy is required to thaw the soil, with little result in temperature change. Similarly, a large amount of energy must first be released by an unfrozen soil before it can freeze. Because many frozen soils are ice-rich, the importance of latent heat effects on the energy balance during phase change is high.

2.5 Mechanical Behaviour of Frozen Soils

The mechanical (stress-strain) properties of ice play an important role in the behaviour of frozen soils. The high strength of cementing-ice bonds contribute directly to the overall strength of frozen soils. Soils in a frozen state are generally very stable, and relatively impervious to groundwater flow which is often useful from an engineering perspective. The range over which pure elastic strain occurs in ice is so low that the magnitude of elastic strain is of little practical importance (Tsytovich, 1975, p. 24). Under compression at high strain rates, the formation of cracks take place, which leads to brittle compressive failure. At lower strain rates, ice undergoes viscoplastic (creep) deformation, which is also influenced by temperature (Schulson, 1999). This overall description of stress-strain behaviour in ice can be described as elastic-thermoviscoplastic.

The scope of this thesis does not focus on stress-deformation of the soil in a frozen state. This is because the magnitude of the thaw settlement in the unfrozen soil is comparatively much more important over the first thawing season. The high strength of frozen soils does however affect the compaction behaviour, which is discussed in the following section.

2.6 Compaction of Frozen Soils

2.6.1 Mechanisms in the Compaction of Frozen Soil

The compaction of soils in a frozen state is much more difficult than in an unfrozen state, and presents a significant challenge to construction in cold regions (Burwash & Clark, 1981). Given the same compactive effort and water content, soils that have been compacted in a frozen state will have a lower dry density, and upon thawing will be more prone to settlement and have lower strength than soils that were compacted in an unfrozen state (Burwash & Clark, 1981).

Compaction of soil, either frozen or unfrozen, is the process of the densification by the rearrangement of soil particles and the expulsion of air (Budhu, 2007, p. 70). Frozen soils resist compaction because of the increase in shear resistance to the rearrangement of the soil particles (Haas, et al., 1978). In addition to the shear strength already present in unfrozen soils, the following mechanisms contribute to the shear strength in frozen soils:

1) pore ice strength; 2) strengthening effects between the soil and ice matrix resisting collapse of the soil skeleton; and 3) effective stress increase resulting from adhesive ice bonds resisting dilation during shearing of a dense soil (Andersland & Landanyi, 2004, p. 107).

The mechanisms listed above, and thus the effectiveness of compaction are affected by a number of factors including ice content, soil particle size, and temperature. Burwash & Clark (1981) show that finer grained soils exhibit a greater reduction in the effectiveness of compaction at freezing temperatures compared to coarse-grained soils. Below 0 °C, lower temperatures result in a decrease in effectiveness of compaction attributed to the increase in the strength of ice at lower temperatures, as well as the decrease in unfrozen water content (most notable in fine grained soils) (Andersland & Landanyi, 2004, p. 114).

As stated, pore ice also affects the effectiveness of compaction in frozen soils. The development of pore ice in frozen soils has been characterized into 4 cases by (Haas, et al., 1978) and is summarized below. These 4 cases of ice development are sketched conceptually in Figure 2-5, and their importance in the compaction of frozen soils is discussed in the following section.

- Case I - Intergranular Contact Only: No ice is present. The resistance during compaction to rearrangement of the soil particles is limited to the relatively low frictional resistance at the contacts between the particles, resulting in a relatively high dry density.
- Case II - Discontinuous Pore Ice: Water accumulates and freezes discontinuously near the intergranular contacts. Any increase of ice at this stage greatly increases resistance to rearrangement of the soil particles.
- Case III - Continuous Pore Ice: All of the intergranular contacts become coated by a continuous layer of ice. Void spaces occupied by air still remain.
- Case IV - Ice Filling Voids: With increasing water content, the air voids are replaced by ice, and the net increase in area of resistance to sliding is only marginally increased at this stage. This results in the reduced slope on the dry density vs. moisture content graph over this range of higher water contents.

2.6.2 Interpretation of Compaction Test Results

The difference in the effectiveness of compaction between unfrozen and frozen soils is exemplified in Figure 2-6 through the moisture-density results of standardized-effort compaction (Proctor) testing on a silty sand soil by (Alkire, et al., 1975). The dashed line indicates the unfrozen compaction results at 20 °C, showing the familiar "Proctor curve" consisting of a concave-down parabola with a well defined maximum dry density and corresponding optimum water content (at 107 p.c.f. and 13.5% respectively in this example). The frozen compaction results at -7 °C indicated by a solid line show a very different response. First, the dry density achieved under the standard-effort compaction is much lower for the frozen soil compared to the unfrozen soil. The magnitude of this reduction is discussed in the following subsection. Secondly, the frozen soil exhibits a bilinear decrease in in dry density with increasing water content.

The nature of this this bilinear decrease can be explained by the 4 cases of pore ice development previously discussed. A close up of a similar set of compaction test results on frozen sands by (Botz & Haas, 1980) is shown in Figure 2-7, with the cases of pore ice development added to the original figure by the author. The point on the curve at 0% moisture content corresponds to Case I, where no pore ice is present and the dry density is the highest. The linear slope extending between 0 and 8% represents Case II, where an increase in pore ice at the intergranular contacts results in a considerable increase in resistance against shearing, resulting in the observed steep decrease in dry density. Near 8% moisture content, this represents the Case III inflection point where all of the intergranular contacts have become coated with ice. The second linear slope extending from 8 to 20% represents Case IV, where the resistance against shearing is marginally increased as the air voids are replaced by ice.

Research on other soil types over a range of particle gradations including silty clay, sandy silt, silty sand, gravelly sand, and gravel have all shown similar behaviours in 1) the reduction in dry density in frozen soils compared to unfrozen soils, and 2) the decrease in dry density with increasing water content in frozen soils (Haas, et al., 1978), (Johnson & Sallberg, 1962), (Burwash & Clark, 1981).

2.6.3 Quantification of Reduction in Compaction Effectiveness

This difference in effectiveness of compaction in Standard Proctor testing, between unfrozen and frozen soils can be quantified using the Standard Proctor Compaction (SPC) ratio. The SPC ratio is defined as the ratio of the soil's frozen dry density to its unfrozen dry density (Burwash & Clark, 1981), typically expressed in percentage form. SPC ratios discussed in literature are generally calculated at a given reference water content equal to the unfrozen soil's optimum water content, however can be calculated for any selected water content. In addition, SPC ratios should be discussed in the context of a reference frozen soil temperature, since this too affects the effectiveness of frozen soil compaction.

SPC ratios plotted vs. temperature are presented in Figure 2-8 for gravel, sand, silt, and clay soil types (Clark, 1970). Note for each soil type, the SPC ratios were calculated at optimum water content. As expected, the SPC ratios were lowest for fine-grained soils and higher for coarse-grained soils. Lower SPC ratios were obtained at colder freezing temperatures (-23 °C) compared to at warmer freezing temperatures (-2 °C).

From the relatively limited literature-base on compaction testing of frozen soils, varying SPC ratio results have been obtained for given soil gradations. Section 4.4 includes detailed comparison of laboratory frozen compaction results on the ITH test site fill material versus comparable soils from literature.

2.7 Thaw Settlement

The thawing of frozen soils often leads to a volume reduction, known as thaw settlement or thaw consolidation. Infrastructure constructed with or resting upon frozen soil, as well as frozen soils in a natural environment can be susceptible to thaw settlement.

There are several mechanisms which contribute to thaw settlement. The first is the change in volume which occurs in the phase change between ice and water[1]. The second is the collapse of the soil skeleton due to the loss of cementing effect of ice between the soil mineral particles. Additional volume change takes place if drainage of meltwater out of the system is also considered (Andersland & Landanyi, 2004, p. 89).

Figure 2-9 illustrates the typical behaviour of a frozen soil under applied pressured during thawing. While frozen, a small decrease in void ratio occurs as a pressure, σ_o is applied (line a-b). Upon thawing (line b-c), the void ratio decreases drastically while the pressure, σ_o is held constant. This is related to the volume reduction from the phase change of ice to water, as well as water being released and squeezed from the pore spaces as stress is redistributed to the soil skeleton (Botz & Haas, 1980). An additional increase in pressure, $\Delta\sigma$ results in further reduction in void ratio (consolidation) (line c-d). (Andersland & Landanyi, 2004, p. 90)

Analytical solutions to calculate thaw consolidation in frozen soils have been developed, most notably the solution presented by (Morgenstern & Nixon, 1971). In their solution, the thawing soil is treated as a one-dimensional consolidation problem with a moving boundary to delineate between the thawed and frozen soil. The theory combines Neumann's theory of heat conduction to define the position of the moving thaw boundary as a function of time, together with Terzaghi's consolidation theory to calculate time dependant settlement within the thawed zone.

In a review of proposed theories on thaw consolidation, (Dumais & Konrad, 2015) identify the importance of Morgenstern & Nixon's theory as a framework for other thaw consolidation theories (including extensions to two and three dimensions) while also identifying limitations in its applicability to certain real-world problems. Morgenstern & Nixon (1971), acknowledged the theory's limitation towards frozen soils high in ice

[1] The volume occupied by ice is approximately 9% greater than the same mass of liquid water. (Farouki, 1986)

content. In ice-rich soils where the soil skeleton is supported by an ice-matrix as opposed to intergranular contacts, thaw consolidation theories described above will underestimate the settlement upon thawing (Dumais & Konrad, 2015). Furthermore, as the theories rely on Terzaghi's consolidation theory, they are not applicable to soils below 100% saturation.

Because of the lack of suitable alternative thaw consolidation models for low-saturation yet ice-rich soils, a linear-elastic constitutive model was used to simulate deformation of the thawed embankment fill and is presented in section 6.3.

Alternative methods to estimate thaw settlements based on experimental results, (Luscher & Afifi, 1973) and (Speer, et al., 1973) may be more appropriate to estimate thaw settlements in ice rich soils. The experimental results by (Luscher & Afifi, 1973) from a series of tests on silty sand soils are shown in Figure 2-10, and are later compared to the measured thaw settlement results from the test site in section 5.1.3.

2.8 Cold Regions Construction Challenges, Practices, and Design

Many challenges exist for construction in cold regions. General challenges include working in cold weather, general lack of infrastructure and transportation, difficult terrain, shortened construction season, and environmentally sensitive areas (Johnston, 1981). A variety of technical challenges also exist related to the construction of embankments in cold regions. This section highlights some of those technical challenges, alongside construction practices and design principles used.

Preservation of the permafrost is an important design principle (Cheng, et al., 2004). For the Inuvik-Tuktoyaktuk Highway, the highway embankment serves as an insulator to protect the underlying permafrost, as will be discussed. Alternative passive cooling methods to protect permafrost from degradation beneath transportation infrastructure include air convection embankments, air ducts, heat drains and thermosyphons, sun-sheds, and high-albedo surfacing (Doré, et al., 2016).

As discussed earlier, there is considerable difficulty in the compaction of frozen soils. This can lead to inadequate compaction later resulting in excessive thaw settlement. In highway embankments, thaw settlement at the embankment toe can lead to longitudinal cracking

along the edge of the road surface, necessitating re-surfacing maintenance or leading to instability of the embankment (Andersland & Landanyi, 2004, p. 251).

Often, the use of frozen fill material is prohibited because of the resulting low strength and settlement that occur upon thawing (Graham, et al., 1988). Where available, sands and gravel can be compacted while frozen if sufficiently dry (water content below 1%) (Johnston, 1981). Chemical additives can also be added to lower the freezing point of the pore fluid in the soil (Haas, et al., 1978).

While relatively homogeneous water contents can be achieved in soils during warm-weather construction (by adding water or drying by disking); this is not possible with cold-weather construction (Botz & Haas, 1980). In addition, frozen soils can possess a very wide range of water contents due to ice lensing or massive ice, whose presence can be difficult to predict/evaluate. Where ground ice is present within granular deposits, removal of the ice by thawing is sometimes required. This is conducted by stripping and allowing natural thawing of the granular deposits, followed by windrowing or stockpiling the materials to allow for drainage of excess moisture (Gowan & Dallimore, 1990).

2.9 Justification for Research

Permafrost covers significant portions of the globe, including a large portion of northern Canada. Highway access in the north is required for several reasons including economic development, access to natural resources, and reinforcing Canadian sovereignty objectives (De Guzman, et al., 2015). These areas requiring highway access are often remote, requiring significant stretches of highway to connect them.

Highway embankment design geometry, and associated costs for construction and maintenance are multiplied over the many kilometers of highway infrastructure. Improved understanding on the processes related to the performance of highway embankments permitting for even small changes in construction or maintenance requirements could have significant impacts on costs of these highways. Due to the comparatively small number of completed highways built with frozen fill in areas of permafrost versus conventional highway construction, global expertise in the design and construction of such highways is

also comparatively limited. Design of highway embankments over permafrost necessitates special care due to the sensitivity of permafrost and risk for permafrost degradation. Further design considerations are required to accommodate climate warming.

The need for research on the behaviour of frozen soils subjected to thawing has been identified (Dumais & Konrad, 2015), (Graham, et al., 1988), (Kurz, et al., 2018), (and various others cited in this thesis). This includes a broad range of topics including construction, laboratory testing, numerical modelling, and theory development.

More specifically, following completion of the Dempster Highway, (Lingnau, 1985) identified the necessity for research on the settlement and thermal regime of similar highway embankments constructed in permafrost areas. While some field studies have been conducted on embankments in permafrost areas, the specific need for research on newly constructed embankments over permafrost, which have not yet reached thermal equilibrium was identified (Darrow, 2011).

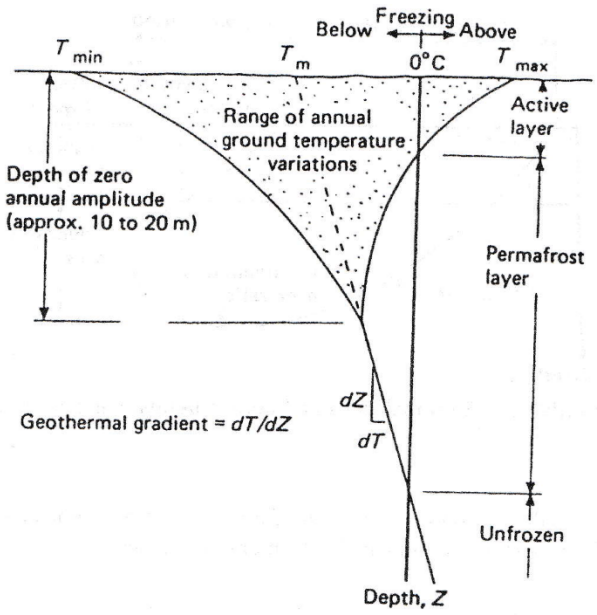

Figure 2-1:Typical Ground Temperature Profile in Perennially Frozen Soil
Permission obtained from (Andersland & Landanyi, 2004)

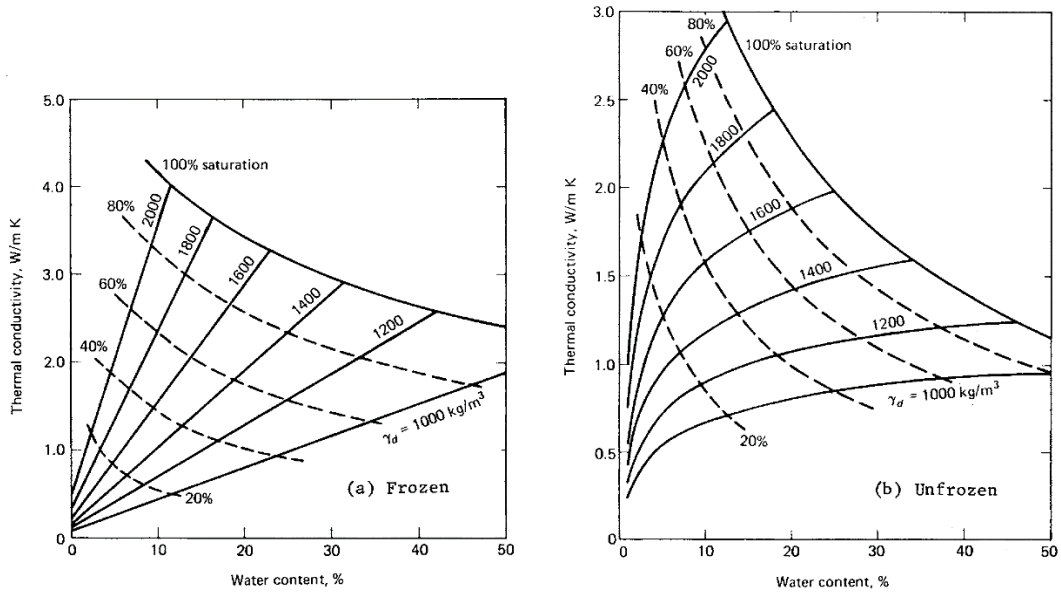

Figure 2-2: Average Thermal Conductivity of Sand and Gravel for a) Frozen, and b) Unfrozen cases
From Harlan & Nixon, Geotechnical Engineering for Cold Regions (Chapter Three), ©1978, reproduced with permission of McGraw-Hill Education.

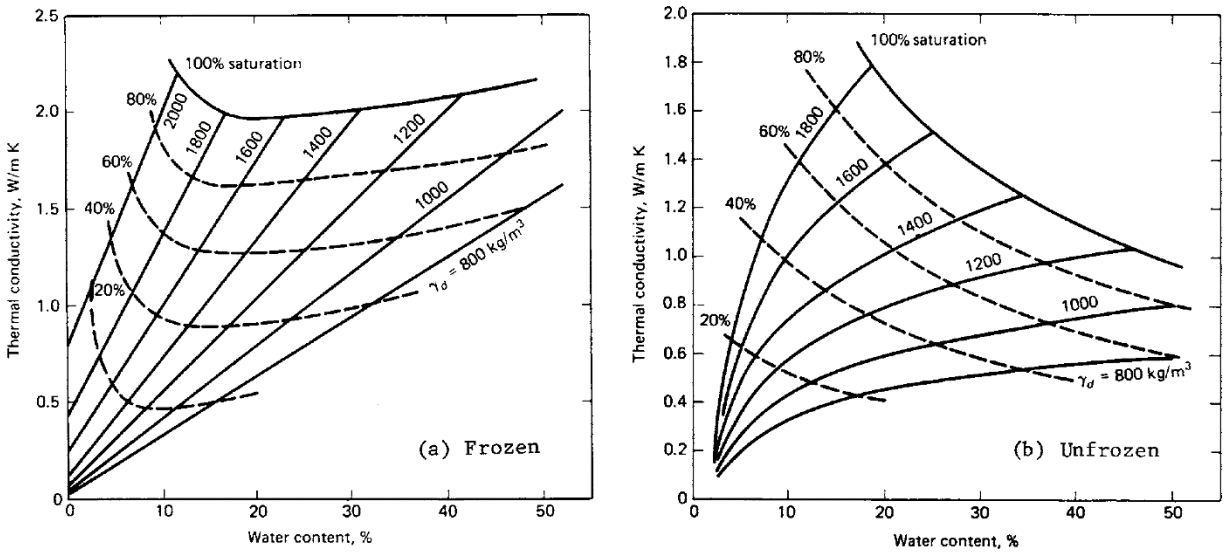

Figure 2-3: Average Thermal Conductivity of Silt and Clay for a) Frozen, and b) Unfrozen cases
From Harlan & Nixon, Geotechnical Engineering for Cold Regions (Chapter Three), ©1978, reproduced with permission of McGraw-Hill Education.

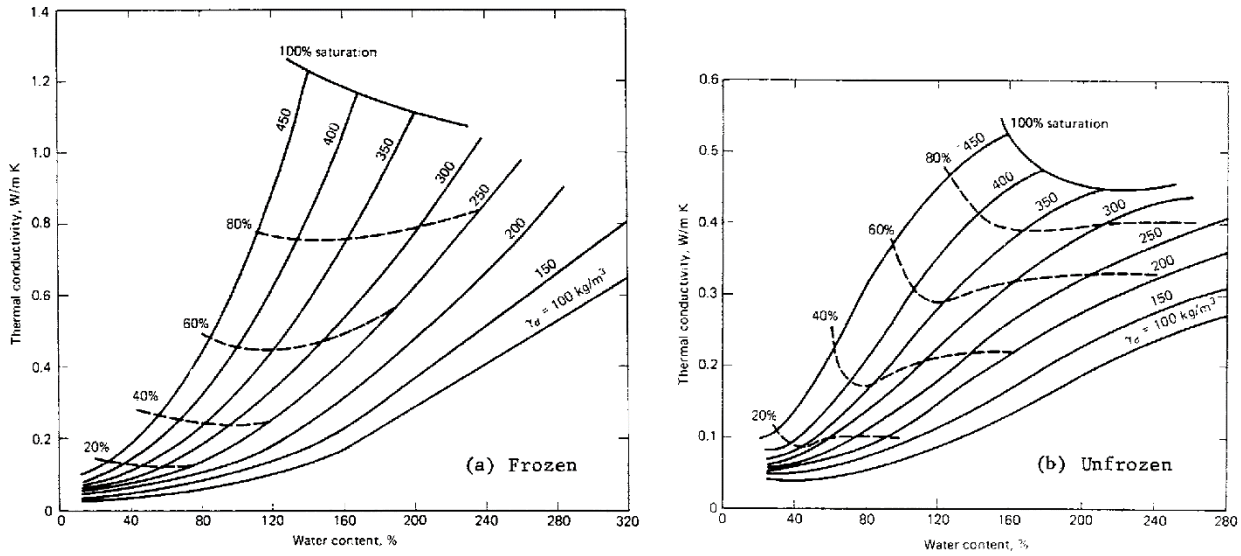

Figure 2-4: Average Thermal Conductivity of Peat for a) Frozen, and b) Unfrozen cases
From Harlan & Nixon, Geotechnical Engineering for Cold Regions (Chapter Three), ©1978, reproduced with permission of McGraw-Hill Education.

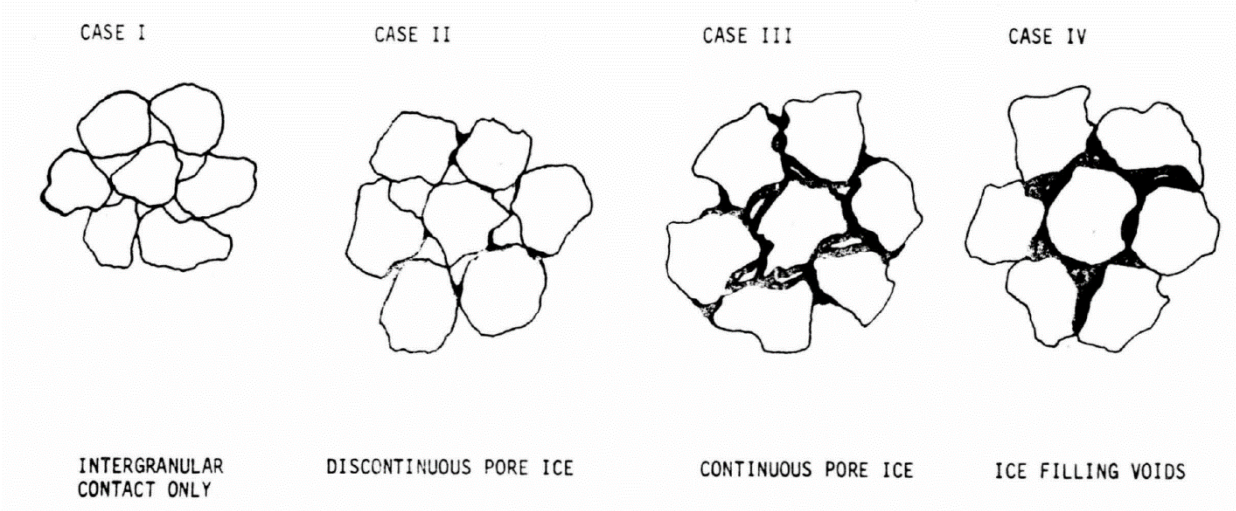

Figure 2-5: Development of Pore Ice with Increasing Water Content
Obtained from (Haas, et al., 1978), government publication

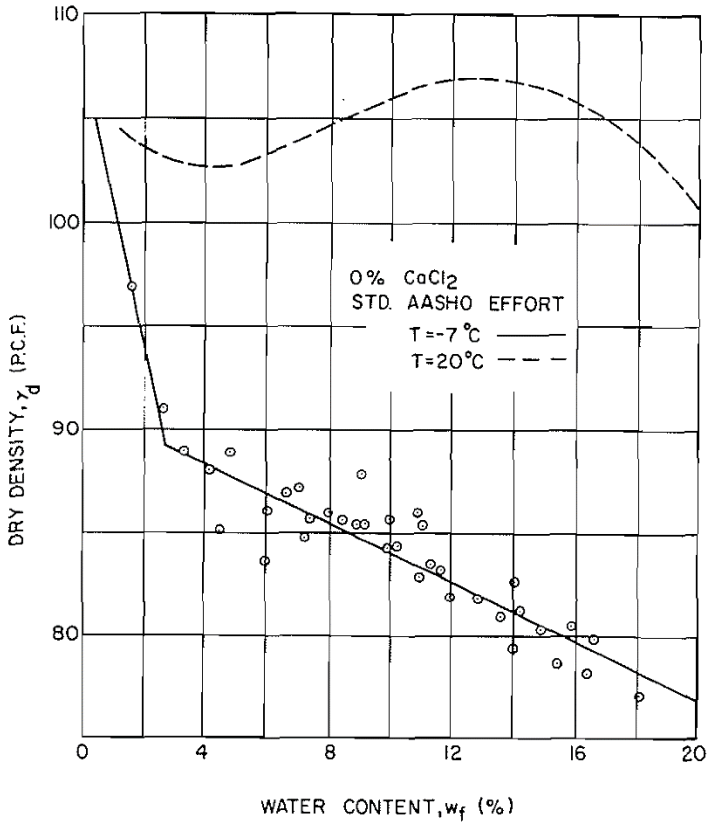

Figure 2-6: Typical Moisture-Density Relationship in both Unfrozen and Frozen Soils
Permission obtained from (Alkire, et al., 1975)

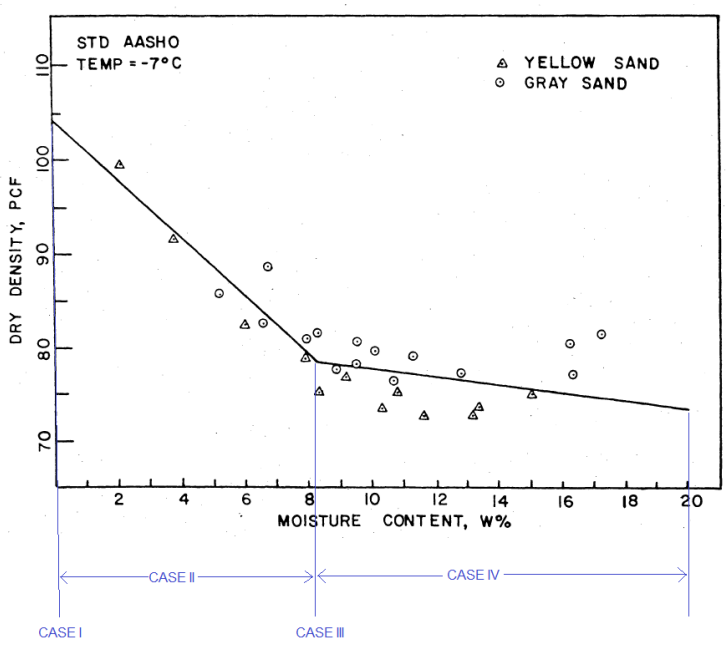

Figure 2-7: Typical Moisture-Density Relationship for Frozen Soil
Obtained from (Botz & Haas, 1980), government publication

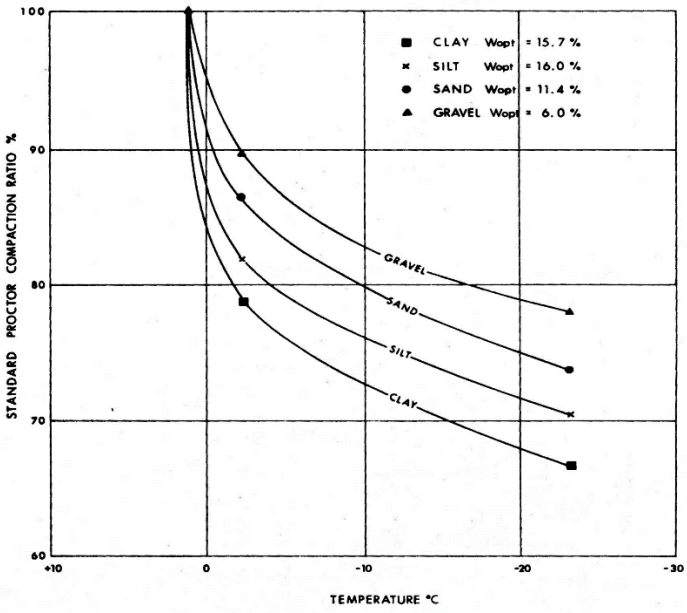

Figure 2-8: Standard Proctor Compaction Ratio vs. Temperature for Four Soil Types
Obtained from (Clark, 1970)

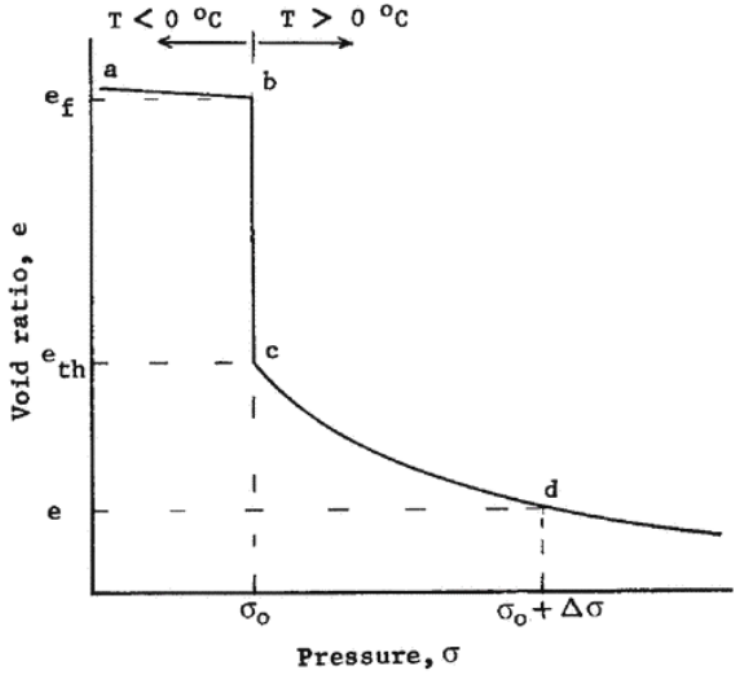

Figure 2-9: Typical Thaw Settlement Curve for Frozen Soils Subjected to Thawing
Permission obtained from (Andersland & Landanyi, 2004)

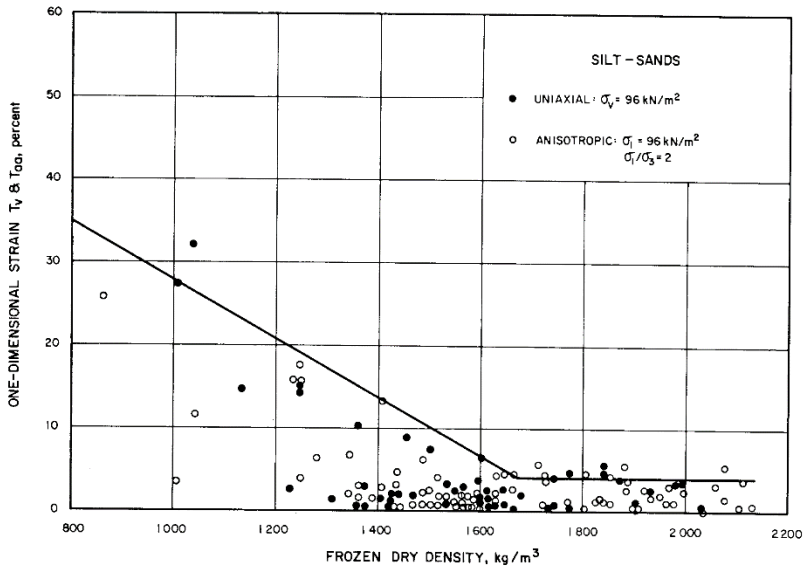

Figure 2-10: Experimental Thaw Consolidation on Frozen Silt-Sands
Obtained from (Luscher & Afifi, 1973), government publication (Vertical Axis shows Volumetric Strain for Uniaxial tests, and Axial Strain for Anisotropic tests; with a single trendline to represent the two datasets)

3 Field Study

3.1 Inuvik-Tuktoyaktuk Highway Project Overview

The Inuvik-Tuktoyaktuk Highway is a 138 km highway between the Town of Inuvik, and the Hamlet of Tuktoyaktuk in the Northwest Territories. The concept for an all-season road first began in the 1960s, with interest over the years coming from local residents and the the oil and gas industry. (Government of Northwest Territories, 2017)

The Inuvik-Tuktoyaktuk Highway (ITH) represents Canada's only all-season road with access to the Arctic Coast. Prior to completion of the highway, primary modes of transport from Inuvik to Tuktoyaktuk were via the Mackenzie River (by barge in summer months, or ice road in winter months), or by air (Government of Northwest Territories, 2017). The connection from Inuvik to Canada's highway system to the south is via the Dempster Highway, which was fully completed in the late 1970's, connecting Inuvik to Dawson City; a distance of 743 km (Lingnau, 1985). Design principles and construction challenges on the Dempster Highway, were similar to those involved on the Inuvik-Tuktoyaktuk Highway.

The key concept in the design of the Inuvik-Tuktoyaktuk Highway was preservation of the underlying permafrost. Conventional highway construction practices involving stripping of surficial organic soil, as well as typical "cut and fill" operations to optimize imported fill volume requirements were avoided on this project since the removal of insulating peat and disturbance to surface soils and would lead to further degradation of permafrost. To protect the permafrost, the highway design consisted of fill placement directly upon the undisturbed native soil surface. The embankment fill acts as insulation with the intent of maintaining the native subgrade soils in a frozen state. The embankment height over the length of highway is typically 2 m, with some sections (including the test site study location) requiring thicknesses up to 6m to satisfy line-of-sight requirements due to undulating terrain.

The highway alignment is shown in the Construction Plan Atlas Overview included in Appendix A. The design of the highway consists of an 8 to 9 m wide, two-lane, gravel surfaced roadway, with 3:1 side-slopes (Government of Northwest Territories, 2017).

A woven geotextile fabric was placed between the native soil and fill material to act as a separator. (Government of Northwest Territories, 2017). The purpose of the geotextile separator is to avoid the loss of aggregate into the underlying soft peat soils.

Fill material for construction of the highway was sourced from a number of borrow areas located along the highway alignment (shown in Appendix A). These borrow source locations were identified through terrain mapping and subsequent geotechnical investigations.

A key constraint in both the design and construction of the highway was the short construction season, which was generally limited to the coldest months of October to April[2]. This was required to:

- Allow use of the winter road for movement of construction and support equipment to the work areas.
- Allow rubber-tire and track-mounted construction and support equipment relatively easy access over the frozen ground and lakes.
- Minimize environmental damage to the sensitive tundra vegetation.

Construction was undertaken by independent crews from both the north and south ends of the highway, eventually meeting one another. Construction began in January of 2014 and was completed in November 2017.

Locations on the highway are identified by their stationing, or kilometer post number. Stationing begins at kilometer post 0 at the Inuvik end of the highway, and increases to

[2] Exact start and end of construction seasons were dependant on timing of freeze-up and thawing. Construction of the southern portion of the highway was extended slightly longer than the northern portion, since access did not rely on the winter road.

kilometer post 134.2 at the Tuktoyaktuk end. The embankment test site is located at approximately station 82+400, or a distance of 82.4 km along the highway north of Inuvik. The coordinates of the test site are 69° 1' 5" N, 133° 16' 6" W (UTM coordinates 8W 569195 m E, 7657343 m N). The site is 12.5 km WNW of Parsons Lake, and 1.5 km E of the northwest shore of the southernmost of the two Husky Lakes (formerly known as the Eskimo Lakes). Many smaller, unnamed lakes are located in the vicinity of the test site. A satellite image at the location of the test site is shown in Figure 3-2. Additional design and construction details specific to the test embankment are covered in section 3.3.3.

3.2 ITH Project Setting

3.2.1 Physiography and Geology

The test site is situated in the physiographic region known as the Tuktoyaktuk Coastlands, which is shown in Figure 3-1 from (Rampton, 1988). Acknowledgement is provided to the late J. Ross Mackay whose research on the western Canadian arctic, and notably the Tuktoyaktuk Coastlands began in 1951, and continued without interruption between 1954 and 2011 (Burn, 2015). His research provides the basis for much of our current understanding of the region.

The Tuktoyaktuk Coastlands are bordered by the Beaufort Sea to the north, and the physiographic regions of the Mackenzie Delta to the west, and by the Anderson Plain to the south and west. The geology of the Tuktoyaktuk Coastlands is characterized by thick unconsolidated sediments deposited during the Pleistocene epoch[3] (Rampton, 1988). The region includes areas of poor drainage and is dotted with lakes, covering over 15 % of the surface area (Mackay, 1963), and commonly about 30 % (Rampton, 1988). Irregular drainage patterns also occur because of the presence of thermokarst activity. Geologic

[3] The term "Pleistocene Coastlands" was used to describe the area of "Tuktoyaktuk Coastlands" in earlier research by J. Ross Mackay.

features such as massive ice, retrogressive-thaw slides, and pingos are common in this region (Rampton, 1988).

Mackay's extensive studies further identified several distinct sub-regions within the Tuktoyaktuk Coastlands region. The test site falls within the Morainic Hills sub-region, as categorized by (Mackay, 1963). Later studies by (Rampton, 1988) make a further distinction by dividing and renaming the Morainic Hills sub-region into two; termed the Parsons Lake Plain, and the West Tuk Peninsula Axis, with the test site falling within the latter sub-region (as shown in Figure 3-1). The West Tuk-Peninsula Axis consists of poorly-draining lakes interspersed between low hills, which form a drainage divide between the Husky Lakes to the southeast, and the Beaufort Sea (Kugmallit Bay specifically) to the northwest. Many hills are capped with deposits from the later Pleistocene epoch, consisting of glacial till or glaciofluvial sediments later in the Pleistocene epoch. These Pleistocene deposits generally consist of gravel and sand-sized particles (Mackay, 1963), (Rampton, 1988).

Surficial geology maps by (Rampton, 1987) provide further refinement of surficial conditions within the West Tuk Peninsula Axis sub-region, and surrounding areas. The maps indicate the test site lies in an area categorized as glaciofluvial outwash from the early Wisconsinian glaciation, consisting of sand and gravel typically between 3 and 30 m in thickness.

Underlying the Pleistocene deposits, the geology consists of strata of clastic deposits extending approximately 6000 m at the location of the test site (Yorath, 1980).

The uppermost stratum is the Pliocene-Pleistocene Iperk sequence, formed of sand and gravel. The sequence has a high porosity, contributing to a high ice content and thermal conductivity (Allen, et al., 1988). Massive ground ice has been found to occur commonly in conjunction with granular deposits in the Tuktoyaktuk Coastlands region (Gowan & Dallimore, 1990). Allen et al. demonstrate the correlation between the thickness of the thermally conductive Iperk sequence and the presence of deep permafrost. At the test site, the Iperk sequence extends to about a 200 m depth, and the permafrost to a depth of approximately 310 m. Throughout the region, permafrost depths range from in excess of

700 m in the northeastern portion of Richards Island, to less than 100 m in the Mackenzie Delta (Allen, et al., 1988).

It should be noted the delineation between the Pleistocene deposits and the underlying Iperk sequence is not completely understood within the field of geology. The maps by (Yorath, 1980) indicate the presence of strata of unknown age at the underside of the Pleistocene deposits in the central and northeastern Tuktoyaktuk Peninsula. It is also noted by (Mackay, 1963) that pre-Pleistocene sediments may underlie portions the Morainic Hills sub-region. Despite this uncertainty, it can however be summarized that within the upper 200 m, the local geology consists of sand and gravel sized particles with the presence of ground ice very likely.

At the location of Pit 174 the surficial geology is categorized as glaciofluvial ice contact deposits from the early Wisconsinian; including eskers, kames, kame and kettle complexes, and some thermokarst-modified outwash plains (Rampton, 1987). Geologists from the NWTDOT identified the borrow areas along this portion of the ITH (including Pit 174) to likely consist of kame deposits[4] Massive ground ice was frequently encountered during the exploratory drilling of these deposits, and was also visible in some areas of the borrow pits during extraction of the fill from the deposits.

3.2.2 Vegetation

The physical structure of vegetation influences the microclimate and energy balance at the ground surface by altering snow accumulation, surface drainage, and wind velocities (Burn & Kokelj, 2009), (Harlan & Nixon, 1978, p. 123).

[4] From personal discussions with NWTDOT geologists, while the author worked on the ITH borrow source investigation programs in February to March 2014 logging and sampling potential borrow sources.

The test site location falls within the "low arctic tundra" region described by (Mackay, 1963) and summarized by (Burn & Kokelj, 2009) consisting of:

- hummocky terrain, with drier uplands and poor-draining interhummock areas
- grasses and lichens in drier areas
- mosses and ericaceous (disliking alkaline soil) shrubs in poor-draining areas

This is consistent with the mosses and small shrubs observed on site during construction where snow was cleared to create a working area (as shown in Photo 10 of Appendix B), as well as site photos 23 to 25 taken in July following snowmelt. During drilling of the low-lying embankment toe area, the surface vegetation generally consisted of 10 to 30 mm of living moss, overlying dead and decaying peat to a depth of approximately 200 mm.

The characterization summarized by (Burn & Kokelj, 2009) above, along with the site observations closely match the "Moist Acidic Tundra" land-cover, as described by (Klene, et al., 2001) in their study of land-cover classes at sites in the Kuparuk River Basin in northern Alaska. Their research highlights the significance of *Sphagnum* mosses on the energy balance in the "Moist Acidic Tundra" environment. This includes the ability to provide insulating effects, affect heat adsorption due to its colour, and promote saturated conditions and thus increase evapotranspiration. (Klene, et al., 2001) calculated n-factors specific to the "Moist Acidic Tundra" environment, which have been used in the thermal model discussed in section 6.2.5.2.

3.2.3 Climate

3.2.3.1 Regional Climate

The climate of the Tuktoyaktuk Coastlands region has been characterized in detail by (Rampton, 1988). The test site lies in the zone of transition between the "arctic coastal" and "continental subarctic" climate zones. Temperature and precipitation records from Tuktoyaktuk are considered typical of the arctic coastal climate, while Inuvik is typical of the northern portion of the continental subarctic climate zone (Rampton, 1988). Both

regions experience cold, dry winters and cool summers. During summer, more rain falls in the southern, continental zone surrounding Inuvik than along the northern coastline near Tuktoyaktuk (Dyke, 2000).

Given the location of the test site, it is reasonable to expect the climate at the test site to fall between that experienced in Tuktoyaktuk and Inuvik. Monthly temperature normals from the Tuktoyaktuk and Inuvik climate stations are shown in Figure 3-3. As can be seen, average monthly temperatures are very similar at the 2 locations from October to January, but are 2 to 4 °C warmer in Inuvik from February to September. (Meteorological Service of Canada, Environment and Climate Change Canada, 2017)

Two additional climate stations were investigated to obtain the most representative climate dataset for the test site location. The Storm Hills and Trail Valley climate stations are situated in remote, uninhabited locations 29 km WSW, and 31 km SSW from the test site respectively. Their locations are included in Figure 3-1. Climate data from all 4 stations was downloaded from the Government of Canada's online records (Government of Canada National Climate Services, 2016). Over the thawing season study period, the climate station temperatures ranked from warmest to coolest were generally: Inuvik, Trail Valley, Tuktoyaktuk, and Storm Hills.

Of the 4 climate stations, Trail Valley was selected as the most representative climate station for the test site. This was chosen because of its proximity to the test site, while also falling within the same physiographic region (Tuktoyaktuk Coastlands) as the test site as shown Figure 3-1. While the Storm Hills climate station is slightly closer to the test site, it falls within a different physiographic region (Anderson Plain), and has unusually low temperatures likely due to its position atop hills at much higher elevations than the surrounding area. Temperature data from the Trail Valley climate station used in the thermal modelling is discussed in section 6.2.5.1.

Thawing and freezing indices are used to quantify the duration and intensity of temperature variations, over a given thawing or freezing season (French, 1996). The thawing index represents the sum of all thawing degree-days over a thawing season. Similarly, the freezing index is the sum of the freezing degree-days over a freezing

season. The thawing and freezing indices calculated using air temperatures are termed air thawing and freezing indices, while thawing and freezing indices calculated using ground surface temperatures are termed surface thawing and freezing indices. The 3-year average air thawing index at the Trail Valley climate station was calculated as 1179 °C*days, and the air freezing index was 3967 °C*days. Air thawing and freezing indices are further discussed in section 6.2.5 as they relate to estimation of surface temperatures through the use of n-factors.

No formal snow depth recordings were collected over the study period, which was concentrated over the thawing season. The insulating effects of snow can however have an important impact on the ground thermal regime. In the Mackenzie Delta Area, the lack of substantial snow-holding vegetation in the tundra results in thin snow cover at topographic high points, and the formation of drifts in low-lying areas (Burn & Kokelj, 2009). This phenomenon was observed at the low-lying toe area of the test embankment, where the snow depth at start of April 2015 construction was estimated to vary between 0.5 and 1 m. The snow depth measured at the embankment toe near the end of the 2016 winter season was approximately 600 mm.

3.2.3.2 Climate Change in the Northwestern Arctic

Climate change has become a topic of increased concern over recent decades. Some of the largest increases in surface air temperatures observed globally since the 1960's have occurred in the northwestern portions of North America, especially between latitudes of 40° and 70° (Serreze, et al., 2000). Figure 3-7 shows average annual temperatures in Inuvik from 1961 to 2005. The average air temperature from 1961 to 1990 was -9.1 °C, and from 1991 to 2005 was -7.7 °C; representing an increase of 1.4 °C over that period. If this change were to occur linearly, this would correspond to an average increase of 0.062°C per year, or 0.62 °C per decade. A more recent climate change assessment study conducted for the Inuvik Airport showed an increase in air temperature of 0.8 °C per decade from 1986 to 2016 (BGC Engineering Inc., 2016). Although complete historical temperature data is not available at other locations throughout the region, it is considered likely that the trends observed in Inuvik are representative of Mackenzie Delta and near-

shore Beaufort Sea region (Bonsal & Kochtubajda, 2009), which encompass the study area.

Year to year climate warming does not directly affect the analyses in this thesis conducted within a single thawing season. Any discussion on climate in the region would however be incomplete without addressing the existence and magnitude of climate warming. Additionally, an appreciation of the region's climate warming assists in the understanding of the local ground thermal regime which has been influenced by warming air temperatures. Future research including predictive long-term performance studies of the ITH should incorporate regional climate prediction models to assess the impact of climate change.

3.2.4 Ground Temperatures

A background review of ground temperatures was conducted to build on the overall understanding of the regional thermal regime, and assist in the estimation of the native soil thermal conductivity.

A number of deep boreholes were drilled throughout the Mackenzie Delta region, from the 1960s to early 1980s, primarily in the interests of hydrocarbon exploration. Temperature data from these boreholes have been catalogued in the Ground Temperature Database for Northern Canada (Geological Survey of Canada, 2000), and include several boreholes in the vicinity of the test site with temperature data collected between 1977 and 1981. Figure 3-4 shows 10 deep boreholes and their locations relative to the test site. The boreholes are identified by a 3-digit identification number in parentheses, and the text in bold indicates the depth to the base of permafrost. The 10 boreholes shown are situated 10 to 28 km from the test site.

The ground temperature profiles for the 10 boreholes were plotted in Figure 3-5 using data taken from the ground temperature database. It should be noted that only selected temperatures have been published in the database; typically at 25, 50, or 100 m intervals; and with the shallowest published temperature typically at a depth of 25 m. Over this depth range, the temperature profiles generally show the expected trend of increasing

temperature with depth, and with relatively consistent temperatures for a given depth between the boreholes. It is noted the ground temperatures cross over to positive temperatures (above 0 °C) below a depth of approximately 300 m.

Two boreholes identified as BH194 and BH275 showed more irregular temperature profiles, which were not representative of the trends observed in the remaining eight boreholes. Review of borehole BH194 shows it is located in a different physiographic region, at a much higher elevation that the remaining boreholes, likely contributing to its different temperature profile.

The non-linear temperature profile in BH275 can be explained as a result of its location in a swampy area at the edge of Parsons Lake. This phenomenon of the geothermal gradient straying away from linearity near the surface was discussed by (Lachenbruch & Marshall, 1986), for the near-identical case of a shallow lake overlying permafrost.

Review of satellite imagery (Google Maps, 2018) shows the remaining eight boreholes lie in comparatively dry areas, of similar physiography to the test site location. It is noted BH279 which appears to be located in Parsons Lake in Figure 3-4, is actually on dry land on a small island within the lake.

A linear trendline was fitted to the sub-zero ground temperature data (shown in Figure 3-5), with the data from BH194 and BH275 omitted. The equation for the fitted trendline within the frozen ground (below 0 °C) is as follows:

3-1

$$T = (0.0237°C/m)d - 7.52°C$$

Where:

T = ground temperature [°C]

$d =$ depth [m]

The coefficient 0.0237 °C/m represents the geothermal gradient, defined as the change in temperature with depth. This is equivalent to a 1 °C change per 42 m depth, which falls within the typical range of 1 °C per 30 to 60 m depth reported in literature (French, 1996). The geothermal gradient within the frozen ground is used in the estimation of the thermal conductivity of the native frozen soil, discussed in section 6.2.8.5. Solving for T = 0 °C, Equation 3-1 estimates the depth to bottom of permafrost at 317 m. This is consistent with the depth of 310 m, as used in the lithologic cross section[5] by (Allen, et al., 1988) discussed in section 3.2.1.

A linear temperature profile is indicative of the geothermal regime in equilibrium with the surface conditions (Karunaratne & Burn, 2003), (Lachenbruch & Marshall, 1986). A non-linear temperature profile means the ground temperatures are out of equilibrium with surface climate conditions (i.e. non-steady-state heat transfer). Departures from linearity in the shallower portions of the borehole are indicative of changes to near-surface heat transfer process. Such changes can include ground-water movement, topography, vegetation cover, and changes in climate (Pollack, 1993).

Given the climate warming over recent decades, the ground temperature profile would therefore be expected to bend astray from linearity, especially near the surface where the impacts of climate warming would be first experienced. The temperature profiles in Figure 3-5 however do no show a definitive warming trend near the surface. Reasons why a clear non-linear warming trend is not readily observed in Figure 3-5 are hypothesized below:

- Plotted ground temperature data is from 1977 to 1981 and misses the more recent warming which has occurred over more recent decades.

[5] Attempts to verify if the cross sections used by (Allen, et al., 1988) relied on any duplicate borehole data already referenced in the current study could not be fully confirmed. Permafrost depth by (Allen, et al., 1988) at the location of the test site was interpolated between 2 boreholes; the first which appears just east of Parsons Lake (possible duplicate), and the second 25 km further northeast (not a duplicate).

- Plotted ground temperatures are too deep to quickly respond to warming air temperature, as no shallow temperature data was available in the upper 25 m.
- Scatter of the temperature data in the upper approximate 200 m may have blurred any potential near-surface warming trends. If additional borehole temperature records were available, it is possible a clearer near-surface warming trend would have been observed. In a similar study of borehole temperatures on the Alaskan arctic coast by (Lachenbruch & Marshall, 1986) mostly positive curvature (warming) results were observed along with several negative curvature (cooling) results.

Returning to the fitted temperature profile outlined in Equation 3-1, the intercept value of -7.87 °C represents ground surface temperatures from 1977 to 1981 below the 25 m depth, extrapolated to ground surface (i.e. d = 0 m). This value was compared to available surface temperatures results reported in literature. Maps of near-surface ground temperatures in the Mackenzie Delta area were compiled by (Mackay, 1974), using temperature data from the late 1960s and early 1970s; and revised by (Burn & Kokelj, 2009), using temperature data from 2003 to 2007, which are shown in Figure 3-6 a) and b) respectively. The figures indicate that in the region of the test site and deep boreholes, near-surface ground temperatures were in the range of -7 °C to -6 °C in the late 1960s and early 1970s, and -6 °C to -5 °C from 2003 to 2007. This suggests the normal surface temperature in the late 1970s was likely already warmer than the -7.87 °C extrapolation, as the effects of the regional climate warming may have already begun influencing near-surface ground temperatures.

In summary, review of ground temperature data from the late 1970s shows a relatively stable equilibrium between surface climate and the deep ground temperatures. Analysis of the ground temperature data is also consistent in prediction of the depth of permafrost, to that reported in literature. The effects of recent climate warming were not apparent in the deep borehole data below 25 m, however climate warming in the region has been documented over the past several decades and has resulted in warmer near-surface ground temperatures.

3.3 Test Site

3.3.1 Overview

The ITH test embankment study site consisted of two adjacent 20 m long sections of the new highway. This included a geotextile-reinforced section, and an unreinforced section. This thesis focuses only on the 20 m long unreinforced section, located between station STA 82+380 and STA 82+400.

The use of an operational section of the highway for the study as opposed to a separate standalone non-operational embankment was chosen by the NWDOT. This was to avoid the costs associated with the construction of a standalone test embankment, while also focusing the efforts of the construction crew on completion of the highway during the short construction season. Advantages related to this arrangement were that it ensured the test section was built with the same conventional methods and equipment, and materials as the surrounding highway. Other advantages were the ease of access to test site, and that for future research the test site will be subjected to regular traffic loading.

Disadvantages to this arrangement included the very tight construction schedule, and some limitations to instrumentation[6] to permit for vehicle traffic and maintenance operations.

The specific location of the test site was selected by the University of Manitoba from several alternate locations. The selection was based on the 6 m fill requirement at this location. This was amongst the thickest fill requirements along the ITH and permitted for easier observation of settlement and lateral deformations.

[6] This included the requirement to bury all instrumentation wiring along the embankment slope, and inability to have permanent survey pins installed in the road or embankment slope surface.

The instrumentation plan was designed to obtain readings throughout half of the embankment cross section, and is discussed later in this chapter.

3.3.2 Embankment Fill Material

3.3.2.1 Material Source

Granular fill material for construction of the test embankment was sourced from Borrow Pit #174, located approximately 5 km northwest of the test site, as shown in the Construction Atlas in Appendix A. The contractor indicated the material from this portion of Borrow Pit #174 would be used as fill for the upcoming construction activities in the project area, including fill required for construction of the test embankment. Sampling of granular fill material from Pit #174 is discussed in section 4.1.1. Photos of the borrow pit and bulk fill sampling are shown in Appendix B, photos 1 to 4.

As previously discussed, the borrow materials from Pit #174 are of glaciofluvial origin, likely kame deposits, and consist of gravel and sand sized particles. Overall, a representative gradation for the granular fill classified as an SP-SM (poorly-graded sand with silt and gravel) type soil, discussed in further detail in section 4.2.

3.3.2.2 Gradation

Fully heaped CAT 740B rock trucks were used to deliver fill to the test site, each having a capacity of 24 m^3 when fully heaped (Caterpillar Inc., 2016). Each truckload of fill delivered to site appeared to have a relatively uniform gradation within that given truckload. Greater variability in gradation and frozen soil type (as described in the following sub-section) was however observed from one truckload to the next. The uniformity of gradation within a given truckload versus between different truckloads could be attributed to filling of each individual truck at a specific portion of the borrow pit, possessing a unique gradation due to natural segregation from the glaciofluvial deposition of the materials within the overall borrow source deposit. A second reason for the uniformity observed within a given truckload could be the mixing that occurs through the process of truck filling, dumping out, and spreading of the fill at the test site.

Further discussion is provided along with the sieve analysis results in section 4.2. Although not captured in the sieve analysis results, occasional cobbles and boulders were observed within the fill material delivered to site.

3.3.2.3 Description as Frozen Soil

The frozen fill material was classified in accordance with ASTM D4083-89 (2016): Standard Practice for Description of Frozen Soils. The classification provides a description of the soil phase, soil characteristics resulting from the frozen state, and description of important ice strata where present (ASTM, 2016). Using this classification, the frozen fill consisted of a combination of 4 subgroups. The subgroup symbols and descriptions are shown in Table 3-1, along with a visually estimated proportion of the contribution of each subgroup to the overall mass of frozen fill used in the embankment construction.

The author identified the need to provide a correlation between the ASTM D4083 frozen soil description, and the pore ice phases presented by (Haas, et al., 1978) outlined in section 2.6.1 to provide context for the expected mechanisms of compaction that would occur for the particular frozen soil types present at the test site. No published correlations were found, therefore the cases of pore ice development listed in Table 3-1 were based on the author's interpretation of the descriptions provided in the literature.

Table 3-1: Frozen Fill Description

Subgroup Symbol (per ASTM D4083)	Description (ASTM D4083)	Corresponding Case(s) of Pore Ice Development (per Haas, et al. 1978)	Estimated Proportion
Nf	Non-visible ice, poorly bonded or friable	Case I, Case II	40 %
Nbn	Non-visible ice, well-bonded, no excess ice	Case II, Case III	25 %
Nbe	Non-visible ice, well-bonded, excess ice	Case IV	25 %
Vx	Visible ice, individual ice crystals or inclusions (typically ~20 to 50% of total volume)	See Note	10 %

Note: No corresponding case of pore ice development is presented by (Haas, et al., 1978). A Vx soil type would resemble Haas et al.'s Case IV, however with loss of interparticle contacts due to high ice content.

Photos of typical samples of the various frozen soil subgroups are included in Appendix B. Typical Nf type frozen soil from the test site is shown laid upon the geotextile in Photo 15. Generally, the Nf type frozen soils had a high gravel content, while the Nbn and Nbe type frozen soils had higher sand contents. Nbn and Nbe frozen soils are difficult to differentiate by visual methods alone. Photo 16 is typical of both the Nbe and Nbn frozen fill at the site. Upon thawing, this differentiation could more easily be made. Photo 17 is indicative of Nbe soils after thawing, resulting in supernatant water at the soil surface. Photo 18 shows a (former) Nbn soil lump after thawing, requiring only minimal force to break the block apart, however lacking excess free water. A type Vx soil is shown in Photo 19 with apparent ice crystal inclusions.

It is important to note the estimated proportions listed in Table 3-1 represent the individual soil lumps delivered to the construction site prior to compaction, and that air voids were present between the individual soil lumps. Compaction of the frozen fill at the test embankment site should therefore by visualized as the re-organization of individual soil lumps, with the various soil lumps consisting of varying cases of pore ice

development. Furthermore, the structure of the individual lumps is altered (by breaking of the interparticle ice bonds) during compaction. It is hypothesized that during compaction, the more weakly-bonded lumps of lower ice-content are broken down more easily than the more strongly-bonded ice-rich lumps. Following compaction, the overall soil structure would thereby consist of ice-rich lumps, within a matrix of unbonded and poorly ice-bonded soil particles. Because the soil skeleton would be supported by the ice-rich lumps, air voids would also be present. The frozen soil structure following compaction should be considered when reviewing the processes of thaw consolidation, discussed later in the deformation modeling section.

3.3.3 Test Embankment Construction

3.3.3.1 General

The test embankment construction was coordinated into the overall highway construction activities taking place at the time by the contractor, E. Gruben's Transport Ltd. Coordination and timing of the test site construction into the contractor's overall schedule proved to be very difficult, due to the nearing the end of the winter construction season.

Construction of the test section was completed by the contractor's crew. The author, together with University of Manitoba Ph.D. student Earl De Guzman, and University of Manitoba geotechnical technician Kerry Lynch supervised the construction activities, and completed the instrumentation installation. Embankment construction and instrument installation was completed at a rapid pace over 7 days from April 14 to 20, 2015.

Drilling services for instrument installation were provided by the general contractor using a Sandvik DI550 DTH (down-the-hole) drill rig. The DTH drill rig was being used on the ITH construction project for drilling of blast-holes in the frozen borrow material at Pit #174 and other borrow sites (as shown in Photos 2 and 11 of Appendix B).

Throughout construction of the test embankment, the geometry was verified by the contractor's survey team to ensure the design was being met. Surveys were generally conducted before and after placement and compaction of each fill lift. The fill placement procedure is discussed in the following section. One notable difference between the

design and the as-built geometry at the end of construction was the addition of a 0.3 m "overbuild" used by the contractors. The "overbuild" consisted of an additional 0.3 m thick lift of compacted fill placed at the crest of the embankment. The purpose of the "overbuild" was to pre-emptively address some of the anticipated settlement that would occur over the thawing season. This would minimize the requirement for placement of additional fill by the contractor the following season to meet the embankment design elevation.

3.3.3.2 Fill Placement

The following procedure was employed for placement and compaction of each fill lift through the test section:

- Fill was delivered and dumped at the desired lift elevation.
- Oversized chunks exceeding 300 mm in diameter were broken down by running over with the dozer.
- Fill was pushed with dozer into loose, approximately 350 mm thick lifts.
- A minimum of 8 passes were made using a smooth, vibratory drum roller (CS78B Caterpillar), compacting the lift to 300 mm thickness.
- The operating weight with cab of the CS78B Caterpillar is listed at 18700 kg (Caterpillar Inc., 2016)

The following observations were made regarding the placement and compaction of the fill:

- Vibratory compaction was successful at breaking up frozen soil chunks at surface of lift as there were no frozen chunks protruding from the compacted surface. Botz and Haas (1980) reported that it was found by the Swedish State Power Board that heavy vibrating equipment was most suitable for compaction of frozen granular soils, during construction of the Messaure Dam.
- Occasional gravel or cobbles did protrude from the compacted surface.
- Little to no rutting (<25 mm) was caused by heavy vehicle traffic driving over the completed, frozen compacted surface.

Although temperature measurements of the fill material were not taken during construction, the mean air temperature as recorded from the Trail Valley climate station was -10.3 °C over the construction period. Air temperatures held constant below 0 °C throughout construction with the exception of on April 19 when air temperatures reached 1.5°C with some thawing of the upper 50 mm of fill visible (see Photo 20). No fill placement or compaction were undertaken at any time of positive temperatures however. Photos 5 to 9 of Appendix B show the typical embankment construction processes.

It should be noted that no field density tests were conducted on the frozen compacted fill during construction. This is acknowledged by the author as a shortcoming of the field study, as such information would have been useful in the characterization of the compacted embankment fill. Although nuclear densometer testing would not have been reliable given the frozen nature of the compacted soil, alternative field density testing such as use of a sand cone or rubber balloon test during construction could have provided valuable spot density checks during construction.

Due to the lack of field density testing, a review of construction methods was conducted to assist in the estimate of the compacted frozen fill density. The compaction methods and effort employed on the test site were generally consistent with methods commonly used to achieve 100 % SPMDD (Standard Proctor Maximum Dry Density)[7] on unfrozen granular fill on other heavy construction projects from the author's previous experience. This included the use of vibratory rollers conducting 8 passes per lift, as was observed on the test site. Some differences however included the thicker lift of 300 mm used at the test site, compared to the more typical 150 to 200 mm lifts used in typical construction. Some compensation for this thicker lift thickness was provided by the heavier compacting equipment used on the test site, having an operating weight of 18 700 kg, compared to the more typical range of 11 000 to 14 500 kg (Caterpillar Inc., 2016). In the absence of a more rigorous method of evaluation, it was assumed the construction

[7] At normal room temperatures, 100 % SPMDD (Standard Proctor Maximum Dry Density) is equivalent to 100% SPC ratio, as discussed in section 4.4

methods used at the test site were capable of delivering a compactive effort equivalent to 100 % Standard Proctor energy. The estimate of the effort applied during compaction was used along with a selected SPC ratio value to estimate the dry unit weight of the compacted frozen fill, which is later discussed in 4.4.2.

It is conceded the compaction of granular soils is a complex subject and dependant on many factors including compaction methods, and properties of the soil including range of particle sizes, shape of the particles, and shape of the gradation curve (Youd, 1973). However given the lack of on-site density testing, this was considered the best approach available. It is worthwhile noting however that in compaction test studies on a frozen silty sand by (Haas, et al., 1978), no significant changes to the frozen dry density were observed between tests conducted at Standard Proctor energy (600 kN-m/m^3) versus tests conducted at Modified Proctor energy (2700 kN-m/m^3), an energy difference equal to a factor of 4.5.

3.3.3.3 Instrumentation Installation

Instrumentation installed at the test embankment is described in detail in (De Guzman, et al., 2015) and included thermistors, Shape Accel-Arrays (SAAs), and piezometers. The following table summarizes the instrumentation installed on the test site. The as-built locations of the instruments were surveyed and measured in the field, and are shown within the embankment cross-section in Figure 3-8.

Table 3-2: Instrumentation Summary

Instrument Type	Usage	Accuracy and Units of Measurement	Quantity Installed at Control Section
Thermistor Strings	Measures temperature at each node of the string	Temperature: ±0.1°C	4 strings (comprising 19 total nodes)
Shape-Accel-Array (SAA)	Measures inclination of individual rigid segments, which is converted to vertical or lateral displacement. Also measures temperature	Deformation: ±1.5 mm (see Note 1) Temperature: ±1°C	(1 horizontally + 1 vertically),
Piezometers	Measures porewater pressure and temperature	Pressure: ±0.35 kPa Temperature:<0.04% Full Scale per °C	2, in each of XS-C and XS-R

Notes: 1) Accuracy listed for typical 32 m length array, however accuracy is improved for shorter array lengths (Measurand, 2017). Array lengths on project were 4.88 and 8 m in length (i.e. accuracy within ±1.5 mm)

Most instruments listed above are common in geotechnical engineering applications and do not require further explanation on their functions. As the SAA is less commonly used, and the following brief description is provided.

The SAA has a similar function to the more commonly used slope inclinometer; used for detecting relative movement perpendicular to the axis in which it is installed (i.e. a horizontal SAA measures vertical displacement and a vertical SAA measures lateral displacement). The advantage of the SAA in this application is that the sensors remain in place post-installation and can be activated and recorded by a data acquisition system, eliminating the requirement for on site readings by personnel as in the case of a slope inclinometer. On this project each SAA consisted of an array of 16 rigid segments (either of 305 mm or 500 mm in length), connected by flexible joints. The SAAs were installed within protective 25 mm PVC pipe, and laid flat or installed vertically within a drilled hole. Each segment contains a micro electro-mechanical systems (MEMS) accelerometer, which measure changes in inclination as the SAA deforms along with the surrounding soil (Measurand, 2017). The recorded data is then compiled using specialized software to

provide deformation measurements for both ends of each rigid segment. To accurately measure total deformation, one extremity of the SAA must be anchored or fixed, as the SAA can only measure relative deformation from one segment to the next. On this project, the fixity of one end of the SAA was achieved by embedment into frozen soil. A secondary function of the SAA is its capability to measure temperatures. A photograph of the SAA installation are shown in Photo 10 of Appendix B. It should be noted the SAA temperature readings are measured at the nodes located at the centre of each rigid segment (as indicated by dots along the SAAs in Figure 3-8), while deformations are calculated at the extremities of each rigid segment (mid-way between each temperature-sensing node, as well as the extremities of the SAA). Since each SAAs each had 16 rigid segments, they therefore provide 16 temperature readings, and 17 deformation measurements.

The placement of the individual instruments during construction successfully matched the intended design location, with some minor deviations as the result of placement of excess fill by the contractor or slight over/under drilling of holes for downhole instrument installation. The as-built locations of the instruments were used in the analyses, with the locations also included in the CAD drawings submitted as part of the electronic appendix.

The reported elevation of thermistor string TS-C4 has been lowered by 0.19 m to account for differences in elevation of the ground surface at the locations of the thermistor string compared to at the locations of the cross-sections of interest, XS-C. That is, the depth of embedment below ground surface for the thermistor nodes has been maintained. Such adjustments were not required for the remaining thermistor strings since these thermistors were installed directly at the cross-sections of interest, XS-C.

Over the course of the study period, the vibrating wire piezometers remained within frozen ground and provided no porewater pressure measurements. Discussion of measured porewater pressures is therefore absent in this current study. The vibrating wire piezometers were still able to collect temperature data, which was analyzed alongside the other temperature node data from the other instruments.

3.3.4 Embankment Geometry and Topographic Survey

A topographic survey of the embankment could not be conducted immediately following construction. This was because all construction crews, equipment, and survey crews were abruptly ordered to leave the ITH project on April 20, 2015 as a result of positive temperatures, thus signaling the end of the construction season. Without survey results following the embankment construction, the embankment design drawings were relied upon to establish the geometry of the as-built condition. This assumption was considered acceptable given the frequent surveying conducted by the contractor's survey crew during the construction process to ensure the construction was meeting the design geometry.

As previously discussed, the contractor employed the strategy of "overbuilding" at the embankment crest as so to better match the design geometry after the thawing season.

The cross-sectional geometry for the as-built condition immediately following construction was thereby taken as the design drawings, with an additional 0.3 m overbuild added on the embankment crest.

A topographic survey of the embankment test area was completed on March 1, 2016 by an survey team retained by the NWDOT. The topographic survey consisted of 5 complete cross-sections of the embankment, taken at 10 m intervals between stations STA 82+380 to STA 82+420. It is emphasised the March 1, 2016 survey date fell prior to the start of the 2016 thawing season. Assuming that no additional settlement occurred between freeze-up of the embankment in October 2015 and the time of the survey on March 1, 2016, the survey data can be considered representative of the embankment geometry at the end of the 2015 thawing season. Test site monitoring results continuing into the 2016 thawing season published by (De Guzman, et al., 2017) generally support this assumption[8].

[8] Vertical displacements measured by SAA-CH over the freezing season between October 2015 and April 2016 actually indicate uplift in the order of 0 to 50 mm, with greatest uplift located at the exterior of the

A single cross-section was selected to represent the un-reinforced “control” section, to allow for consistent analysis of both measured and modelled temperature and deformation results. The cross-section, named XS-C was selected to coincide with the as-built alignment of the horizontal and vertical SAAs in the control section of the embankment. The alignment of the XS-C cross-section corresponds to station STA 82+393.69, located near the centre of the control section. The location of XS-C is shown in plan view in Figure 3-2, and the cross-section can be seen in Figure 3-8.

embankment. The author suspects this uplift to be associated with frost heave of the saturated thawed soils near the exterior of the embankment, however this has not yet been studied in detail.

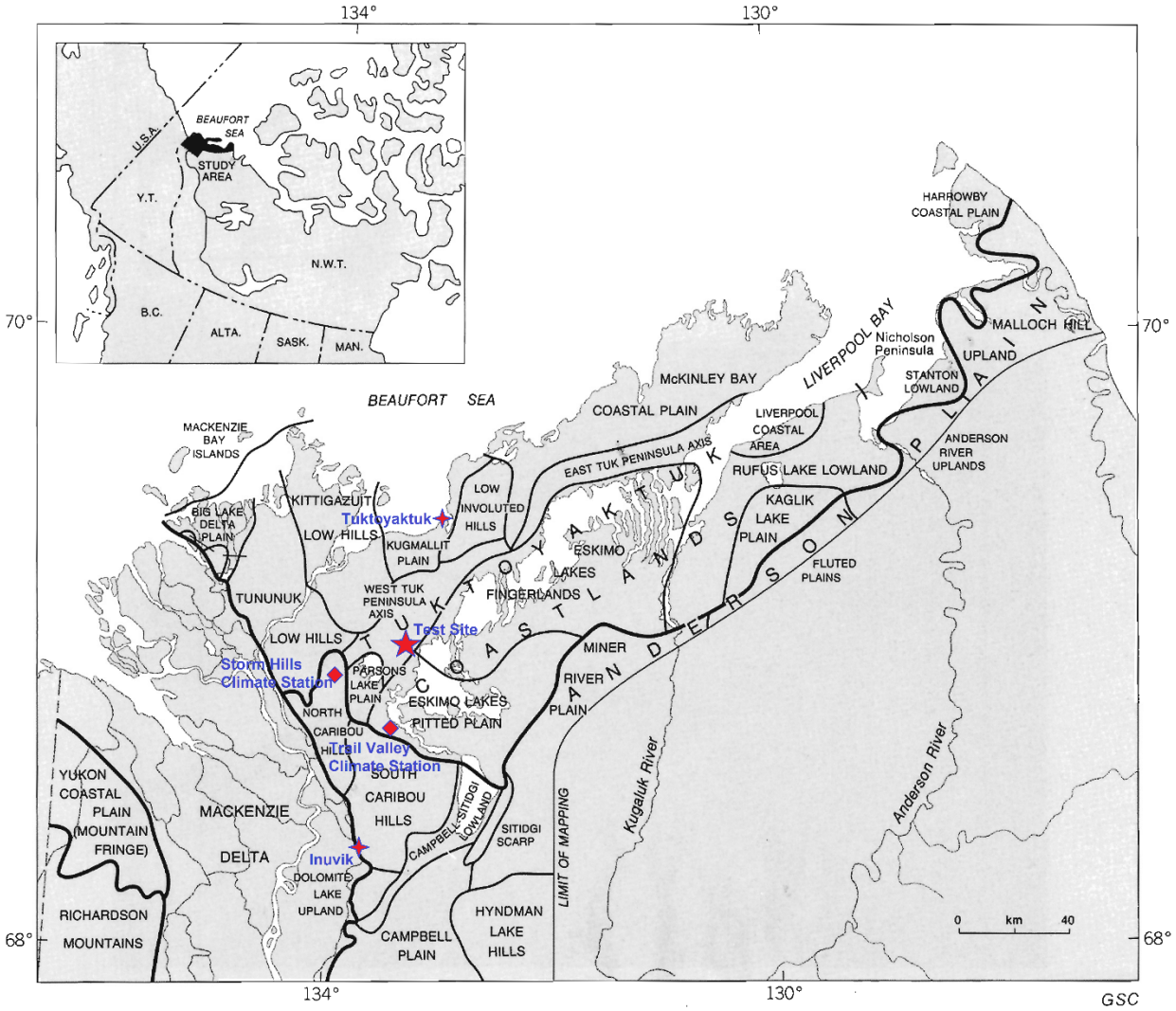

Figure 3-1: Physiographic Regions and Sub-regions of the Tuktoyaktuk Coastlands and adjacent areas (Physiographic regions are delineated by bold lines [Tuktoyaktuk Coastlands, Anderson Plain, Mackenzie Delta, Yukon Coastal Plain, Richardson Mountains]. Sub-regions are delineated in fine lines.) (Rampton, 1988) – Government publication.

Figure 3-2: Site plan.
Satellite imagery from (Google Maps, 2018)

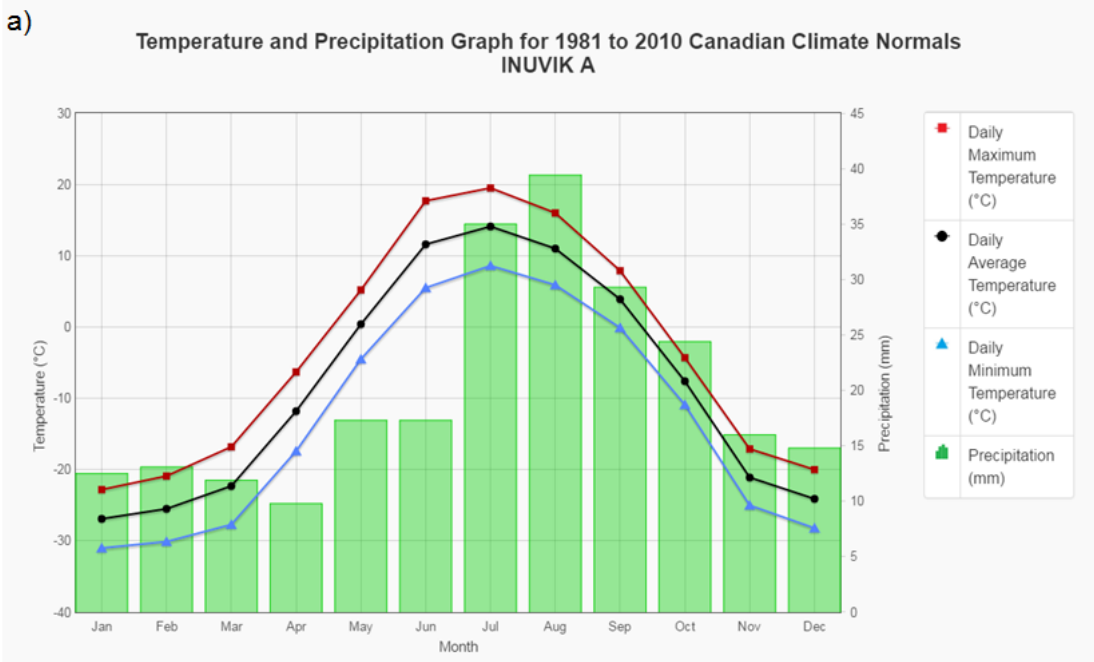

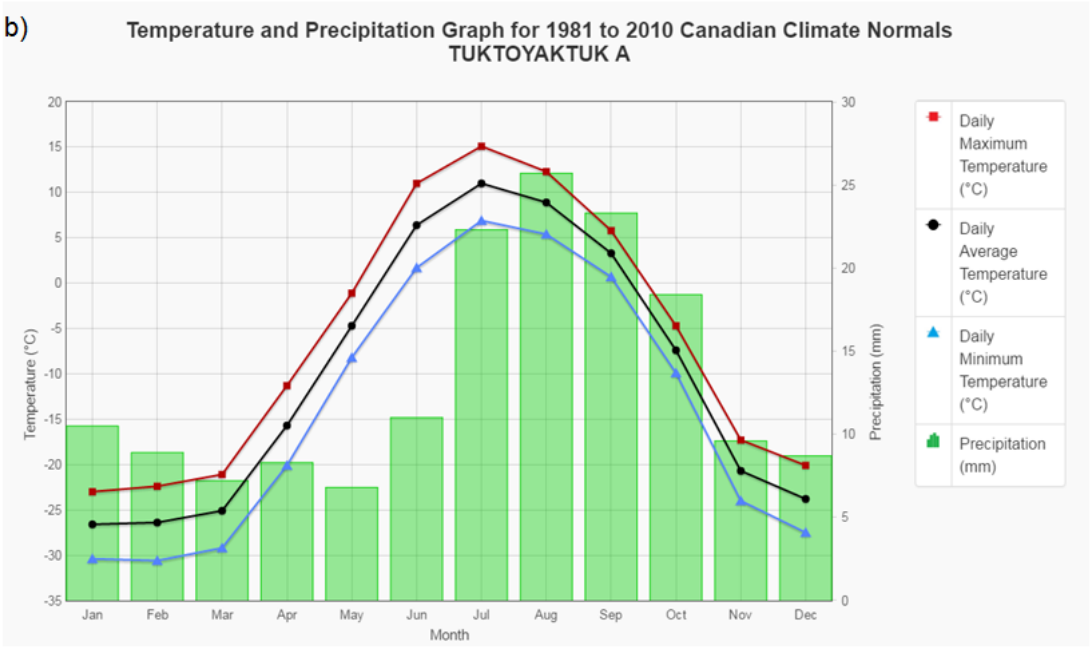

Figure 3-3: Inuvik and Tuktoyaktuk Climate Normals
(Government of Canada National Climate Services, 2016) – Government publication.

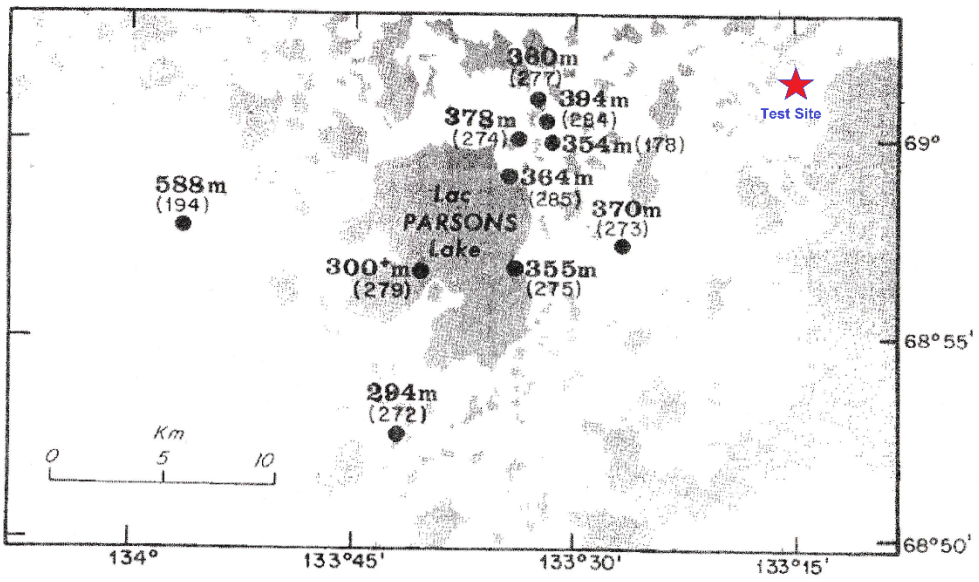

Figure 3-4: Deep Borehole Ground Temperature Location Map
(Borehole identification number shown in parentheses, depth to the base of permafrost shown in bold text) (Geological Survey of Canada, 2000) – Government publication.

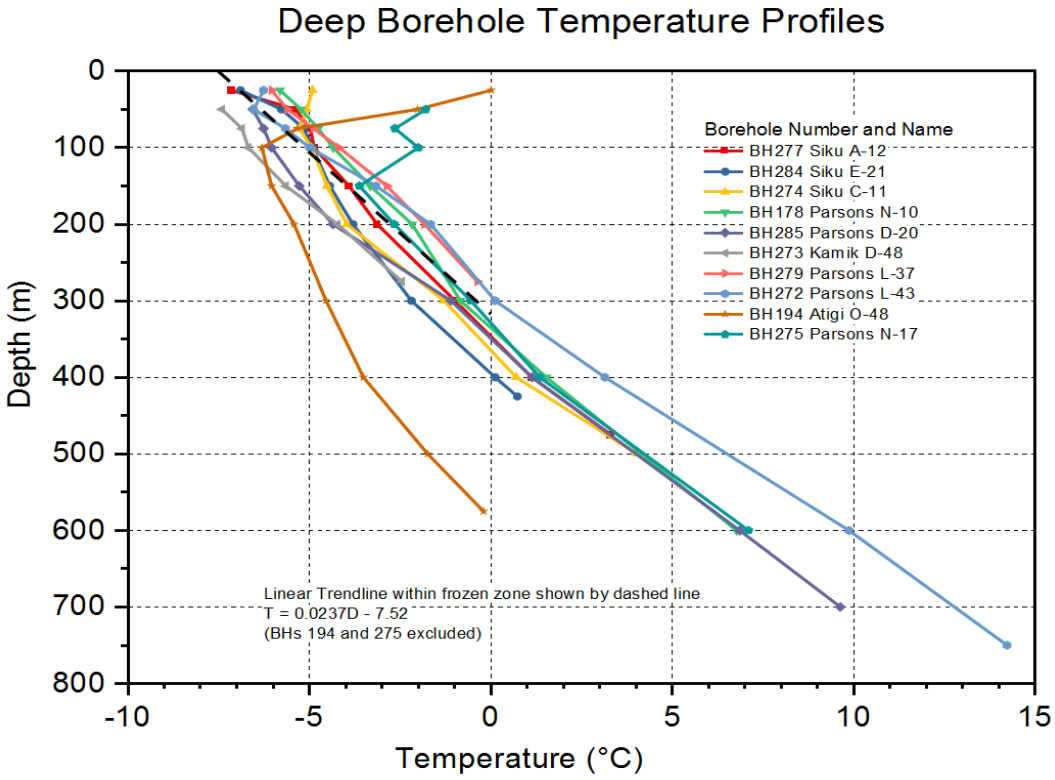

Figure 3-5: Deep Borehole Temperature Profiles.
Data obtained from (Geological Survey of Canada, 2000)

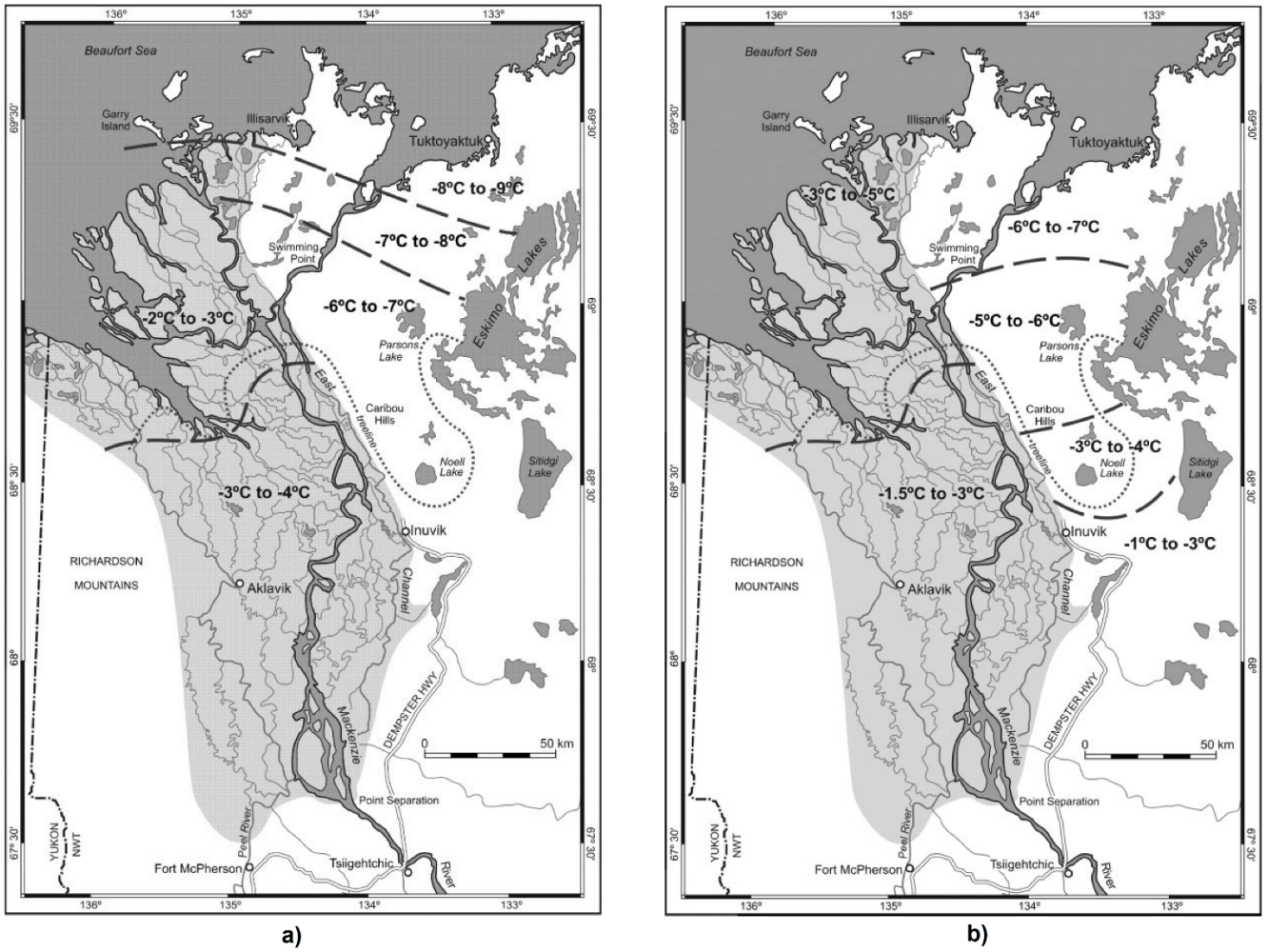

Figure 3-6:Near-Surface Ground Temperatures of the Mackenzie Delta Area in; a) the late 1960s and early 1970s from (Mackay, 1974), and b) between 2003 and 2007 from (Burn & Kokelj, 2009) Reproduced with permission from John Wiley and Sons.

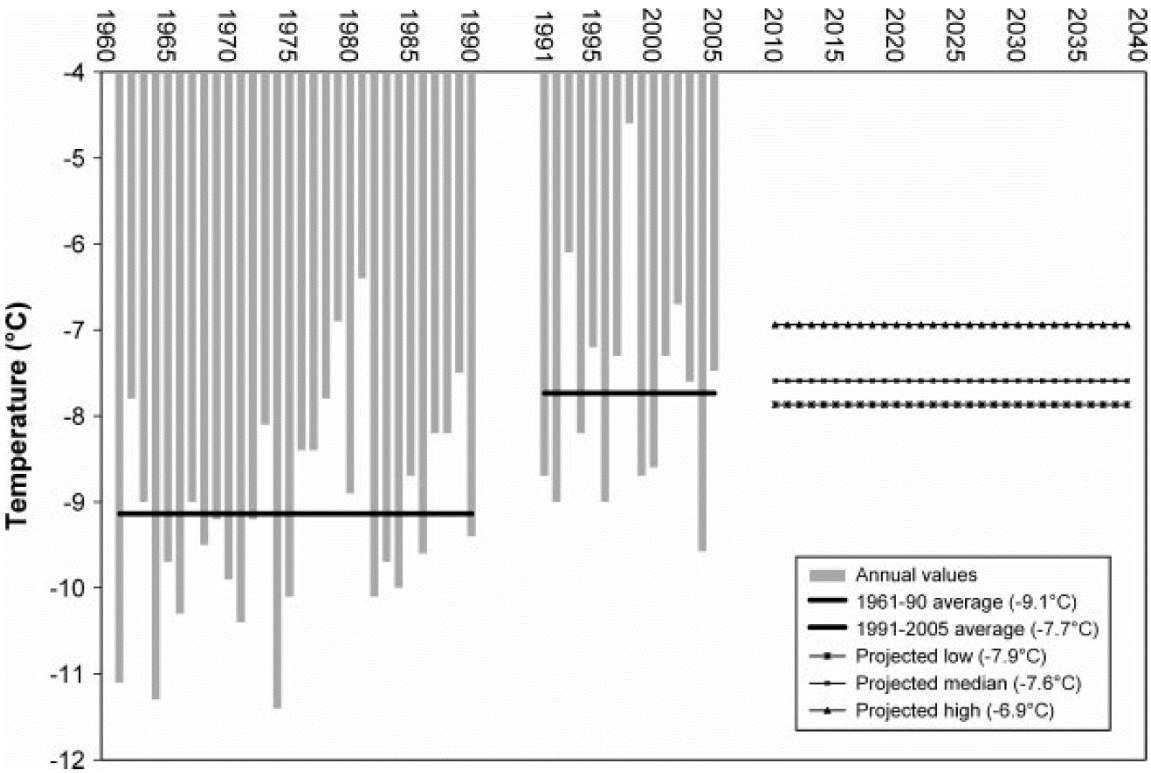

Figure 3-7: Inuvik Annual Average Temperatures from 1961 to 2005
. (Bonsal & Kochtubajda, 2009) – Reproduced with permission from John Wiley and Sons.

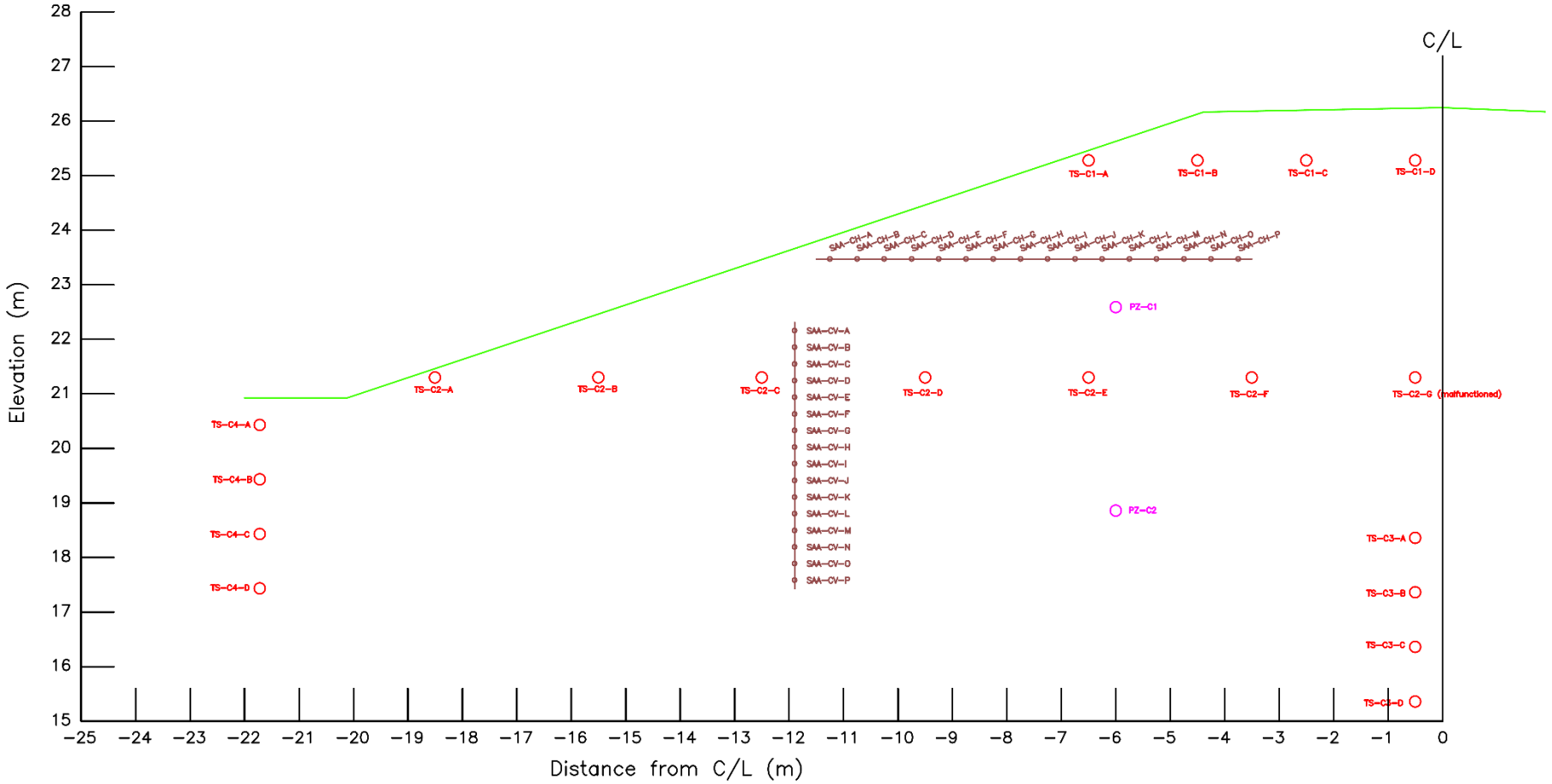

Figure 3-8: As-built Instrumentation Plan

4 Laboratory Testing

4.1 Overview

Laboratory testing was conducted on select samples recovered from the field study. The purpose of the laboratory testing was to classify the soil, as well as study soil properties as they relate to performance of the test embankment.

The laboratory testing program included water content, sieve and hydrometer analysis, plasticity index, and moisture-density (Proctor) testing. The testing was carried out by University of Manitoba graduate students Earl De Guzman, Dylan Stafford, and Samuel Kaluzny. (De Guzman, et al., 2018)

4.1.1 Sampling Procedure

Samples were recovered during the test embankment construction and returned to the University of Manitoba for laboratory testing. The sampling consisted of individual grab samples, as well as bulk soil bag samples.

A total of 11 grab samples were collected from the embankment test site, identified as EGS-1 to EGS-11. This included 7 grab samples of frozen granular fill sampled from various fill lifts delivered to site over the course of construction. Another 4 grab samples consisting of native soil from the embankment foundation level were collected from the material jettisoned to the surface by forced air during drilling with the DTH drill rig. Photographs 11 and 12 of Appendix B show materials being forced out of the borehole during drilling, and the resulting materials which were sampled following drilling.

Bulk fill sampling was conducted directly from borrow Pit #174, which was the source of granular material for several kilometers of highway, including the test embankment section. An excavator was used to fill four one-cubic-metre sized soil bags with granular fill taken from an approximately 20 m wide by 5 m high exposed face, that had recently been opened by blasting. The soil bags were filled with material taken from different areas of the exposed face using an excavator, as shown in Photo 3 of Appendix B. An

additional 7 grab samples identified as P174-1 to P174-6, and P-174-8 were taken from material placed in the large soil bags.

All grab samples were placed in airtight containers and maintained at sub-zero temperatures in a cooler while on the research site. Each grab sample had a wet mass of approximately 2 kg. The grab samples thawed during transport back to Winnipeg and were tested immediately for water content to before the samples would lose moisture.

The 4 large bulk soil bags were trucked to Winnipeg, and were used for the tests requiring significant soil volumes. Thawing of the large soil bags occurred during shipment to Winnipeg, resulting in loss of moisture through seepage through the mesh bag, and evaporation. The bulk samples were therefore not representative of on-site moisture conditions.

It is noted the relatively small size of the granular fill grab samples very likely resulted in the under-representation of the coarser, gravel to cobble-sized particles within the samples. Aside from misrepresenting the gradation, this also would have led to an over-estimation of the embankment's natural water content. A correction is addressed in section 4.3.2.

4.2 Particle Size Analysis

4.2.1 Procedure and Results

Granular fill grab samples collected from the embankment and borrow Pit #174 were tested for sieve analysis in accordance with ASTM D422-63 (ASTM, 2007). The sieve analysis results are presented in Figure 4-1 a). The embankment samples are identified by the prefix "EGS" and those from Pit #174 identified by the prefix "P174". The gradation identified as "CM-4" is considered as an average representation of the granular fill used in the test embankment construction and is discussed in the following section.

Figure 4-1 b) shows other selected gradations used in the comparison and discussion of lab test results. Gradation CM-4 is shown once again, alongside "CM-4-P19"[9] which is identical to CM-4, but only containing the fraction passing the 19 mm sieve. An average gradation of the embankment grab samples is shown as "EGS-AVG". Another 4 gradations from lab test results from the literature of (Botz & Haas, 1980) and (Clark, 1970) are presented for comparison purposes to Proctor compaction test results and are discussed in detail in section 4.4.2. The significance of the remaining gradations presented in Figure 4-1 a) and b) is discussed below.

4.2.2 Discussion

Many soil properties, such as water content, moisture-density relationships, and various thermal properties, are influenced by the particle size of soils. The review of the fill material gradations in this section permits for 1) the classification of the soil, 2) the translation of laboratory-measured soil parameters between the different gradations included in the study, and 3) comparison of soil properties with literature results.

The results in Figure 4-1 a) show a relatively broad scatter of gradations across the embankment grab samples. This supports the observations made during construction of the variability in fill gradation between the different truckloads delivered to the test embankment site.

The CM-4 gradation shown in Figure 4-1 a) and b) was obtained as the average gradation from a series of tests on composite mixtures obtained from the bulk fill samples obtained from Pit #174 (De Guzman, et al., 2018). The CM-4 gradation therefore serves as an idealized representative gradation when discussing the embankment fill material.

[9] The suffix "P19" refers to the material *passing the 19 mm* sieve size.

The embankment fill, represented by the CM-4 gradation consisted of 28.1 % gravel sized particles, 60.8 % sand, and 11.1 % fines (silt and clay). Hydrometer analysis of the fines by (De Guzman, et al., 2018) indicate the silt and clay represent approximate overall soil fractions of 8.0 and 2.0 % respectively. In accordance with the Unified Soil Classification System, the CM-4 gradation classifies as an SP-SM soil type (poorly-graded sand with silt and gravel).

Because the CM-4 gradation was prepared using material from the large bulk fill samples, it contains a higher fraction of coarse, gravel-sized particles and is considered more representative of the overall embankment fill than the smaller grab samples, which tend to under-represent of the coarser material fractions. This lack of coarser particles in the grab samples is apparent when taking the average gradation of the embankment grab samples, shown as EGS-AVG in Figure 4-1 b), and comparing this to the CM-4 gradation shown in the same figure. It is noteworthy the EGS-AVG gradation curve follows nearly parallel to the CM-4 gradation, but merely shifted indicating the difference in gravel content.

Figure 4-1 b) introduces gradation CM-4-P19. This gradation was created by mathematically subtracting the particles greater than 19 mm, from the CM-4 gradation. The 19 mm maximum particle size is of significance since this represents the maximum particle size permitted in both the Proctor compaction testing. In other words, the CM-4-P19 gradation represents the gradation of the granular fill used in these laboratory tests. It is of interest to note the stark similarity between the EGS-AVG gradation (for which a corresponding average natural water content was measured) and the CM-4-P19 gradation.

4.3 Water Content

4.3.1 Procedure and Results

Grab samples of the granular fill and native soil were tested for water content[10] in accordance with ASTM D2216-10 (ASTM, 2010), with the results summarized below:

Table 4-1: Water Content Results for Grab Samples

Native Soil		Granular Fill	
Sample ID	W.C. (%)	Sample ID	W.C. (%)
EGS-5	1891.9	EGS-1	13.8
EGS-6	664.7	EGS-2	20.9
EGS-7	105.2	EGS-3	21.9
EGS-8	410.1	EGS-4	3.5
Average	768.0	EGS-9	14.4
		EGS-10	16.5
		EGS-11	17.9
		Average	15.6

Data from (De Guzman, et al., 2015)

4.3.2 Discussion

Water contents of the native soil were relatively high, and highly variable, ranging from 105.2 to 1891.9 %. These elevated water contents of high variability are typical of near-surface ice rich permafrost soils in the western Canadian Arctic (French, 1996, p. 89).

[10] Water (moisture) contents throughout this thesis are expressed as gravimetric water content (ratio of mass of water to mass of dry soil particles). The term "volumetric water content" is used in the specific cases where applicable (most notably the thermal properties in thermal modelling section).

Water contents of the granular fill grab samples collected from the test embankment during construction ranged from 3.5 to 21.9 %, with an average water content of 15.6 %. This same group of samples had an average gradation EGS-AVG. Given the almost identical gradation between EGS-AVG and CM-4-P19 (as noted in section 4.2.2), a natural water content of 15.6 % was considered a good estimate for the CM-4-P19 gradation as well.

As previously discussed, gravel-sized particles were underrepresented in the grab samples. This results in a misrepresentation of the embankment's natural water content when relying on the grab samples. To estimate the natural water content of the as-built embankment with the corresponding gradation CM-4, an oversize correction was applied to the water content of the grab samples in accordance with ASTM D4718-87, Standard Practice for Correction of Unit Weight and Water Content for Soils Containing Oversize Particles. The oversize correction is a mathematical equation for correcting the water content and unit weight of a finer fraction of soil, to determine the corresponding water content and unit weight of the total fraction of soil (ASTM, 2007).

Applying the oversize correction, the water content of 15.6 % corresponding to the CM-4-P19 gradation, corrects to a water content of 13.7% for the CM-4 gradation. This value of 13.7 % was considered representative of the embankment's natural water content following construction.

4.4 Moisture-Density Relationships

4.4.1 Procedure and Results

Moisture-density relationships for the embankment fill materials were tested as part of the studies by (De Guzman, et al., 2018). The tests, commonly referred as Standard Proctor tests, were conducted in accordance with ASTM D698-12: Laboratory Compaction Characteristics of Soil Using Standard Effort, using sub-method C (ASTM, 2012).

There are 3 sub-methods of the test standard, which each limit the maximum particle size in the test. Sub-method C permits the inclusion of any particles passing the 19.0 mm

sieve in the test, whilst the other sub-methods limit maximum particles size to those passing the 9.5 mm sieve. Sub-method C was therefore deemed the most appropriate for the fill material, to accommodate the coarse nature of the soil. The soil fraction tested in sub-method C, (once the material retained on the 19.0 mm sieve is removed) is equivalent to the CM-4-P19 gradation, as previously defined in section 4.2. The oversize correction discussed in the previous section was then used to correct the results to be applicable to the coarser embankment gradation (CM-4). Both the corrected and uncorrected results are presented, as the uncorrected (passing the 19.0 mm sieve) results can be more easily compared to results from literature (also passing the 19.0 mm sieve).

The Proctor tests were conducted in unfrozen and frozen conditions, at temperatures of 23 °C and – 10 °C respectively.

As Proctor testing is intended for unfrozen soils, some modifications to the standard test method were required. For the Proctor test conducted on the ITH fill material at -10 °C, the soil samples were prepared as follows:

- Predetermined amount of water added to dry soil to obtain desired water content
- Moist soil was frozen into ~20 mm thick slabs in steel pans
- Slabs were broken using a hammer into frozen lumps to a size passing 22.5 mm sieve
- Gradation of frozen lumps was well-graded, with the shape of the frozen aggregate classifying as angular[11]

The uncorrected and oversize-corrected Proctor curves are shown in Figure 4-2 a) and b) respectively. The test results are summarized in Table 4-2 below.

[11] Based on definition for "well-graded gravel", and visual-manual procedure for describing angularity outlined in ASTM D2488-09a: Standard Practice for Description and Identification of Soils (ASTM, 2009)

Table 4-2: ITH Fill Proctor Test Results Summary

Soil State	Testing Temperature	Uncorrected		Oversize-Corrected	
		Maximum Dry Unit Weight (kN/m³)	Optimum Water Content (%)	Maximum Dry Unit Weight (kN/m³)	Optimum Water Content (%)
Unfrozen	23 °C	19.54	9.4	20.17	8.2
Frozen	-10 °C	N/A (undefined)	N/A (undefined)	N/A (undefined)	N/A (undefined)

Uncorrected values from (De Guzman, et al., 2018)

Note that no maximum dry unit weight is defined for the frozen soil condition, since dry unit weight decreases continuously as moisture content increases, as can be seen in the figures. The maximum dry unit weight at the optimum water content (OWC) for the unfrozen soil corresponds to point (A) on both Figure 4-2 a) and b). Point (B) represents the frozen soil dry density at the equivalent OWC at Standard Proctor Effort. Points (C) and (D) represent the dry densities at the embankment's natural water content at Standard Proctor Compactive Effort for the unfrozen and frozen soil cases respectively.

4.4.2 Discussion

Limited research exists on the compaction of soils in a frozen state, therefore the Proctor test results were compared to similar testing programs presented in the literature by (Clark, 1970)[12] and (Haas, et al., 1978)[13]. The testing programs were conducted on different soils, with the gradations of the soils most similar to the ITH fill re-plotted in Figure 4-1 b) for direct comparison. This section compares the Proctor test results from the current ITH study to the results from the two aforementioned studies. The purpose of

[12] Original testing program was conducted and published by (Clark, 1970), with additional discussion of the same test program published by (Burwash & Clark, 1981)

[13] Original testing program was conducted and published by (Haas, et al., 1978), with additional discussion of the same test program published by (Botz & Haas, 1980)

the laboratory test review is to estimate the dry density of the compacted frozen fill at the test embankment.

The testing program by (Haas, et al., 1978) employed similar procedures to those listed for the ITH testing program, with the most notable difference being the use of standard ~20 mm sized frozen soil cubes rather than crushed frozen soil chunks. The study's authors state the use of frozen soil cubes was chosen to achieve high reproducibility of results. It is hypothesized the decision to use crushed frozen soil chunks in the ITH fill testing program was appropriate however, given the gradation of the crushed frozen soil chunks more closely resemble the relatively well-graded distribution of the blasted frozen material delivered to the embankment test site. Little information was available on preparation methods for the frozen soil particles in the testing program by Clark.

The 3 testing programs on frozen soil all showed the expected trend of decreasing dry density with increasing water content. It is noted both the ITH test program and the program by Clark only capture the right-side (higher water content) portion of the bilinear trend, as they did not extend to sufficiently low water contents to establish the initial steeper portion of the trendline, as previously shown in Figure 2-7.

To quantify the reduction in compaction between unfrozen to frozen soil states, SPC ratios were calculated for the test results from the current ITH testing program, and interpreted from the test data by Botz & Haas. SPC ratios in Clark's test program were directly reported by (Burwash & Clark, 1981). Since the studies by both Clark, and Botz & Haas were conducted on soils finer than the 19.0 mm sieve size, this permits for ideal comparison to be made with the ITH Fill CM-4-P19 gradation. As such, the ITH Fill uncorrected Proctor results (applicable to the CM-4-P19 gradation), are used for comparison with the literature results in this section.

The comparison of SPC ratios is summarized in Table 4-3 below. The dry unit weights in Clark's experiments were back-calculated using the known SPC ratios, and the SPC ratios in the experiments by Botz & Haas using the known dry unit weights at room temperature and frozen conditions. It should be noted the dry unit weights for the frozen

soils are based on a water content in the frozen soils equivalent to the optimum water content (OWC) obtained at room temperature conditions.

Table 4-3: Literature Comparison of SPC Ratios at Optimum Water Content

Study	Soil Type	Optimum Water Content [%]	Max. Dry Unit Weight [kN/m³]	Frozen Dry Unit Weight(1) [kN/m³]	SPC Ratio	Frozen Compaction Temperature
Clark	Sand	11.4	18.04	14.43(2)	80 %	-10 °C (see Note 2)
	Gravel	6.0	20.79	17.26(2)	83 %	
Botz & Haas	Yellow Sand	12.5	17.75	12.01	68%	-7 °C
	Gray Sand	13.0	17.59	11.97	68%	
ITH	ITH Fill CM-4-P19	9.4	19.54	15.09	77%	-10 °C

Notes:

1. At water content equal to room temperature OWC.
2. After Fig. 6 by (Burwash & Clark, 1981), interpolation at -10 °C based on tests conducted at -2 °C and -23 °C.

As shown in the table above, a frozen dry unit weight of 15.09 kN/m³ was obtained for the ITH Fill at a moisture content equivalent to the unfrozen OWC (corresponding to point B in Figure 4-2 a)). Dividing this value by the (unfrozen) maximum dry unit weigh of 19.54 kN/m³, an SPC ratio of 77% was obtained for the ITH fill. Compared to the results reported by (Burwash & Clark, 1981), the ITH fill SPC ratio is a slightly lower value than expected, given the CM-4-P19 gradation falls within the gradation limits of Clark's "Sand" and "Gravel", for which SPC ratios of 80 and 83 % were obtained respectively.

In the experiments by Botz & Haas, an SPC ratio of 68% was obtained for both the "Yellow Sand" and the "Gray Sand". Compared to the ITH fill, this lower SPC ratio value is expected, given the finer gradation of these sand soils. Secondly, it is hypothesized the lower SPC ratios for the Botz & Haas tests may be attributed in part to

differences in preparation of the frozen soil particles prior to compaction. Compaction of the uniform frozen soil cubes in the Botz & Haas study would be less efficient compared to the more "well graded" frozen lumps in the ITH fill testing program, offering a second potential explanation for Botz & Hass' lower SPC ratios. Further investigation on the effects of the initial structure of the frozen soil lumps on the final compacted dry density is recommended in future research.

While the results in Table 4-3 evaluate the SPC ratio based on the frozen dry unit weight at optimum moisture content, the ITH test site embankment was constructed with soil moisture levels well above optimum. The natural water content of the CM-4-P19 soil was 15.6 % (corresponding to point D in Figure 4-2a)), or 6.2 % above the optimum moisture content of 9.4 %. A review of the literature test results was attempted to determine if the SPC ratios would be affected at moisture contents well above optimum. Unfortunately the test programs by both Clark, and Botz & Haas were inconclusive in determining if SPC ratios were affected at moisture contents as high as 6.2% above optimum. This is because those test programs did either not extend to sufficiently high moisture contents, not did they contain enough datapoints to reveal a clear trendline at those elevated moisture contents.

In the case of the ITH fill testing program, the Proctor testing was conducted over a larger range of moisture contents above optimum. At the CM-4-P19 natural water content of 15.6 %, the unfrozen and frozen dry unit weights at standard compaction effort were 18.34 and 13.75 kN/m³ respectively (as identified by points C and D on Figure 4-2a)).

Similarly for the oversize-corrected results; at the CM-4 natural water content of 13.7 %, the unfrozen and frozen dry unit weights at standard compaction effort were 19.04 and 14.59 kN/m³ respectively (as identified by points C and D on Figure 4-2b)). This converts to an SPC ratio of 77%, the same as that obtained at optimum moisture content. In summary, the ITH fill tests indicate a relatively unchanged SPC ratio at moisture levels well above optimum, equivalent to those natural moisture levels encountered in the embankment.

In summary, the dry unit weight of the frozen compacted fill was estimated at 14.59 kN/m³, and is represented by the condition shown in Figure 4-2 b) at Point D. The above completes objective 2) shown in section 1.3, of estimating the density of the embankment fill compacted in a frozen state. The following summarizes the methodology from which this value was obtained:

- The embankment fill is best represented by the CM-4 gradation, which has a corresponding natural water content of 13.7%.
- Temperature of the embankment fill material during compaction was approximately -10 °C, based on temperature data during construction.
- Effort applied during compaction of embankment fill material was equivalent to 100% of Standard Proctor.
- Based on Proctor testing results at -10 °C, an SPC ratio of 77 % would be expected for the ITH fill compacted at 100% of Standard Proctor effort at this temperature. From review of the limited available literature, and given the soil type, an SPC ratio of 77% appears reasonable.

This state of dry unit weight and water content was used to characterize the frozen compacted fill in the upcoming modelling sections.

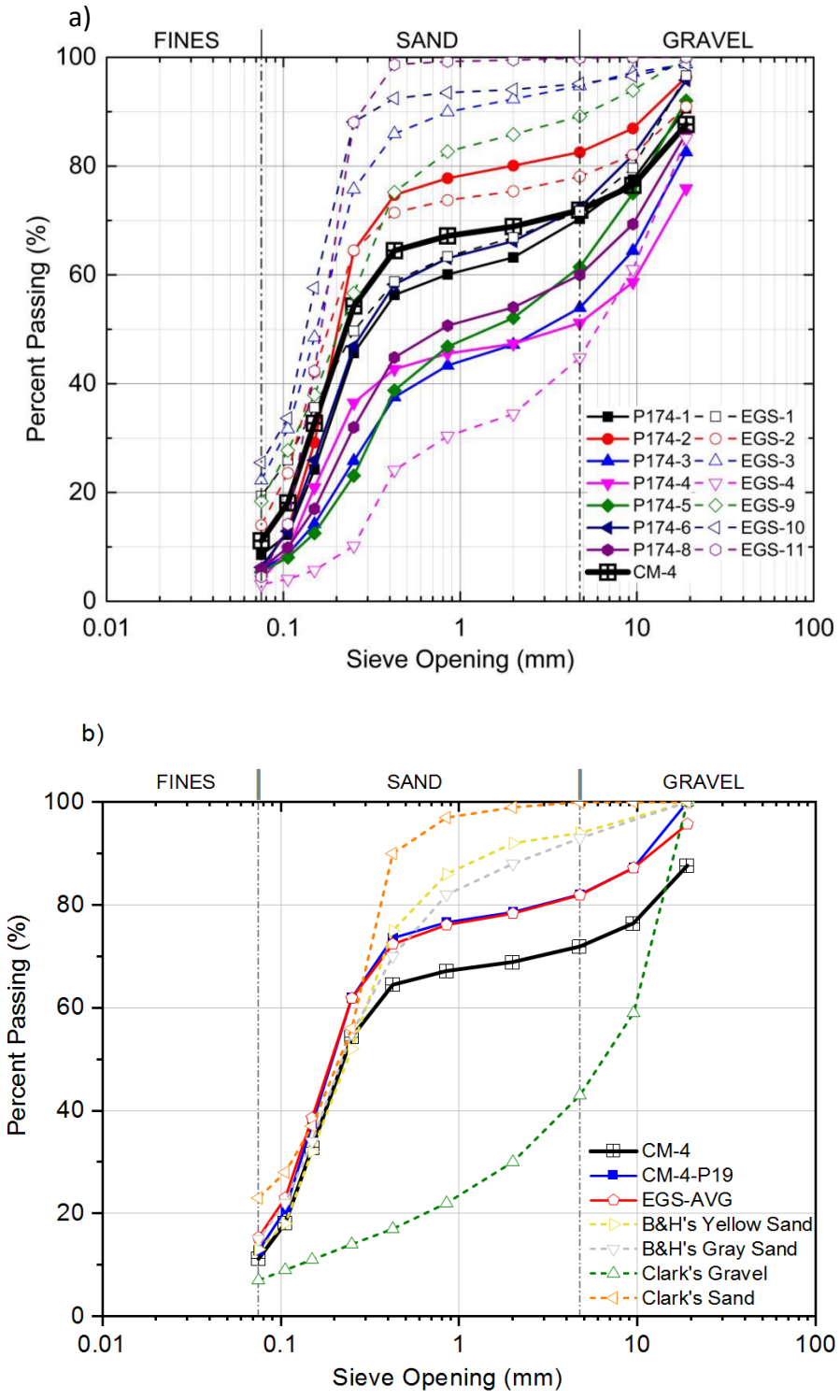

Figure 4-1:Granular Fill Gradations
a) of grab samples (De Guzman, et al., 2018)
b) for comparison with literature results. Includes gradation data replotted from (Clark, 1970); (Botz & Haas, 1980).

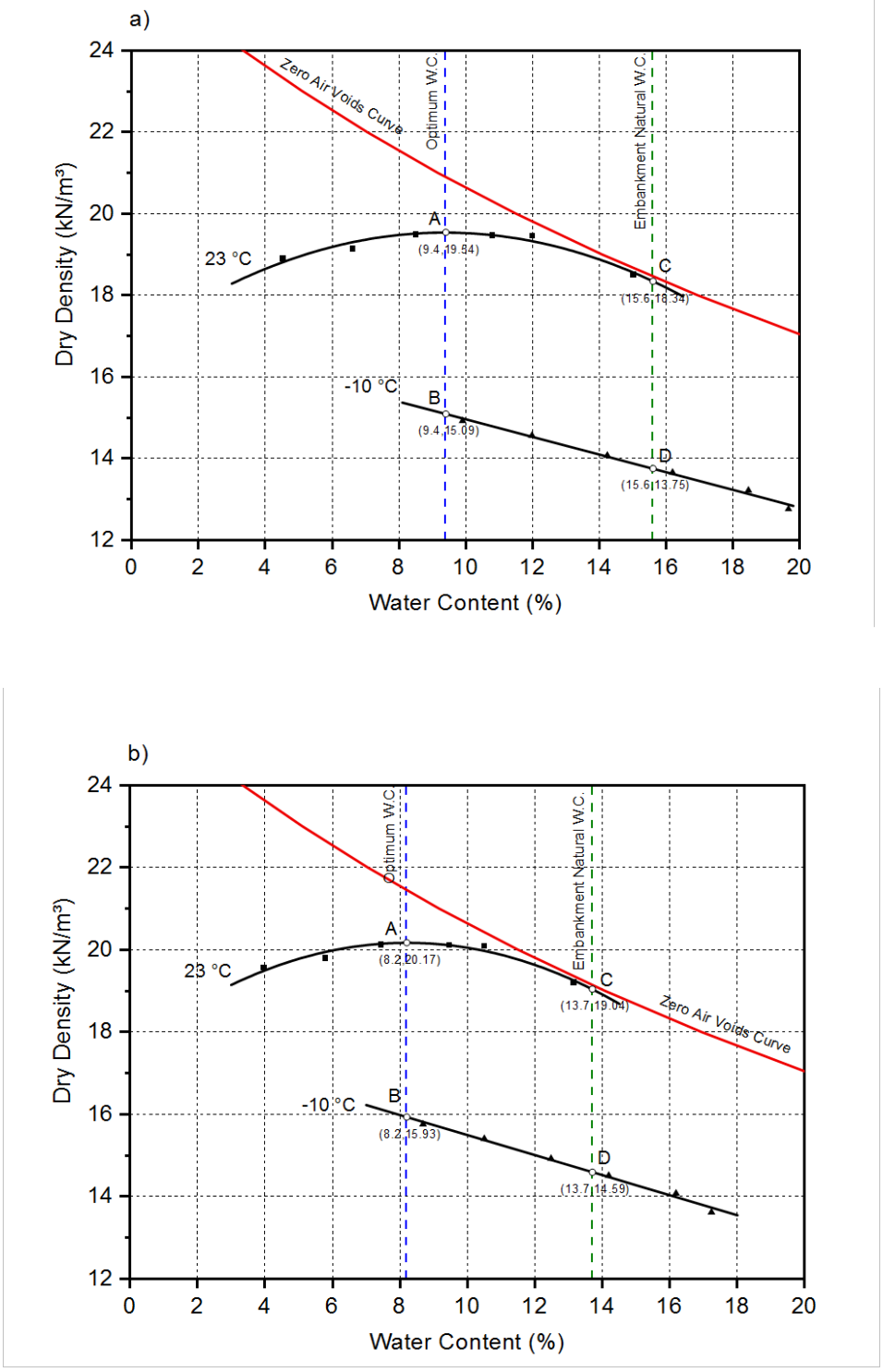

Figure 4-2: Moisture-Density Relationships for ITH Fill material
; a) without oversize particle correction, and b) with oversize particle correction. Uncorrected data obtained from (De Guzman, et al., 2018)

5 Instrumentation Monitoring

5.1.1 Study Period and Data Acquisition Interval

As previously discussed, the scope of this thesis covers the thermal and deformation processes within the first thawing season after construction of the embankment. From review of climate data, the thawing season began shortly after completion of the test embankment construction of 2015/04/20, with sustained positive temperatures continuing until 2015/09/18.

The data acquisition system was programmed to activate and record readings for all the instruments at regular intervals. The recording interval was set for every 3 days during the "warmer" periods of the year (from April to October), and reduced to every 14 days during the "colder" periods of the year (from December to March) to conserve the battery, which performs poorly at cold temperatures. This reduced 14-day interval was considered acceptable given that very little movement would be anticipated while the embankment is frozen during the winter months. Occasional supplemental readings were obtained between these regular intervals when the data acquisition system was manually activated by the Northwest Territories Department of Transportation (NWTDOT) technician on site, who visited to download the saved data recordings and exchange the battery for a fully-charged one.

A lapse in the regular recordings over 60 days occurred between 2015/10/05 and 2015/12/03, believed to be the result of human error when downloading the data on site and failing to reactivate the program to continue with the regularly-scheduled readings. Fortunately, the data lapse occurred after most of the thawing and deformations of interest had already taken place.

A study interval was selected over which the recorded data was analysed, and thermal and deformation models simulated. The study interval was selected to start at the at the completion of the embankment construction and start of instrument recordings on

2015/04/20. This date coincides with the first day in 2015 that daily mean temperatures reached 0 °C.[14]

Given the timing of the thawing season, as well as the available intervals of measured site data, it was chosen to select the study period end date as 2015/10/05. This coincided with the last reading from the instruments prior to the 60-day lapse in recorded data. This ending for the study interval is considered reasonable, given the measured temperature data discussed in the following section shows the embankment was completely frozen by this time. Additionally, maximum recorded deformations occur within this interval.

The selected study period allows for presentation of the measured and modelled temperature and deformation results at 9 timesteps, evenly spaced at 3 week intervals beginning at the start of the study period on 2015/04/20. An additional tenth and final timestep occurring 9 days after the 9th timestep was required to correspond to the final readings on 2015/10/05 at the end of the study interval (prior to the 60-day lapse in data). The use of discrete timesteps allows for ease of comparison between measured data and modelled results, as well as viewing any relationships between temperatures and deformations in the embankment.

These 10 timesteps effectively demonstrate the progression and retreat of the thawing front in the embankment as measured by the temperature and deformation-sensing instrumentation and are used to display the recorded data in the following sub-sections.

5.1.2 Temperature Monitoring

Ground temperatures within the embankment and foundation soils were measured with the thermistors, as well as the temperature sensing nodes within the SAAs and piezometers.

[14] Following 2015/04/20, mean daily temperatures temporarily returned below freezing on several occasions as shown in the mean daily temperature plot in Figure 6-4.

Of the 19 total thermistor nodes in the control section, all but one functioned properly during the duration of the monitoring period. Node TS-C2-G, failed early on after installation for reasons unknown, and therefore data from this node is absent from the study. As the thermistor nodes on any given thermistor string are wired independently from one another, the malfunctioning of any given node does not affect the performance of the remaining nodes within the string (personal communication, RST Instruments Ltd. Technical Specialist, Nov. 2, 2016). The remaining 18 thermistor nodes within the control section appeared to be reading properly. Temperature-sensing nodes within the SAAs and piezometers also were properly reading.

Measured temperatures versus time were plotted at 9 selected temperature-sensing nodes to visualize the development of the thermal regime over the study period. These nodes were selected to provide representative spatial distribution throughout the XS-C cross-section. The selected nodes were distributed at “shallow”, “medium”, and “deep” relative depths throughout the toe, mid-slope, and crest of the embankment. The locations of the temperature-sensing nodes are shown within Figure 3-8, and are summarized in Table 5-1 below:

Table 5-1: List of selected temperature-sensing nodes for plotting vs. time

Relative Depth	Embankment Location		
	Toe	Mid-Slope	Crest
Shallow	TS-C4-A	SAA-CH-A	TS-C1-D
Medium	TS-C4-B	TS-C2-C	SAA-CH-P
Deep	TS-C4-D	SAA-CV-P	TS-C3-D

The measured temperature vs. time plots for the selected nodes are shown in Figure 5-1 alongside the thermal modelling results at each of those given node locations (which are discussed in the thermal modelling chapter).

The following general observations and comments are related to the measured temperature versus time results in Figure 5-1:

- At their respective toe, mid-slope, and crest locations; the “shallow” nodes were the warmest, followed by the “medium”, and “deep” nodes.
- The “shallow” nodes nearest the surface at the toe, mid-slope, and crest showed the reaching of a peak temperature above freezing, then proceeded to decrease, as air temperatures decreased over the season. This is expected as the proximity of these nodes to the surface makes them sensitive to the seasonal changes in air temperature.
- The shallow nodes demonstrated a high variability in successive readings (taken every 3 days), related to climate variations within the larger study period. This variability follows the variability of the air temperatures, which is shown later in Figure 6-4. This is as expected and consistent with the observations on another test embankment constructed with frozen fill (Botz & Haas, 1980). Interestingly, these near-surface ground temperature variations are most noticeable after the temperatures pass above the 0 °C mark. While frozen, short term climate variations are less noticeable in the near-surface ground temperatures since energy into the soil is absorbed as latent heat, required to thaw the frozen soil.
- All of the “medium” and “deep” nodes stayed at sub-zero temperatures throughout the study period. This is as expected, since the design principle of the embankment is to maintain a frozen core and foundation.
- The nodes categorized as “medium” and “deep” demonstrated a continuous increase in temperature over the study period. This steady increase can be attributed to a lag in response time to changes in climate at the surface. Even as air temperatures decreased at the end of the study period, heat trapped in the soil near the ground surface continued to migrate into ground, resulting in the continuing increase in temperature. An exception to this can be seen in TS-C2-C located in the embankment mid-slope, which was close enough to the surface to demonstrate a decrease in temperature near the start of September.
- The range of temperatures experienced over the thawing season was greater within the embankment fill material, compared to the native soil underlying the peat. This is expected since the embankment fill possesses a high thermal conductivity compared to the peat, which tends to insulate the ground beneath it.

With the temperature graphs versus time, it is difficult to visualize ground temperatures within the embankment cross section at a given time. A simplified method of visualizing measured temperature contours at discrete timesteps was originally proposed by the author. This simplified method consisted of contours created in the embankment cross section by interpolating the measured temperatures spatially, between the known temperature node locations. Ultimately this simplified method was not presented in this study as it provided unrealistic temperature contours; most notably at 1) the exterior of the test embankment where extrapolation of temperatures beyond the known temperature nodes would lead to extreme hot or cold unrealistic temperatures; and 2) near material type boundaries which are not accounted for in the interpolation.

From the thermal models however, thermal contours through the embankment cross section at specific times can be generated to achieve the desired visualization. The thermal model results (discussed in the upcoming sections) were in generally good agreement with the measured results, and therefore provide a reasonable qualitative visualization of measured ground temperature contours at specific times during the study period. The thermal model temperature contours are presented Appendix C's Figures C-01 to C-10, each representing one of the 10 selected timesteps discussed in section 5.1.1. The measured temperature data is also superimposed on the thermal model contour data (as values in black text, representing the measured temperature in °C at the adjacent temperature-sensing node location[15]). The following is a summary of general observations made from the modelled temperature contours, but also applicable to measured temperatures:

- The temperature contours show the expected behavior of warming along the exterior surface of the embankment, with the progression of the thawing front advancing deeper into the embankment throughout the thawing season.
- The embankment core and foundation soils remained frozen throughout the entire thawing season, as expected.

[15] Only every third SAA temperature node measurement has been plotted in the figures, for clarity.

- The maximum ground temperatures observed throughout the study period occurred in early-July, along the surface of the embankment (as shown in Figure C-05). This corresponded with the maximum air temperatures over the study period.
- Advancement of the thaw front however continued until 2015/09/05 (as shown in Figure C-08) in most of the embankment. There is a delay between peak air and ground temperatures (early-July), and the timing of maximum thaw penetration (early September).
- The maximum thaw penetration depths at the embankment crest, mid-slope, and toe areas were approximately 2.43 m, 2.17 m (measured perpendicular to the slope), and 0.50 m respectively. (Refer to Figure Figure 5-3 in the following subsection)
- introduced in the following sub-section)
- Towards the end of the thawing season, cooling of the embankment occurred from the exterior moving inwards, as shown in Figures C-08 to C-10.
- Complete freeze-up of the embankment occurred by 2015/10/05, as shown in Figure C-10.
- During the summer, ground temperatures in the native foundation soils directly below the embankment were cooler than the native soil located beyond the embankment footprint. The presence of the embankment insulated the foundation soil beneath it from the warming above. See figures C-05 to C-08.

A comparison between the measured and modelled temperature results is provided in section 6.2.10.

5.1.3 Deformation Monitoring

Deformations in the XS-C cross-section were measured with the SAAs. The horizontally oriented SAA-CH was used to measure vertical deformation, while the vertically oriented SAA-CV was used to measure lateral deformation. The placement of the SAAs within the XS-C cross-section is shown in Figure 3-8.

Relative displacement over the length of each array is calculated by designating a "fixed" point along each SAA. In each of the horizontal and vertical SAAs, one extremity remained embedded within frozen soil over the entire study period, which were selected to represent the fixed segment with assumed zero-displacement[16]. The deformation results therefore rely on the assumption that zero movement occurs at the extremity of the SAA, located in frozen soil. Baseline SAA readings were taken on 2015/04/20, immediately following embankment construction, which served as reference for subsequent relative movements over the course of the study period.

Plots of measured deformation at selected time intervals for SAA-CH and SAA-CV are shown in Figure 5-2. The sign convention for deformation is consistent with the geometry used throughout the study where vertical settlement is negative, and lateral spreading (away from the embankment centreline) is also negative. As expected, the deformations were generally constrained to the exterior portions of the embankment which had thawed, while very little movement occurred within the frozen zones of the embankment.

Figure 5-2 a) shows the vertical settlement originated at the outside of the embankment at the early stages of the thawing season, and advanced towards the centre of the embankment as the thawing front penetrated deeper into the embankment. Maximum vertical settlement over the study period was observed at the outer extremity of the SAA-CH (located at distance of -11.5 m from the centreline), and had a magnitude of 338.0 mm. At all locations along SAA-CH, the magnitude of settlement can be seen to increase at each subsequent timestep, proportionally with the thickness of thawed soil directly below the SAA-CH. The only exception is between the final two plotted timesteps from 2015/09/26 to 2015/10/05, where no additional settlement occurs. This is expected since this corresponds with the freeze-up of the embankment.

[16] Note this is contrary to the interpretation presented in (De Guzman, et al., 2015), in which the SAA-CH position was deemed fixed at the opposite extremity of the array (-11.5 m from C/L). The fixing configuration used in the current study is considered more realistic given the relatively fixed frozen state of the soils near the embankment centre, and was in good agreement with temperature measurement results.

Unexpected upward movement of the SAA-CH can also be seen in Figure 5-2 a). The upward movement occurs towards the centre of the embankment, between a distance of 3.5 and 6.0 m from the embankment centreline. The upward movement begins to occur on 2015/07/25, and progresses until the final plotted date of 2015/10/05, where it reaches a maximum value of 16 mm, located 5.5 m from the embankment centreline. The exact reason for the uplift in SAA-CH is unknown. It is noted the uplift is relegated to the portion of the SAA that remained frozen within the embankment core over the thawing season. It is hypothesized the uplift may be attributed to flexural bending of the PVC pipe which houses the SAA, as the opposite end is pulled down with the thawing soil. An alternative hypothesis is that the uplift may be caused by ice lens formation within the frozen embankment core below the SAA.

Figure 5-2 b) shows lateral deformation in SAA-CV originating nearest the surface at early stages of the thawing season, and similarly increasing with depth as the thawing season progressed. The observed lateral deformation was directed away from the centreline, showing the expected lateral spreading behaviour within the thawed portion of the embankment. Maximum lateral displacement over the study period was observed at the upper extremity of the SAA-CV (located at elevation 22.31 m), and had a magnitude of 185.7 mm. These measurements are in agreement with general observations from the site, where longitudinal cracking was observed along the crest of the embankment (see Photo 26 of Appendix B).

Measured SAA deformations are also shown in conjunction with the thermal model contours and measured temperatures in Figures C-01 to C-10 in Appendix C. Within each figure representing a different timestep over the study period, the baseline SAA readings are shown alongside the measured (to-scale) deformations at that particular timestep. In Figures C-01 to C-03, the difference between the baseline measurement and deformation is indiscernible, however becomes much more noticeable in Figures C-04 to C-10 as the thaw front begins to intersect the SAAs. The figures highlight the strong relationship between the position of the thawing front and the deformations over the first thawing season.

A schematic of maximum deformations within the embankment is presented in Figure 5-3. The schematic illustrates the maximum depths of thaw penetration at different areas of the embankment XS-C cross section, while also showing the volume reduction associated with thaw consolidation. The ground surface profile of the as-built condition immediately following construction is shown as the upper boundary of Region A, and the ground surface profile at the end of the thawing season (based on the March 2016 survey) is shown as the as the lower boundary of Region A. The base of the thawing zone, taken as the modelled zero-degree isotherm on the date of maximum thaw penetration on 2015/09/05 is shown as the lower boundary of Region B. Region A represents the cross-sectional area reduction resulting from thaw consolidation, and is 7.62 m^2. Region B represents the cross-sectional area of the thawed zone, and is 33.50 m^2. The combined Regions A and Region B represent the total cross-sectional thaw area of 41.12 m^2.

The thaw consolidation volumetric strain can be calculated by dividing Region A by the combined Regions A and B, equalling -18.5%. For comparison, the experimental literature results in Figure 2-10 for a similar soil type show a volumetric strain of -12%, when using the same estimated embankment frozen dry density of 1488 kg/m^3 (14.59 kN/m^3). Conversely, the measured volumetric strain of -18.5% corresponds to a frozen dry density of approximately 1260 kg/m^3, when referring to the results from Figure 2-10.

Given the magnitude of observed thaw settlement over the first thawing season, it can be concluded the construction practice of overbuilding by 0.3 m is justified. Given the magnitude of thaw settlement even exceeds this 0.3 m amount, additional conservatism through placement of an even thicker overbuild may be justified.

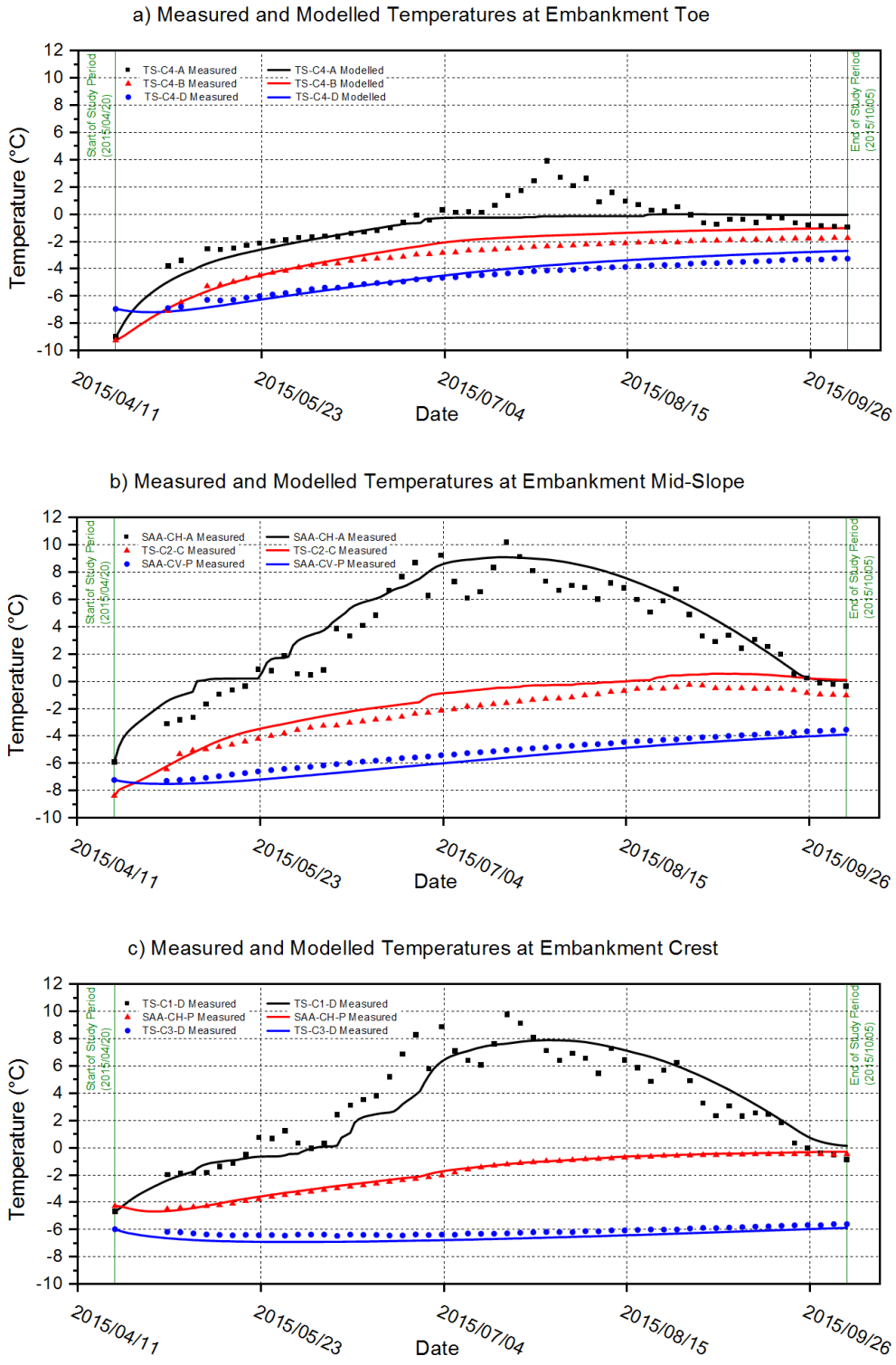

Figure 5-1: Measured and Modelled Temperatures vs. Time at a) Embankment Toe, b) Mid-Slope, and c) Crest

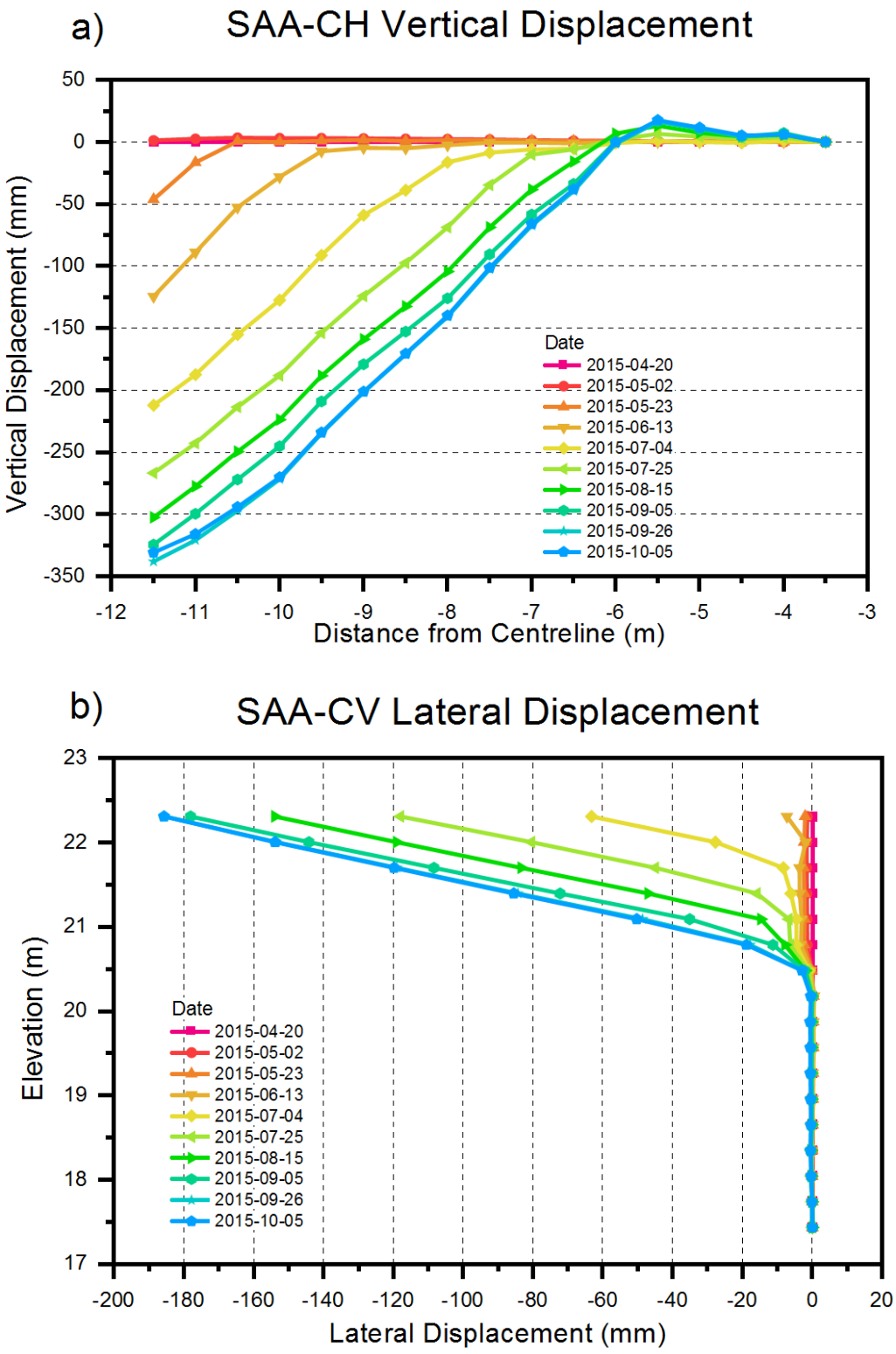

Figure 5-2: Measured SAA deformations in a) Vertical settlement, SAA-CH and b) Lateral displacement, SAA-CV

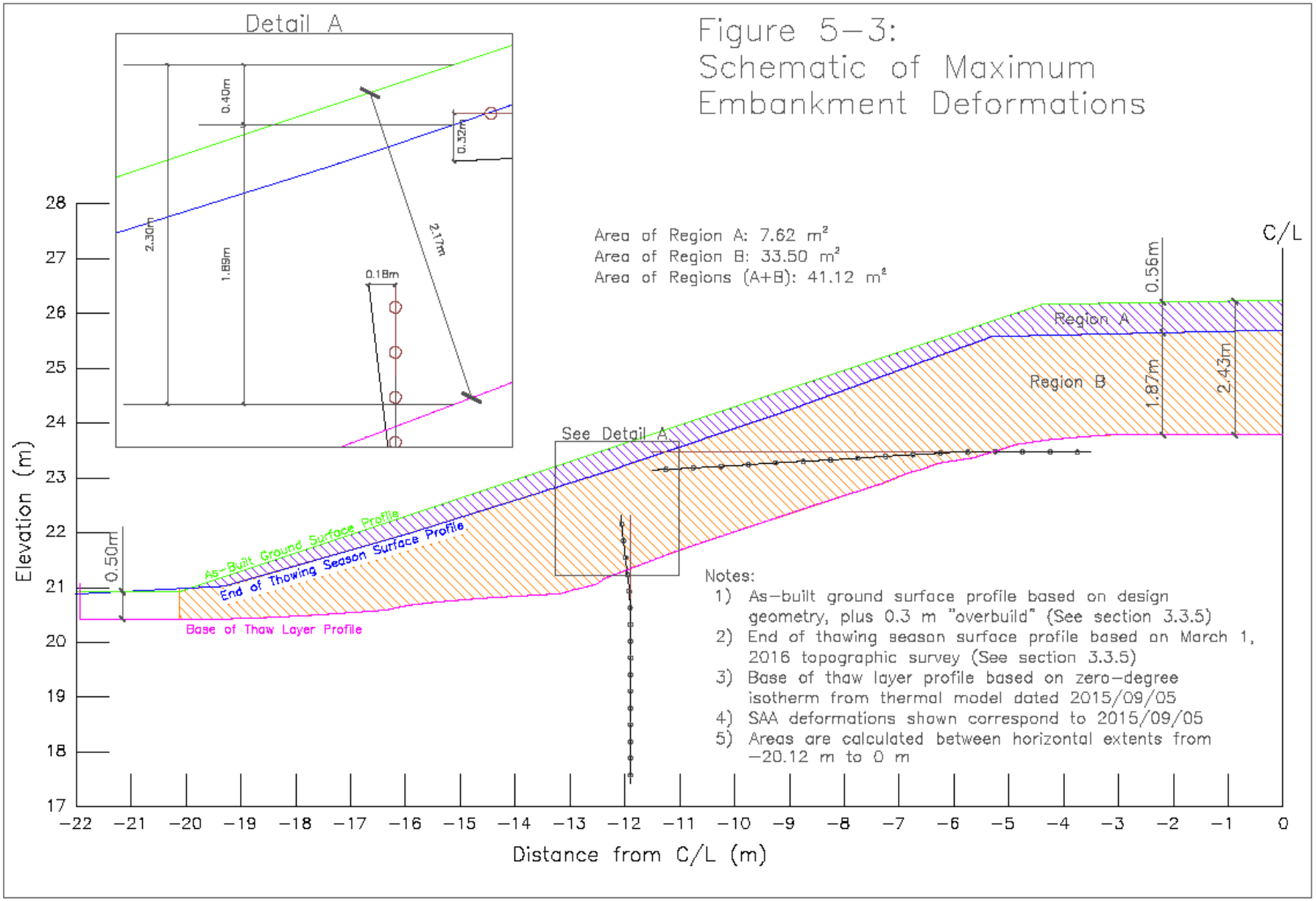

Figure 5-3: Schematic of Maximum Embankment Deformations

6 Numerical Modelling

6.1 Introduction and Modelling Objectives

Numerical modelling in the realm of geotechnical engineering is a tool that can be used to grasp an understanding of physical processes observed in real world applications. The numerical modelling simulated the processes of heat transfer and stress-deformation in the test embankment. The simulations were conducted over the first thawing season following construction, using the information obtained from the field study, laboratory testing, and literature review.

As previously outlined in section 1.3, objective 3) of this research was the development and calibration of numerical models with field data and laboratory test results. This is presented in the thermal and deformation modelling sections to follow which include the modelling processes, theory, model details and inputs, followed by results. Objective 4) of this research was to investigate the important factors affecting the performance of the embankment during and shortly after construction, which are covered in the respective discussion sections as well as the sensitivity analysis sections.

6.2 Thermal Modelling

6.2.1 Methodology

The goal of the thermal modelling was to obtain a working model, able to simulate ground temperatures within the test embankment over the course of the thawing season. Thermal modelling of the embankment was conducted by finite element method numerical modelling using the commercially-available software Temp/W published by Geo-Slope International Ltd. The software is capable of analyzing heat transfer through porous media containing soil, water, ice, and air. The software is configured to accept inputs for soil parameters, model boundary conditions, and geometry, and is used to simulate the thermal ground regime.

Initial parameters were selected from the results of the laboratory testing and the available literature. Published relationships between thermal properties and known physical soil properties from laboratory tests were used when possible.

Given the many parameters in the thermal model, it is possible in theory to replicate certain measured field results with different combinations of parameter calibration values. For example, a specified thaw depth within the embankment fill can be achieved by using a high thermal conductivity, accompanied by a relatively low thawing n-factor. Alternatively, the same thaw depth can be obtained using a lower thermal conductivity, and a comparatively high thawing n-factor. In cases like this, the approach taken in selection of correlated parameters was to prioritize individual parameters in which there was greatest confidence in their accuracy, while still maintaining the second correlated parameters within reasonably accepted values.

Given the many variables affecting the thermal energy balance at the test site, the thermal modelling process was broken into two separate parts; the pre-construction model and the post-construction model. This allowed for the calibration of certain parameters independently of others, simplifying the overall modelling process. Calibration of pre-construction model was completed first. The calibrated parameters obtained from the pre-construction model were then incorporated into the post-construction model, without requiring further adjustment.

Both the thermal and deformation analyses were simulated over the same study period interval from 2015/04/20 to 2015/10/05, equal to the data acquisition interval described in section 5.1.1. This allows for consistent comparison between the field measurements, and the thermal and deformation model results.

6.2.1.1 Pre-Construction Model

The purpose of the pre-construction thermal model was to calibrate parameters that were independent of the embankment construction. These included material thermal properties for the peat and native foundation soils, and surface n-factors for the peat, which are discussed in the upcoming sections.

The pre-construction model sought to simulate the ground thermal regime over a typical year, without the embankment present. The pre-construction model relied on the premise that prior to the embankment construction, a typical ground temperature profile would have existed, with an established DMZAA and annual temperature fluctuations similar to the trumpet curve shown in Figure 2-1.

A year-long climate boundary function was created and simulated to repeat annually, until a realistic annual ground-temperature profile was established. Calibration of the pre-construction thermal model was conducted by adjusting the model parameters until the desired ground temperature profile was obtained, including stable long-term temperatures below the DMZAA. The successfully calibrated parameters could then be used in the subsequent post-construction model.

6.2.1.2 Post-Construction Model

The post-construction model sought to simulate the embankment thermal regime over the thawing season. The model used the previously-calibrated parameters from the pre-construction model, along with new thermal parameters for the added materials and boundary conditions corresponding to the new embankment construction. The new parameters calibrated within the post-construction model included thermal properties of the embankment fill, and surface n-factors along the crest and sideslope of the embankment.

Calibration of the post-construction thermal model was conducted by fitting the modeled results to the thermal regime observed at the embankment test site. This was done by comparing the results of modeled versus measured temperature plots taken throughout the embankment over time.

6.2.2 Theory

This section covers the equations used to calculate heat conduction, which are used in the Temp/W software.

The heat flux due to conduction is defined in Equation 6-1 as:

6-1

$$q = -k\frac{\partial T}{\partial x}$$

Where:

$q =$ heat flux

$k =$ thermal conductivity

$T =$ temperature

$x =$ distance

The equation above indicates that heat flux due to conduction is a function of the soil thermal conductivity and the temperature gradient. The negative sign denotes the direction of heat flow is from higher temperatures to lower temperatures. (Geo-Slope International Ltd., 2010)

The governing differential equation used in the Temp/W thermal model is shown in Equation 6-2 (Geo-Slope International Ltd., 2010):

6-2

$$\frac{\partial}{\partial x}\left(k_x\frac{\partial T}{\partial x}\right) + \frac{\partial}{\partial y}\left(k_y\frac{\partial T}{\partial y}\right) + Q = \lambda\frac{\partial T}{\partial t}$$

Where:

$k_x =$ thermal conductivity in the x-direction

$k_y =$ thermal conductivity in the y-direction

$T =$ temperature

$Q =$ applied boundary flux

$\lambda =$ capacity for heat storage

$t =$ time

Equation 6-2 indicates the change in the heat flux within an elemental volume of soil over a given time is equal to the change in stored heat energy (Geo-Slope International Ltd., 2010). The capacity for heat storage term, λ is defined as follows:

6-3

$$\lambda = c + L\theta \frac{\partial \theta_u}{\partial T}$$

Where:

$c =$ volumetric heat capacity

$L =$ latent heat of fusion of water

$\theta =$ volumetric water content of the soil

$\theta_u =$ unfrozen water content ratio (value between 0 and 1)

$T =$ temperature

The volumetric heat capacity term, c is a material property defined for frozen and unfrozen conditions, which is further discussed in section 6.2.8.4. The second term in Equation 6-3 represents the capacity for heat storage attributed to latent heat of fusion. This is a function of the unfrozen water content ratio θ_u, which itself is a function of temperature. Unfrozen water content functions are touched upon in section 6.2.8.2.

Substituting Equation 6-3 into Equation 6-2 yields the complete differential equation used in the thermal model:

$$\frac{\partial}{\partial x}\left(k_x \frac{\partial T}{\partial x}\right) + \frac{\partial}{\partial y}\left(k_y \frac{\partial T}{\partial y}\right) + Q = \left(c + L\theta \frac{\partial \theta_u}{\partial T}\right)\frac{\partial T}{\partial t}$$

6.2.3 Geometry

6.2.3.1 Pre-Construction Model

The geometry used in the pre-construction model was relatively simple as it simulates a cross section of flat undisturbed ground, without the presence of the embankment. Because of this geometry, horizontal heat flow would be balanced on both sides, resulting in a net horizontal heat flow equal to zero. As such, the horizontal extents of the pre-construction model could be limited to the width of a single element (chosen as 0.25 m), in order to minimize computation requirements. The depth of the pre-construction model was extended to 20 m below the ground surface. Although much deeper than the field borings, this was chosen so that a depth of mean zero annual amplitude could be clearly established within the model. The pre-construction thermal model geometry is shown in Figure 6-1.

6.2.3.2 Post-Construction Model

The geometry used in the post-construction thermal model was taken at cross-section XS-C, near the centre of the control section of the embankment. This allowed for use of a consistent cross-section in both the thermal and deformation models. The model geometry only required one half of the embankment, corresponding to the instrumented half of the embankment. The horizontal extents of the model were extended to 40 m from the embankment centreline. This distance was found sufficient to avoid influence on temperatures near the embankment toe.

The geometry of the post-construction thermal model was extended deeper than the measured temperature readings to better simulate the behaviour of the overall ground thermal regime. It is later shown that a DMZAA of 14 m was calculated for the site using the pre-construction thermal model. As such, the vertical extents of the post-construction

model were increased to that same depth of 14 m (elevation 7 m). The post-construction thermal model geometry is shown in Figure 6-2.

The finite element meshing pattern consists of a mixed quadrilateral and triangle unstructured mesh. This pattern is recommended versus a simple quadrilateral-only mesh as it allows for more evenly sized elements given the somewhat irregular, non-rectangular embankment geometry (Geo-Slope International Ltd., 2010). In addition, the presence of quadrilateral elements at the ground surface is preferable to triangular elements in the numerical modelling as the heat flux gradients are usually steeper in the direction perpendicular to the ground surface. The post-construction model mesh consists of a total of 21105 elements with a nominal element size of 0.5 m in the locations of deep foundation soils, and reduced to 0.125 m in the upper approximate 2 m of the ground surface as well as within the embankment for finer resolution in the areas of greatest heat flux. The meshing pattern is also shown in the model geometry figures.

To further accommodate for the relatively large climatic variations occurring near the ground surface, surface layers have been incorporated into the thermal model. Within the Temp/W software, the surface layers provide fine discretization perpendicular to and near the ground surface. The surface layers in the post-construction model consisted of 10 layers, each 0.02 m thick, for a total surface layer thickness of 0.2 m.

6.2.4 Flux Boundary Conditions

Flux boundary conditions were used to specify the heat flux in the thermal models and included both zero-flux boundaries and a geothermal heat flux boundary, as shown in Figure 6-1 for the pre-construction model and Figure 6-2 for the post-construction model. The zero-flux boundaries were located vertically on each side of the problem geometry, and the geothermal heat flux boundary was located along the base of the problem geometry.

6.2.4.1 Zero-Flux Boundaries

Zero-flux thermal boundaries are used in both the pre-construction and post-construction models.

In the pre-construction model, zero-flux boundaries were applied vertically on both the left and right sides of the model geometry. As previously discussed, due to the symmetry along the vertical axis of the problem, horizontal heat flow would be balanced on both left and right sides, resulting in a net horizontal heat flow equal to zero.

In the post-construction model, zero-flux boundaries were also applied vertically on both the left and right sides of the model geometry. The zero-flux boundary at the right side of the model represents the net-zero heat transfer due to the symmetry of the embankment (as only one half of the embankment is modelled).

Similarly, the flux along the left side of the model can be set to zero because of the symmetry of the problem, as the tundra extends further on the left side beyond the modelled geometry. The distance between the embankment and the zero-flux boundary condition on left side of the model has been sufficiently extended so that the modelled embankment temperatures are not affected.

6.2.4.2 Geothermal Heat Flux

A constant unit flux boundary condition was implemented at along the bottom boundary of the model to simulate the geothermal heat flux. The magnitude of geothermal heat flux varies throughout the world. In a study of the permafrost regime in the Mackenzie Delta and Beaufort Sea region, (Allen, et al., 1988) assumed a constant geothermal heat flux of 60 mW/m². This was supported by heat flux values calculated at various locations along the Alaskan arctic coast, and the uniformity of deep temperature gradients across the Mackenzie Delta region. This 60 mW/m² geothermal heat flux value was adopted for the thermal models in this thesis, and was applied as a constant flux boundary condition along the bottom of the model geometry in both the pre-construction and post-construction models.

6.2.5 Climate Boundary Condition

Climate boundary conditions were created to simulate the energy balances at the ground surface, over the course of the study period. Each climate boundary condition consisted of: 1) an air-temperature function, and 2) a modifying n-factor function to account for the

differences between air temperature and those at the ground surface. The climate boundary conditions were applied at the ground surface, and are shown in Figure 6-1 and Figure 6-2 for the pre-construction and post-construction models respectively.

Differing air-temperature functions were used in the pre-construction and post-construction models as will be discussed. Differing n-factor modifying functions were also used to account for different heat transfer conditions at the: 1) peat surface, 2) embankment sideslope, and 3) embankment crest.

6.2.5.1 Air Temperature Functions

As discussed in section 3.2.3, the Trail Valley climate station was selected as the most representative climate station from which to obtain air-temperature data for the test site. Daily average temperature readings from the climate station were downloaded to create the required air temperature functions.

Daily fluctuations in air temperatures can results in instability in modelling, and deviation between modeled and measured near-surface ground temperatures. To minimize this effect, average daily air temperatures can be smoothed over a longer period (Darrow, 2011). Smoothing of the air temperature data was conducted by fitting the daily average air temperatures to a sine function. This approach has successfully been employed in the thermal modelling of highway embankments over permafrost (Flynn, et al., 2016). For the present study, two separate smoothed air temperature sine functions were fitted; one for the pre-construction model, and another for the post-construction model.

The pre-construction model air temperature function sought to represent temperature fluctuations for the test site over a typical year. To reduce the influence of annually varying temperatures, daily average air temperatures over a 3-year period were used (from 2012/12/14 to 2015/12/14). The daily average air temperature data for this period can be seen in Figure 6-3, along with its fitted sine function. The pre-construction air temperature function can be represented by the equation:

6-5

$$T_{pre}(t) = 19.95 \sin\left(2\pi\left[\frac{t + 233.7}{365}\right]\right) - 7.62$$

Where:

$T_{pre} =$ Air temperature in the pre-construction model [°C]

$t =$ time [days]

For the post-construction model, it was desired to represent smoothed air temperature conditions experienced at the site during the selected 168-day study period (from 2015/04/20 to 2015/10/05). The temperature data for this study period is included within the larger 3-year period previously discussed. A closer view of the measured air temperature data over the 168-day study period is shown in Figure 6-4. The figure also includes the fitted sine function for the post-construction model air temperature, which is represented by the equation below:

6-6

$$T_{post}(t) = -17.22 \sin\left(2\pi\left[\frac{t + 244.94}{365}\right]\right) - 5.31$$

Where:

$T_{post} =$ Air temperature in the post-construction model [°C]

$t =$ time [days]

As an alternative to the fitted sine function for the post-construction model, daily mean air temperatures from the Trail Valley climate station (shown as the blue data points in Figure 6-4) were used in a trial run to compare difference between using the fitted sine function and daily air temperatures. The model results for this trial run are shown in Figure 6-5. Generally, the trial model using the daily air temperature function showed good responsiveness to the daily temperature fluctuations, especially near the ground surface

expected. The air temperature function model generally resulted in an overprediction of ground temperatures. As such, a separate calibration for the soil parameters and n-factors would be recommended to better fit the daily air temperature function model to the measured data. For simplicity, this was not conducted within the scope of the current study. Further research using daily air temperature data versus a smoothed sine function is recommended, with care to avoid numerical model instabilities if there are sudden changes in daily air temperature.

Air thawing and freezing indices were discussed previously in section 3.2.3. The air thawing and freezing indices calculated from the fitted sine functions are compared against the indices calculated from the raw temperature data in Table 6-1 below.

Table 6-1: Summary of Freezing and Thawing Indices

Air Temperature Dataset Period	Calculated Thawing Index (°C*days)		Calculated Freezing Index (°C*days)	
	Raw Data	Sine Function	Raw Data	Sine Function
Pre-Construction(1)	1179(3)	1098	3967(3)	3881
Post-Construction(2)	1187	1128	N/A	N/A

Notes:

1) Refers to pre-construction model temperature dataset, representing 3-year period from 2012/12/14 to 2015/12/14.

2) Refers to post-construction model temperature dataset, representing 168-day study period from 2015/04/20 to 2015/10/05.

3) Represents average annual thawing index within the period.

The freezing index is not calculated for the post-construction air-temperatures since the post-construction dataset does not include the freezing season. It is noted the thawing and freezing indices calculated for the fitted sine functions give lower index values than their

"raw data" counterparts. This means the smoothing of the sine functions produced more mild seasons, with less extreme hot or cold days compared to the raw un-smoothed data. The difference is relatively small however and considered acceptable for this study. The higher thawing indices for the post-construction cases versus the pre-construction cases signify the post-construction 2015 thawing season was warmer than average.

6.2.5.2 N-Factors

The energy balance at the ground surface is a complex process, influenced by many factors including air temperature, solar radiation, wind, soil properties, moisture, and snow and vegetative cover (Klene, et al., 2001). N-factors represent an empirical method to summarize the many factors affecting of the energy fluxes at the ground surface.

The n-factor provides a relationship between the air temperatures and the temperatures at the ground surface. This is convenient in estimating ground surface temperatures since air temperature data is typically available for most sites.

The two types of n-factors are the freezing n-factor, n_f; and the thawing n-factor, n_t; which are defined by the following equations (Andersland & Landanyi, 2004):

6-7

$$n_f = \frac{I_{sf}}{I_{af}}$$

6-8

$$n_t = \frac{I_{st}}{I_{at}}$$

Where:

$I_{sf} =$ surface freezing index [°C*days]

$I_{af} =$ air freezing index [°C*days]

$I_{sf} =$ surface thawing index [°C*days]

$I_{sf} =$ air thawing index [°C*days]

In the thermal models, the ground surface temperature is calculated in each new timestep using the following equation (Geo-Slope International Ltd., 2010):

6-9

$$T_s = n\left(T_a - T_{phase}\right) + T_{phase}$$

Where:

$T_s =$ Temperature at the ground surface [°C]

$n =$ n_f or n_t, corresponding to T_s calculated from the previous timestep

$T_a =$ Air temperature [°C]

$T_{phase} =$ Phase change temperature

The phase change temperature represents the cut-off between the freezing and thawing season, with a value of 0 °C used in the models.

With the use of n-factors it is important to select values that are appropriate for the given ground surface type. (Lunardini, 1978) summarized freezing and thawing n-factor values for many engineered and several natural surfaces. (Taylor, 1995) summarized field-measured n-factors for natural areas in the Mackenzie Valley area, however mostly applicable to forested areas. Given the many natural land-cover types that exist, (Klene, et al., 2001) identified the need for additional information on soil surface temperature data.

The calibrated n-factor values used in the models are shown in the table within Figure 6-5. Separate freezing and thawing n-factors were assigned to the surface of the peat, the embankment slope, and the embankment crest.

For the peat, selection of the n-factors was based off a study of thawing n-factors for natural surface areas in the Kuparuk River Basin in northern Alaska by (Klene, et al., 2001). Of the five land cover classes included in their study, the description provided for the "moist acidic tundra" closely matched the native peat surface found at the ITH test site, as discussed in section 3.2.2. The availability of a thawing n-factor applicable to the peat surface at the test site is considered very fortunate. The freezing n-factor for the peat was subsequently determined through calibration of the pre-construction model.

For the embankment fill slope and crest, the initial estimates for n-factors were based off typical published literature values for gravel surfaces in northern regions (Andersland & Landanyi, 2004, p. 59). Adjustments to these initial estimates were made throughout the calibration process.

6.2.6 Initial Temperature Conditions

Initial conditions must be assigned in all transient models. In the pre-construction model, values for initial temperature conditions were not critical, since the model was run until equilibrium temperatures (quasi-steady-state conditions) were obtained below the DMZAA. As such, differing initial temperature conditions could be used which would lead to the same eventual result, provided the model simulated enough time for the temperatures to stabilize.

The post-construction model results were much more sensitive to the initial temperature conditions since the results of interest (thawing season) begin immediately in the first timesteps of the model. Initial temperature conditions in the post-construction model were selected to match the field conditions at the start of the model on 2015/04/20. Temperature conditions were assigned using a temperature "spatial function" as termed in the Temp/W software. The user inputs temperatures at discrete points throughout the space, and the software generates a spatial function krigged surface (a type of interpolation), to generate temperatures throughout the two-dimensional domain.

The temperature input points for the spatial function were derived from two sources. The first source was the measured field temperatures corresponding to the model start date of

2015/04/20. These measured temperature readings however only extend approximately 6 m below ground surface (elevation 15 m), while the post-construction model geometry required initial temperature conditions for the full model domain extending to approximately 14 m below ground surface (elevation 7 m). Temperatures between 6 and 14 m below ground surface were therefore estimated using the computed ground temperatures from the pre-construction model on 04/20.

The spatial function of the initial temperature conditions for the post-construction model is equivalent to the first timestep of the model on 2015/04/20, and can be seen in Figure C-01 of Appendix C.

6.2.7 Material Types

The materials in the thermal models were established from the known construction procedure for the embankment, stratigraphy encountered during drilling for instrument installation, and through literature review of the local geology. The material types used in the models were “peat”, “native soil”, and “granular fill”. Material types for the pre-construction model are shown in Figure 6-1. The post-construction model used the same general soil profile as the pre-construction model, with the addition of the embankment granular fill, as shown in Figure 6-2.

The peat material consists of a 200 mm layer overlying the native soil. The thickness of the peat layer was based on the average thickness observed during drilling on site. It should be noted the layer of peat was maintained at the underside of the embankment fill material in the post-construction model. This reflects the construction practice used at the test site (and over the entire highway), which was to place fill materials at the surface without disturbing the tundra vegetation.

Careful consideration was made in the selection of material type to represent the native soil, underlying the peat. In the ITH thermal modelling engineering report by Amec Foster Wheeler (Amec Foster Wheeler, 2016), the soil underling the peat is termed “native clayey soil”, and has thermal properties which are consistent with what would be expected for a clay-type soil. This presence of clay is however contrary to the

observations during drilling on site, as well as what would be expected from the local geology. Given that the Amec Foster Wheeler study was used to classify the entire Inuvik-Tuktoyaktuk Highway route, it is believed this "native clayey soil" was likely selected as a generic representative subsoil for the entire highway, and is not considered representative of the native soil encountered at the test site[17].

From the review of local physiography and geology discussed in section 3.2.1 it is known that beneath the surficial peat layer, the area is covered by Pleistocene deposits consisting of sand, gravel, and ice, which themselves overly the Iperk sequence, which also consist of sand, gravel, and ice. It was also noted the underside of the Pleistocene deposits and top of the Iperk sequence are not well delineated. Given the similar constituents within the Pleistocene deposits and Iperk sequence, it was chosen to group these geologic layers as one, termed "native soil" for modelling purposes. Within this thesis, the "native soil" layer should be considered as a mix of sand and gravel, with ice present in the seasonally frozen portion. This description is also consistent with the observations made during drilling into the native soil layer for the instrumentation installation, where gravel and ice were encountered.

The granular fill material layer as shown in Figure 6-2 represents the imported fill, modelled to match the known embankment geometry.

6.2.8 Material Properties

The following sections outline the material properties used in the thermal analyses and justification for the values selected. The selected material properties were the same in both the pre-construction and post-construction models, and are summarized in the table within Figure 6-5.

[17] A geological review suggests clay-type soils are be more representative of the native soils southern portion of the ITH highway alignment.

Figure 6-5 includes the material properties of volumetric water content, heat capacity, and thermal conductivity which are all direct input parameters in the thermal model. The figure also includes the phase relationship parameters of gravimetric water content, dry unit weight/density, saturation, specific gravity, and void ratio. While not direct inputs in the model, these have been included to show basic soil phase relationships have been maintained and are consistent with one another, and as cross-reference since some of the thermal properties possess a relationship to these phase relationship properties.

6.2.8.1 Water Content

A water content of 13.7 % was selected for the embankment fill material. This was taken directly from the oversize-corrected average water contents of the 7 fill samples collected during embankment construction as outlined in section 4.3.2.

A wide possible range of possible water contents could exist for both the peat and native soil materials. This is due to the ability of peat to absorb significant amounts of water, and because of the high variability of ice content that could be present within the native soil. Values for the peat and native soils were selected to fit within the wide range of values from literature, and were narrowed by seeking consistency in the relationships between thermal conductivity, water content, and dry density discussed earlier in section 2.4.2 and shown in Figure 2-2 and Figure 2-4.

6.2.8.2 Unfrozen Water Content

At sub-zero temperatures, some fraction of pore water can still exist in liquid form. This is because pore water adsorbed on the soil mineral particle surface is more resistant to freezing. This phenomenon is of most importance in fine-grained soils, due to their high specific surface area (Tsytovich, 1975). For coarse grained-soils, this can be ignored since virtually all the pore water becomes ice at 0 °C (Farouki, 1986). The unfrozen water content for the granular fill and native soil were therefore assumed to be zero in the models.

Peat soils can support relatively high unfrozen water contents at sub-zero temperatures (Keune & Hoekstra, 1967). Testing on peat soils by (Nagare, et al., 2012) showed a

single soil freezing characteristic curve could be established for the peat, even with different initial water contents. This curve was incorporated into the Temp/W models as the unfrozen volumetric water content function for the peat material, and is shown in Figure 6-9.

6.2.8.3 Dry Unit Weight

The dry unit weight is not a direct parameter in the thermal modelling equations, however the following sections will show the parameters of heat capacity and thermal conductivity are dependent on the dry unit weight (or similarly density) of the soil. Emphasis was therefore placed on having a representative estimate for dry unit weights of the materials.

The selected value for the dry unit weight of the compacted fill was 14.59 kN/m³, which is thoroughly discussed in section 4.4.2. Using soil phase relationships, the corresponding saturation of the compacted frozen fill material was 46.1%, providing a sense of the relatively low degree of saturation for this material.

Dry unit weight for the peat was taken from (Amec Foster Wheeler, 2016), while the value for the native soil was estimated using the earlier discussed relationships shown in Figure 2-2.

6.2.8.4 Heat Capacity

The heat capacity (or mass specific heat) of a soil is defined as the amount of heat required to raise the temperature of a unit mass of the soil by 1 degree and is expressed in units of kJ/kg/°K (Farouki, 1986).

The heat capacity of a substance is related its internal energy, including the mass of the substance itself; and the microscopic kinetic energy from the movement of particles at the molecular level (Lunardini, 1988, p. 6). The heat capacity of a soil can be calculated from the respective mass fractions and heat capacities of the different soil constituents. (Andersland & Landanyi, 2004):

6-10

$$c = \frac{1}{m}(c_s m_s + c_w m_w + c_i m_i + c_{air} m_{air})$$

Where:

$c =$ heat capacity [kJ/kg/°K]

$m =$ total soil mass [kg]

$c_s, c_w, c_i, c_{air} =$ heat capacities of solids, water, ice, air [kJ/kg/°K]

$m_s, m_w, m_i, m_{air} =$ mass of solids, water, ice, air [kg]

It is often useful to express heat capacity in terms of unit volume, known as volumetric heat capacity, c_v. The volumetric heat capacity is the product of the heat capacity and the density, ρ.

6-11

$$c_v = \rho c$$

Using the relationship between density, mass, and volume; together with Equation 6-11, Equation 6-10 can be expressed in terms of volumetric heat capacity:

6-12

$$c_v = c_{vs} x_s + c_{vw} x_w + c_{vi} x_i$$

Where:

$c_v =$ volumetric heat capacity [kJ/m³/°K]

$c_{vs}, c_{vw}, c_{vi}, =$ volumetric heat capacities of solids, water, ice [kJ/m³/°K]

$x_s, x_w, x_i, =$ volume fractions of solids, water, ice [m³/m³]

Note the very small air term has been dropped in Equation 6-12 above.

Using established ratios of heat capacity for the different soil constituents in relation to water, the volumetric heat capacity of frozen and unfrozen soils can be calculated using the following equations:

6-13

$$c_{vu} = \left(\frac{\rho_d}{\rho_w}\right)\left(0.17 + 1.0\frac{w}{100}\right)c_{vw}$$

and

6-14

$$c_{vf} = \left(\frac{\rho_d}{\rho_w}\right)\left[\left(0.17 + 1.0\frac{w_u}{100}\right) + 0.5\left(\frac{w - w_u}{100}\right)\right]c_{vw}$$

Where:

c_{vu}, c_{vf} = volumetric heat capacity of unfrozen, and frozen soils [kJ/m³/°K]

ρ_d, ρ_w = unit mass for dry soil, and water [kg/m³]

w = water content [%]

w_u = unfrozen water content [%]

The values of 0.17, 1.0, and 0.5 in the equations above correspond to the specific heat of soil minerals, water, and ice, respectively. For organic soils, the value of 0.17 should be replaced with a value of 0.40 to represent the organic soil specific heat. (Andersland & Landanyi, 2004)

Heat capacity values for the peat, native soil, and granular fill materials in both unfrozen and frozen states were calculated using Equations 6-13 and 6-14.

6.2.8.5 Thermal Conductivity

Thermal conductivity, k is defined as the amount of heat passing in unit time through a unit cross-sectional area under a unit temperature gradient applied in the direction of heat flow, and can be expressed in the following equation (Farouki, 1986):

6-15

$$k = \frac{q}{A(T_2 - T_1)/l}$$

Where:

k = thermal conductivity [W/m*°K]

$q =$ heat flow [W]

$A =$ cross-sectional area perpendicular to heat flow [m²]

$T_2, T_1 =$ temperatures at two ends of the element [°K]

$l =$ length of element [m]

Thermal conductivity of the native soil was estimated using Equation 6-15. Using the geothermal heat flux value of 60 mW/m² from section 6.2.4.2, and thermal gradient value of 0.0237 °C/m within the frozen native soil from section 3.2.4, the thermal conductivity for the frozen native soil was calculated to be 2.53 W/m/°K. The calculated thermal conductivity is in the vertical direction, however it was assumed that thermal conductivity in horizontal direction is also equivalent.

The unfrozen thermal conductivity for the native soil was then derived by correlating the soil parameters from the frozen native soil in Figure 2-2 a) to the unfrozen parameters in Figure 2-2 b). Similarly, thermal conductivity values for the peat were obtained from the relationships in Figure 2-4.

Initial estimates for thermal conductivity values of the granular fill were obtained from the literature values shown in Figure 2-2. These initial estimates were increased through calibration of the model to the final values displayed in Figure 6-6.

6.2.9 Pre-Construction Thermal Model Results and Discussion

6.2.9.1 Results

The pre-construction thermal model succeeded in establishing a long term stable ground thermal regime (no considerable warming or cooling of deep permafrost). The results of 3 separate runs of the pre-construction model using differing trial values of -6.4° C, -5.7°C and -4.5° C as the initial temperature for the native soil material are shown in Figure 6-10. Despite the differing initial temperatures, a long-term thermal equilibrium at a value between -5.6 °C and -6.0 °C is reached for a selected element at an elevation of 7 m which corresponds approximately to the depth of zero mean annual amplitude.

Figure 6-11 shows the maximum and minimum range of temperature profiles occurring within a 1-year period of the simulation, after the stable annual thermal equilibrium has been obtained. The temperature profile shows a well-defined “trumpet curve”, with the amplitude of annual temperatures ranging from -17.4 °C to 9.4 °C at the ground surface, and progressively diminishing with increasing depth down to the DMZAA to a temperature of approximately 5.8 °C.

6.2.9.2 Discussion

The results of the pre-construction model were generally as expected. The modelled DMZAA of 14 m is in good agreement with the previously discussed literature values between 10 and 20 m. The temperature of -5.8 °C occurring at the DMZAA also falls within the range of -5 °C to -6 °C shown in the published detailed ground temperature mapping, previously discussed and shown in Figure 3-6.

The selected freezing n-factor for the peat surface of 0.63 was higher than typically reported in literature. This higher value was required during model calibration to sufficiently cool the ground surface to maintain long term equilibrium with the warming

occurring over the thawing season. Possible unaccounted environmental factors at the site such as higher than typical winds, or less than typical snow depth are hypothesized as reasons for such a high freezing n-factor, however they were not investigated further.

Interestingly, the thermal conductivity for the native soil of 2.53 W/m/°K was very close to that of ice (ranging from 2.21 W/m/°K at 0°C to 2.63 W/m/°K at -40°C). Although there was some uncertainty in the volumetric water content of the native soil layer, any potential variance in the amount of ice present within the native soil layer would have only a marginal effect on the overall thermal conductivity, as the thermal conductivity value of the frozen native soil is so close to that of ice. This could also be a possible indication that the native soil thermal conductivity is being dominated by the high ice content therein.

As mentioned in the methodology section, the pre-construction model relied on the premise that prior to the embankment construction, a regular annual thermal ground regime would have existed. Put another way, it was assumed the year to year ground temperatures were in equilibrium with the annual climate fluctuations at the location of the embankment prior to its construction. As outlined in sections 3.2.3 and 3.2.4, the ground thermal regime is however indeed slowly changing, tied to the regional air temperatures which have increased on average by 0.8°C per decade. A more thorough modelling simulation could have used a climate function spanning several decades, complete with incremental annual air temperature increases. The model would then have to be calibrated to replicate the annual incremental increase in ground temperature, rather than seek to reach long-term stable conditions as shown in Figure 6-10. This type of thorough analysis was not undertaken for two reasons. First, long-term ground temperature data is not available in the level of detail required for such an analysis. Secondly, while important for long term predictive modelling (outside the scope of this thesis), the relatively small annual air temperature increases were considered inconsequential for the purposes of the pre-construction model, whose goal was to confirm reasonable estimates for thermal parameters of the native soil and peat materials to be used in the subsequent post-construction thermal analysis. By comparison, the

thermal properties of the embankment fill were found to have a much greater effect on the thawing of the embankment, which was the focus of this current study.

The duration required to reach equilibrium was approximately 14 years for the selected initial temperatures, as shown in Figure 6-10. The duration required to reach a thermal equilibrium in the model was dependent on the proximity of the initial selected temperatures to the equilibrium value. The long duration to reach thermal equilibrium is also influenced by the insulating surficial peat layer.

6.2.10 Post-Construction Thermal Modelling Results and Discussion

6.2.10.1 Results

Modelled temperature vs. time plots for the post-construction model were previously introduced in section 5.1.2 alongside the temperature monitoring results and shown in Figure 5-1 a), b), and c); for locations along the embankment toe, mid-slope, and crest respectively. There is generally good agreement between the modelled and measured results, typically within 1 °C, with exceptions to this highlighted in the discussion section.

Thermal contour plots from the post-construction thermal model are shown in Appendix C, also previously introduced in the temperature monitoring section. The figures show the modeled thermal contours over the 10 selected timesteps in Figures C-01 to C-10[18]. As previously noted, the thermal modelling contour results were in generally good agreement with the measured results, again typically within 1 °C of the measured readings. Discrepancies between modelled and measured results greater than 1 °C were observed at specific temperature nodes along the exterior of the embankment and are discussed in the following section.

[18] The first page of Appendix C provides a reference for interpreting the information shown on the figures.

6.2.10.2 Discussion

The model was generally successful in reproducing ground temperatures similar to those measured within the embankment and foundation soils over the thawing season, as can be seen in Figure 5-1 as well as the thermal model temperature contour outputs in Appendix C. Differences between the measured and modelled results are highlighted and discussed in this section, as well as discussion on some of the important thermal properties obtained through calibration of the model.

The modelled temperatures at the embankment toe (Figure 5-1 a)), show good agreement in the 2 deeper thermistor nodes TS-C4-B and TS-C4-D, typically falling within 1 °C of the measured temperatures. In the shallower thermistor node TS-C4-A however, the modelled temperatures are cooler than the measured temperatures. This is especially apparent in the warmest period from early July to mid-August, when the thermistor node measurements read above 0 ° C and temporarily as high as 4 °C, while the modelled temperatures remain slightly below 0 ° C over that period. This can also be observed in Figures C-05 to C-07 as the modelled thaw penetrates very close to thermistor node TS-C4-A, but never penetrating below it until mid-August (Figure C-08).

The inability of the modelled temperatures to cross above the 0 °C threshold at that location is due to the amount of latent heat required to melt the frozen peat and native soils, related to their high water content. A distinct material layer representing the native soil within the active layer could be considered to improve the model accuracy, as the water content within the native soil active layer may be lower than that of the underlying permafrost.

Recurring discrepancies between modelled and measured results greater than 1 °C were observed at temperature-sensing nodes TS-C1-A, SAA-CH-A, and TS-C2-A located near the surface of the embankment slope. The discrepancies were the largest in TS-C2-A, located near the base of the slope and discussed here. In the 4 selected timesteps displayed from Figures C-04 to C-07, the modelled temperatures relative to the measured temperatures alternated from being warmer, to cooler, to warmer, to cooler again. These discrepancies can be attributed to the use of a smoothed air temperature function in the

thermal model as shown in Figure 6-4. The discrepancies noted in Figures C-04- to C-07 coincide with air temperature fluctuations above and below the smoothed air temperature function used in the model. Deeper within the embankment and foundation soils, the effect of these air temperature fluctuations is not noticeable.

Another notable discrepancy in the model was observed in thermistor node TS-C2-B, which is located adjacent the aforementioned TS-C2-A, but nearer to the embankment centre. In Figures C-06 to C-08 which represent the peak thawing season, modelled temperature contours at TS-C2-B exceeded the measured temperatures by of 2 to 4 °C. Such extreme overprediction of temperatures was not observed in the adjacent temperature-sensing nodes. A likely reason for these high localized temperatures in the model was the presence of the peat layer which lying directly beneath the TS-C2-B node. The modelled peat acted as an insulator preventing the dissipation of excess heat into the underlying relatively cool foundation soils. The thermal model did not however account for the consolidation that would inevitably occur within the peat layer as it thawed under the weight of the embankment, and the associated increase in thermal conductivity.

As expected, thermal properties of the embankment fill had the greatest impact on the modelled temperatures and depth of thaw penetration within the embankment. The calibrated thermal conductivity values for the frozen and unfrozen granular fill of 2.31 and 2.80 W/m/°K were higher than the typical literature reported values. Possible reasons include: 1) Mineral content (notably quartz) can have a significant effect on the thermal conductivity of soils. Although no mineralogical analysis of the granular fill was conducted, it is possible there was a higher than typical quartz content. 2) The presence of fines within the granular fill improved the intergranular contacts thus increasing thermal conductivity.

Calibration of the model also resulted in the unusual result of a higher thermal conductivity value for granular fill in an unfrozen state compared to the frozen state. This could be due in part to the densification of the granular fill transitioning from a frozen state to a thawed state. The densification that occurs upon thawing increases the overall thermal conductivity as water and air are replaced by soil particles, possessing higher

constituent thermal conductivities (Dumais & Konrad, 2015). Future thermal modelling studies on the test embankment should consider the densification and associated changes in thermal properties that would have occurred over the first thawing season.

Generally, the calibrated model parameters are considered justifiable and within the range of published literature values. (Farouki, 1986), (Andersland & Landanyi, 2004), (Tsytovich, 1975), (Klene, et al., 2001).

While the current model simulated only the first thawing season following construction, future modelling of long-term embankment performance should incorporate climate projection models.

6.2.11 Sensitivity Analysis

6.2.11.1 Results

A sensitivity analysis was conducted to demonstrate the importance of selected parameters on the thermal model results. The sensitivity analysis was conducted by independently varying the thermal conductivity and heat capacity values for the granular fill by +- 50%, while maintaining all other parameters constant.

Figure 6-12 shows the sensitivity analysis results for temperatures of two selected nodes (SAA-CH-A, and TS-C2-C) at the mid-slope location. The original model results are labelled as “baseline” and are shown for reference. The 50% increase and decrease of the parameter values are indicated by the symbol k, for thermal conductivity; and c, for heat capacity.

6.2.11.2 Discussion

From the figure, it can be seen that modelled temperatures increased corresponding to increases in thermal conductivity and decreases in heat capacity. Conversely, modelled temperatures decreased with decreases in thermal conductivity and increases in heat capacity. It should be noted that the trends observed over the thawing season study period would be expected to act in the opposite direction over the cooling season. For example,

an increase in thermal conductivity would be expected to result in decreased temperatures over the cooling season.

The results also showed for a constant increase or decrease of the parameter values by a given value of 50%, the model was more sensitive to changes in thermal conductivity compared to heat capacity. This is consistent with sensitivity analyses conducted by (Pavon, 2018) for the test site, which were conducted not only over the thawing season, but over a longer approximately 1.5 year timeframe.

Adjusted maximum and minimum peak thaw penetration profiles over the study period corresponding to the (k +50% and k -50 % scenarios) were also obtained from the thermal model sensitivity analyses and used to define the geometry used in the deformation modelling sensitivity analyses, discussed in that section.

6.3 Deformation Modelling

6.3.1 Methodology

Similar to the thermal modelling, the goal of the deformation modelling was to simulate measured observations from the test embankment over the course of the thawing season. The deformation modelling was conducted by finite element method numerical modelling software Sigma/W published by Geo-Slope International Ltd. The software calculates stress conditions, and corresponding deformations using constitutive models selected by the user. The software is configured to accept inputs for soil parameters, model boundary conditions, and geometry.

It is important to note the deformation modelling does not include a review of elastic or viscoplastic deformation associated with the frozen soils, and focuses only on the deformation associated with thaw consolidation. The deformation modelling was conducted sequentially, using the thermal model contour results to define the geometry of the unfrozen and frozen zones in the embankment. A similar sequential modelling approach was undertaken to define frozen and unfrozen regions and associated mechanical properties in a study of seasonal deformations under a road embankment on degrading permafrost (Kurz, et al., 2018).

The deformation properties were calibrated using the recorded field deformation measurements from the SAAs.

6.3.2 Theory

A linear elastic model was used to calculate stress-deformation within the thawed embankment soils. The Sigma/W software calculates the stresses at each soil element using the model geometry and soil unit weight. For the two-dimensional plane-strain analysis, the stresses and strains are related by the following equation (Geo-Slope International Ltd., 2010):

6-16

$$\begin{Bmatrix} \sigma_x \\ \sigma_y \\ \sigma_z \\ \tau_{xy} \end{Bmatrix} = \frac{E}{(1+v)(1-2v)} \begin{bmatrix} 1-v & v & 0 \\ v & 1-v & 0 \\ v & v & 0 \\ 0 & 0 & \frac{1-2v}{2} \end{bmatrix} \begin{Bmatrix} \varepsilon_x \\ \varepsilon_y \\ \gamma_{xy} \end{Bmatrix}$$

Where:

$\sigma =$ normal stress (in the x, y, and z directions)

$\tau_{xy} =$ shear stress in the x/y plane

$E =$ Elastic Modulus

$v =$ Poisson's Ratio

$\varepsilon =$ normal strain (in the x, and y directions)

$\gamma_{xy} =$ shear strain in the x/y plane

6.3.3 Geometry

The starting geometry used in the deformation model is similar to that used in the post-construction thermal model, however the horizontal extents of the deformation model were reduced (extending only 26 m from the embankment centreline), since the geometry

further away from the embankment does not affect deformation model results. Secondly, the bottom of the model is shaped to match the contour of the unfrozen/frozen soil boundary at selected timesteps throughout the study period, as defined by the location of the zero-degree isotherm from the results of the post-construction thermal model. Two geometries of interest presented in this thesis are the thawed region on 2015/07/04, corresponding to an early stage of embankment thawing; and a second geometry from 2015/09/05, corresponding to the maximum extent of thaw penetration observed within the embankment over the study period.

As previously mentioned, the cross-sections XS-C was selected to match the alignment of the horizontal vertical SAAs which were installed in the un-reinforced "control" section. This would ensure the SAA data corresponds as close as possible to the actual embankment geometry at the SAA location.

The finite element meshing pattern consists of a mixed quadrilateral and triangle unstructured mesh with nominal element size 0.125 m. The number of elements is 2233 for the geometry on 2015/07/04, and 2874 for the geometry on 2015/09/05. The meshing pattern is shown in the model geometry Figure 6-6.

6.3.4 Boundary Conditions

Zero-displacement boundary conditions were used in the deformation model, restraining movement of the elements at the extents of the model. This included fixed x/y-displacement boundary conditions at the base of the thawed soil region, to restrict horizontal and vertical movement. Fixed x-displacement boundary conditions were applied at the left and right extents of the model to restrict horizontal movement. The boundary conditions are shown in Figure 6-6.

6.3.5 Material Types

The thawed regions described in the geometry section overlapped the known stratigraphy of embankment granular fill, peat layer at the ground surface and underlying the granular fill, and layer of native soil below the peat. For simplicity in the deformation model, the entire thawed region was however treated as granular fill material type.

The frozen soil was not assigned deformation properties, and therefore no deformation occurred within the frozen soil.

6.3.6 Material Properties

The deformation parameters for the granular fill material are summarized in the table within Figure 6-6. Deformation parameters were obtained through calibration of the parameters to fit the field-measured deformation results.

Initial estimates for the material property values were obtained from literature, then calibrated to best match the measured deformations. A very low elastic modulus value of 110 kPa was ultimately selected for the granular fill material, which is reviewed in the discussion section.

6.3.7 Deformation Modelling Results

Results of the deformation model are presented in Figure 6-13, comparing the measured vs. modelled results at the locations of a) SAA-CH, and b) SAA-CV. The results are presented for the 2 selected timesteps; the first corresponding to an early stage thawing on 2015/07/04, and the second corresponding to the date of maximum thaw penetration on 2015/09/05. The deformed finite element mesh, (without vertical or horizontal exaggeration) is shown in Figure 6-8 a), corresponding to the date of maximum thaw penetration on 2015/09/05. Figure 6-8 b) shows the displacement vectors with direction of node movement. Note the nominal element dimensions has been doubled in Figure 6-8 b) for sake of clarity. The displacement vectors show the embankment spreading laterally away from the centreline as well as vertically.

In Figure 6-13 a), for both displayed timesteps, the model slightly overestimates the vertical deformation in the region nearest the embankment centre (within a horizontal distance of approximately 10 m from the centreline). Near the exterior of the embankment, the opposite occurs with an underestimation of vertical settlement (between a horizontal distance of 10 to 11.5 m from the centreline). For the modelled lateral deformation results shown in Figure 6-13 b), the model underestimates lateral deformation over the entire vertical range at both timesteps.

6.3.8 Deformation Modelling Discussion

As earlier described, the overall soil structure of the embankment fill following compaction would be expected to consist of a skeleton formed by ice-rich lumps of soil, separated by air voids, as well as unbonded and poorly ice-bonded soil particles. As outlined earlier in section 2.7, most thaw consolidation models are ill-suited to simulate the significant volume change associated with thawing of ice-rich frozen soils and are not intended for modeling of unsaturated soils. A simple linear elastic constitutive model was chosen to calculate stress-deformation within the thawed embankment soils. The effectiveness of the model, and considerations for future deformation modelling are discussed.

Calibration of the deformation model to match the measured vertical and horizontal deformation proved challenging, with the discrepancies between measured and modelled results visible in Figure 6-13. The linear-elastic model parameters of elastic modulus and Poisson's Ratio could not be calibrated to simultaneously match the deformations occurring 1) vertically near the embankment centre, 2) vertically near the perimeter of the embankment, 3) and laterally.

As mentioned, a very low elastic modulus value of 110 kPa was selected for the granular fill[19]. This value, obtained through calibration of the model is approximately 2 orders of magnitude lower than elastic modulus values reported in literature for loose sand (Budhu, 2007, p. 605). The reason for such a difference is that this calibrated value is used to represent the compression occurring in the ice-rich fill from a frozen state to a thawed state (trajectory b-c-d in Figure 2-9), while the literature reported values are intended to represent the compression of sand in a pre-existing thawed state (trajectory c-d only).

A Poisson's ratio value within the higher range of typical values for sand of 0.35 was selected for the fill (Budhu, 2007, p. 605). This selected value was obtained through

[19] For reference, this falls well below the elastic modulus of most soft soils, and among everyday items is comparable to the elastic modulus of gummy bears at 70 kPa (Williams, et al., 2005).

calibration, but would require further increase to approach the lateral displacement targets.

The simplification to exclude deformation of the frozen zone as a component of the model proved to be successful, as measured deformations within the frozen zone were almost negligible, compared to the significant deformations within the thawed region. Discrepancies between measured and modelled results in situations where the model showed zero displacement can be attributed to inaccuracies in defining the thawed/frozen interface within the thermal model.

Given the decision to model the thaw deformation through a linear-elastic model, the simplification to consider all the thawed soil as single material type was considered reasonable. Although separate material regions and parameters could have been assigned for the peat and native soil layers, the overall model would have increased in complexity with little confidence in the calibrated parameters[20].

In summary, the linear-elastic model was considered only marginally successful its ability to accurately model vertical and lateral deformations within the embankment. The model fails to represent the unique thaw-settlement curve for ice-rich frozen soils as shown in Figure 2-9. More advanced constitutive models available within the GeoStudio software package available to the author were similarly unable to replicate this mechanism of thaw settlement. Deformation modelling software capable of modelling the mechanisms of thaw consolidation encountered at the test site would require the ability to:

1. Define initial frozen soil structure conditions including ice-content and dry unit weight or void ratio. (i.e. establish point b on Figure 2-9, assuming deformation a-b is neglected)

[20] This is because of limited number of SAA nodes within the embankment, making it difficult to isolate and attribute measured deformations to the peat or native soil layers alone.

2. Compute immediate settlement related to ice phase change and collapse of frozen soil skeleton, involving thermo-mechanical coupling for temperature-dependent mechanical properties. (i.e. deformation b-c on Figure 2-9)
3. Compute time-dependent settlement of thawed soil (deformation c-d on Figure 2-9), involving porewater pressure dissipation (coupled with temperature). In certain scenarios, this could be simplified as immediate elastic settlement.

While alternative thaw consolidation models have been developed (Yao, et al., 2012) and successfully applied as in the modeling permafrost degradation beneath the Qinghai-Tibet highway (Qi, et al., 2012), these models simulate saturated soils, and therefore do not consider the collapse of the frozen soil skeleton and expulsion of air voids (as in item 2 above). These models can therefore not be applied to the current study problem. Further research into modeling the mechanism of collapse of the frozen soil skeleton is required.

The research presented only focuses on the component of deformation associated with thaw consolidation and does not include a review of elastic or viscoplastic deformation associated with the frozen soils. In future long-term performance studies of the test embankment, a new relatively stable active layer will become established along the exterior of the embankment. As the new active layer is established, thaw consolidation over successive years will decrease. At that time, viscoplastic creep movement of the frozen core and foundation soils may then represent a more significant proportion of overall embankment deformations, warranting further research. In research by others on degrading permafrost beneath a road embankment, the recommendation for coupled seepage, temperature, and load-deformation including viscoplasticity was identified as a suggested modelling approach (Kurz, et al., 2018).

6.3.9 Sensitivity Analysis

A sensitivity analysis was conducted to demonstrate the importance of certain parameters in the deformation model. This included modifying of the elastic modulus, and thermal conductivity of the granular fill material. Although the thermal conductivity is not a direct parameter input for the deformation model, it does impact the deformation model

results since it affects the thermal analysis temperature contour results, which are subsequently used to define the deformation model geometry.

Figure 6-14 shows the sensitivity analysis results for deformation model, through modification of the parameters discussed above. The figure shows modelled deformations on 2015/09/05, corresponding to the time of maximum thaw penetration in the embankment calculated at the locations of SAA-CH in portion a), and SAA-CV in portion b). Similar to the sensitivity analysis for the thermal model, the original model results are labelled as "baseline" and are shown for reference. The 50% increase and decrease of the parameter values are indicated by the symbol k, for thermal conductivity; and E, for elastic modulus.

The results show that the thermal conductivity has a significant effect on the modelled deformations, by affecting the thawed region geometry in the deformation model. More generally, this also highlights the importance of having an accurate thermal model when coupling sequentially with a deformation model.

The deformation model was also highly sensitive to the elastic modulus, as evidenced in the results figure. While beyond the scope of the current sensitivity analysis, it can be appreciated the elastic modulus is itself a function of the dry density of the fill material.

Because the elastic modulus represents one of only 2 soil property variables in the linear-elastic model (alongside Poisson's ratio), and has such an impact on the model results, the next logical extension of this deformation model would be to define the elastic modulus as a function of other parameters (most notably dry density). In numerical analyses by (Botz & Haas, 1980, p. 74), a dry density parameter was incorporated into the elastic modulus of frozen fill. It was found that the dry density parameter had the greatest effect on simulated settlement.

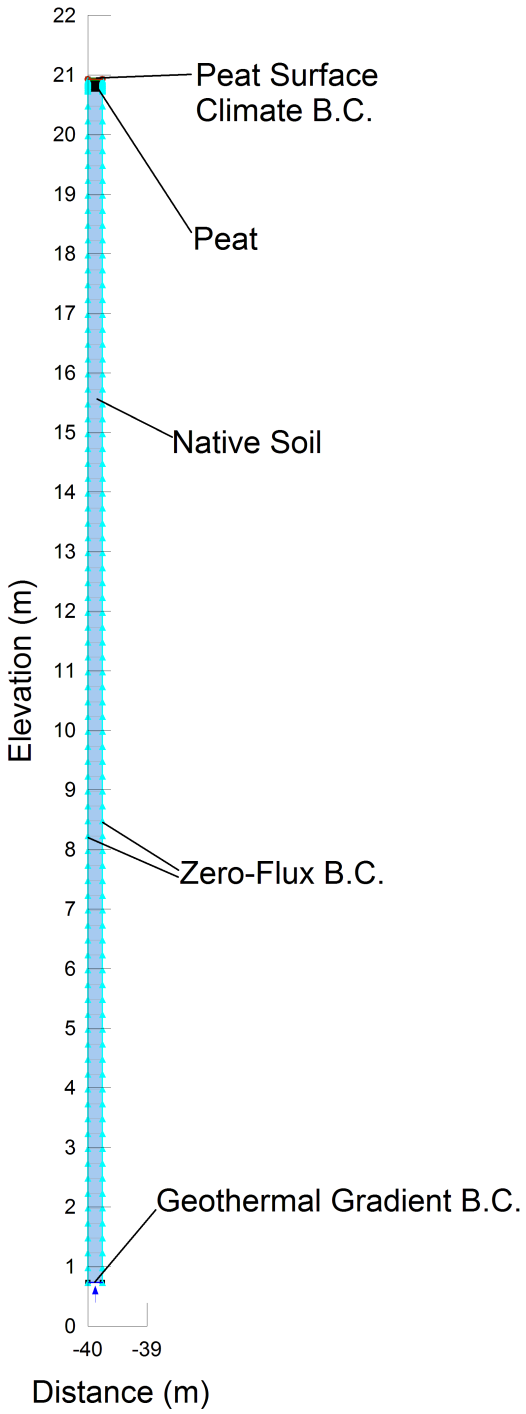

Figure 6-1: Pre-construction Thermal Model Geometry
(Material Types, Boundary Conditions (B.C.), and Element Meshing are shown)

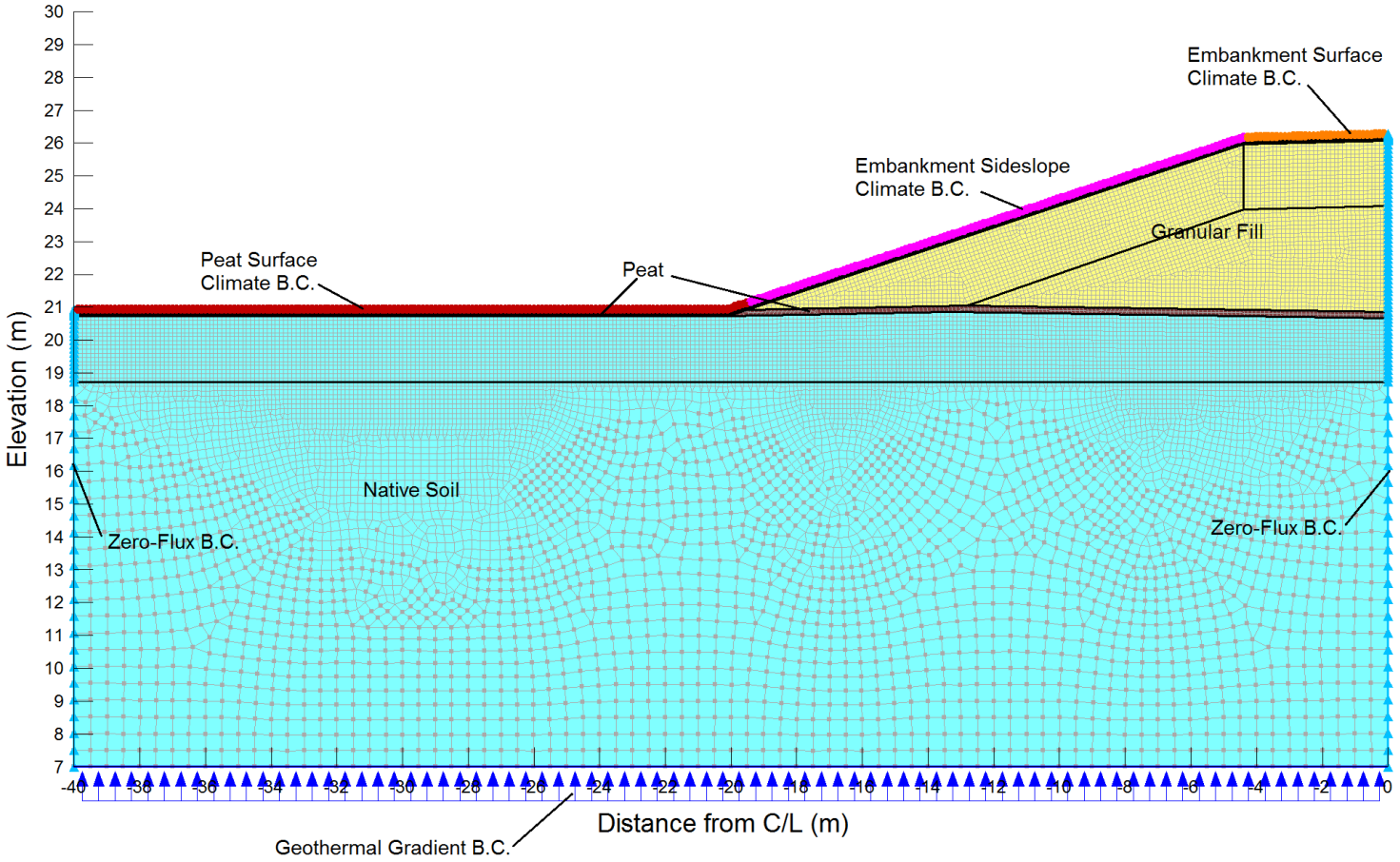

Figure 6-2: Post-construction Thermal Model Geometry
(Material Types, Boundary Conditions (B.C.), and Element Meshing are shown)

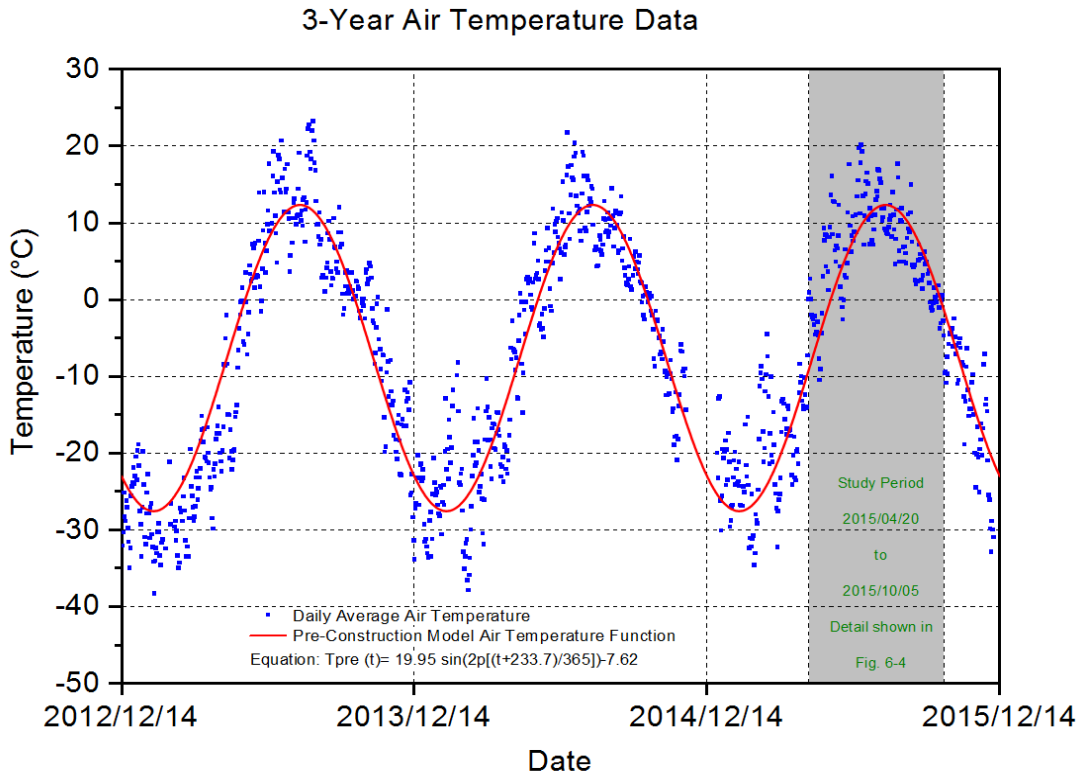

Figure 6-3: 3-Year Air Temperature Data

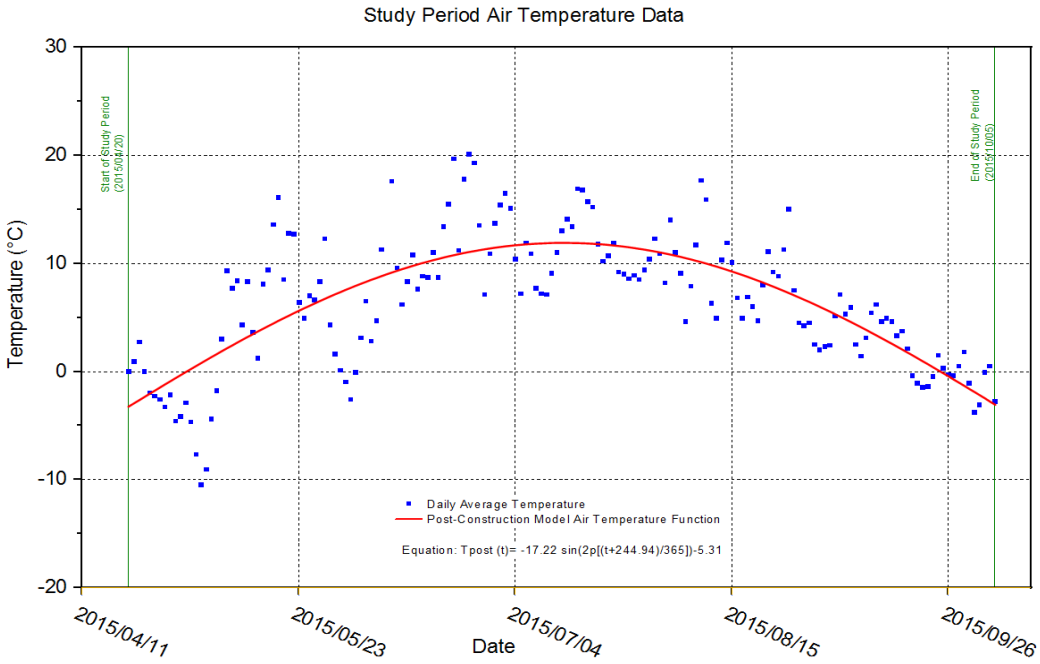

Figure 6-4: Study Period Air Temperature Data

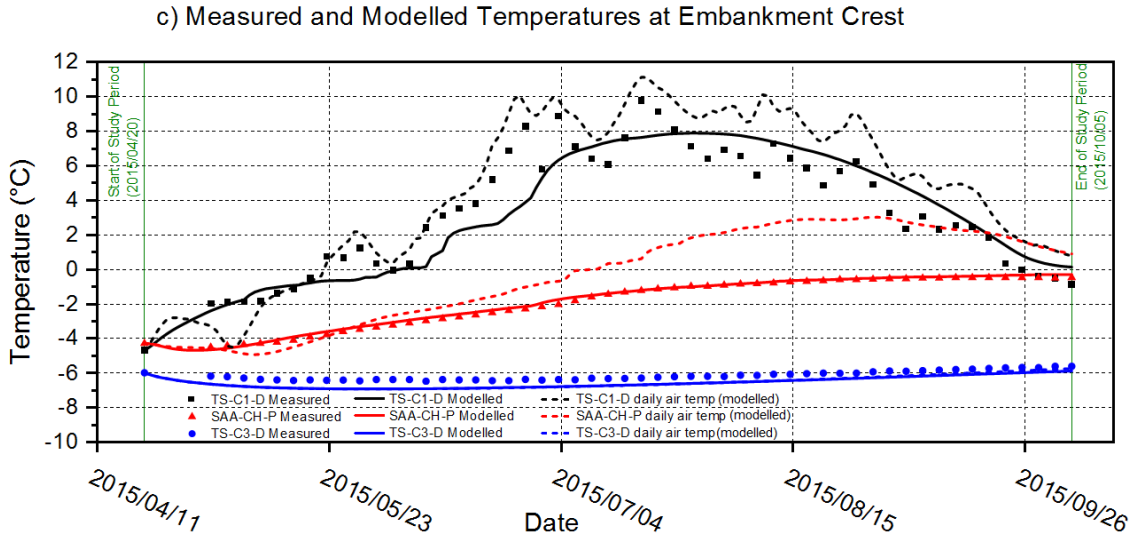

Figure 6-5: Modelled embankment temperatures at crest, with alternative daily climate function model results

Daily climate function (in dotted lines), versus sinusoidal climate function (smoothed line), .

Thermal Model Material Properties

Material Type	Water Content		Heat Capacity (MJ/m³/°K)		Thermal Conductivity (W/m/°K)		Dry Unit Weight (kN/m³)	Dry Density (kg/m³)	Specific Gravity	Saturation (%)	Void Ratio
	Gravimetric (%)	Volumetric	Unfrozen	Frozen	Unfrozen	Frozen					
Peat	200.0 %	0.40	2.01	1.20	0.25	0.45	1.96	200	1.40	46.7	6.00
Native Soil	28.8 %	0.40	2.69	1.84	1.50	2.53	13.73	1400	2.67	85.0	0.91
Granular Fill	13.7 %	0.20	1.91	1.49	2.80	2.31	14.59	1488	2.67	46.1	0.79

Thermal Model Freezing and Thawing n-factors

Location	Surface Material	Freezing n-factor	Thawing n-factor
Embankment Toe	Peat	0.63	0.76
Embankment Slope	Granular Fill	0.95	1.00
Embankment Crest	Granular Fill	0.80	1.30

Deformation Model Material Properties

Material Type	Elastic Modulus (kPa)	Poisson's Ratio
Granular Fill	95	0.35

Figure 6-6: Modelling Parameters

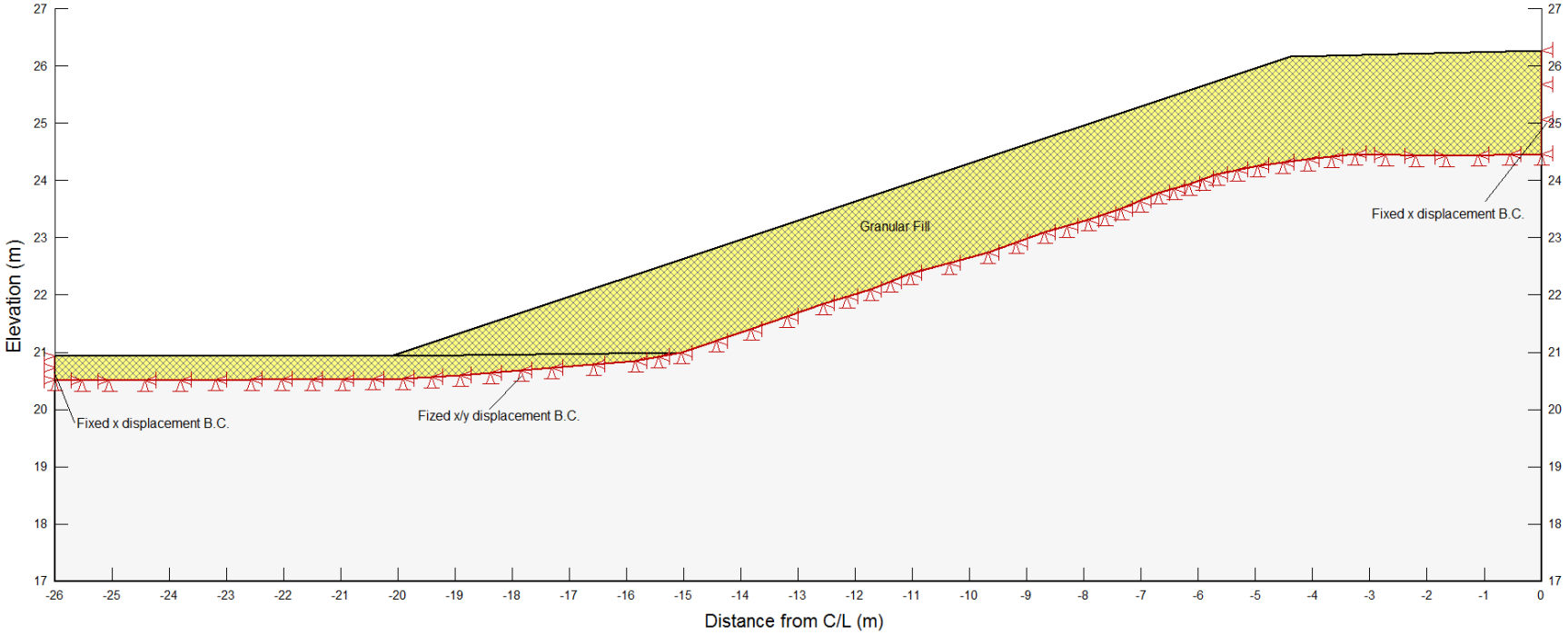

Figure 6-7: Deformation Model Geometry
(Material Type, Boundary Conditions (B.C.), and Element Meshing are shown) . Geometry shown corresponds to 2015/09/05

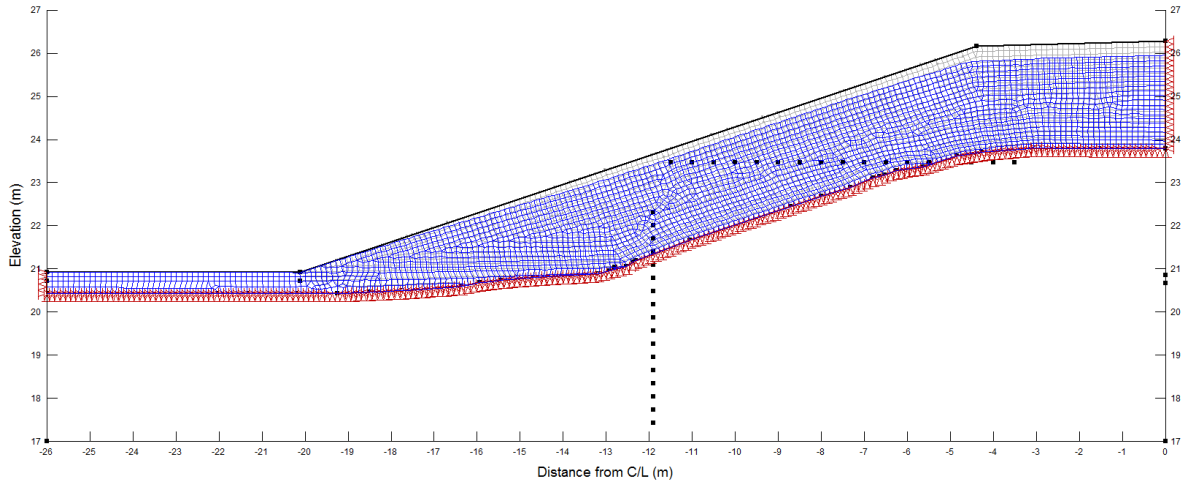

a)

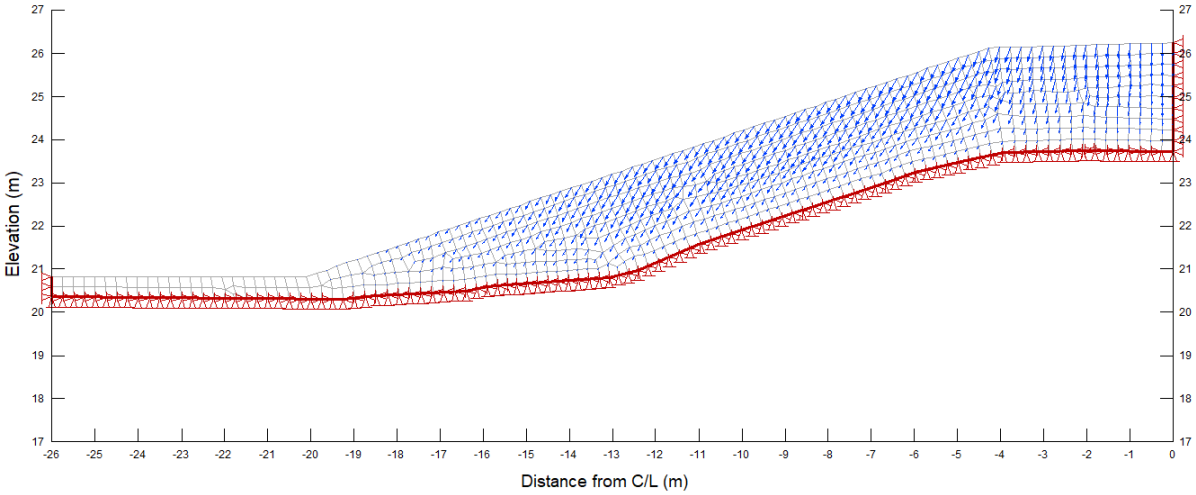

b)

Figure 6-8: Deformation Model with deformed finite element mesh and displacement vectors
Geometry shown corresponds to 2015/09/05

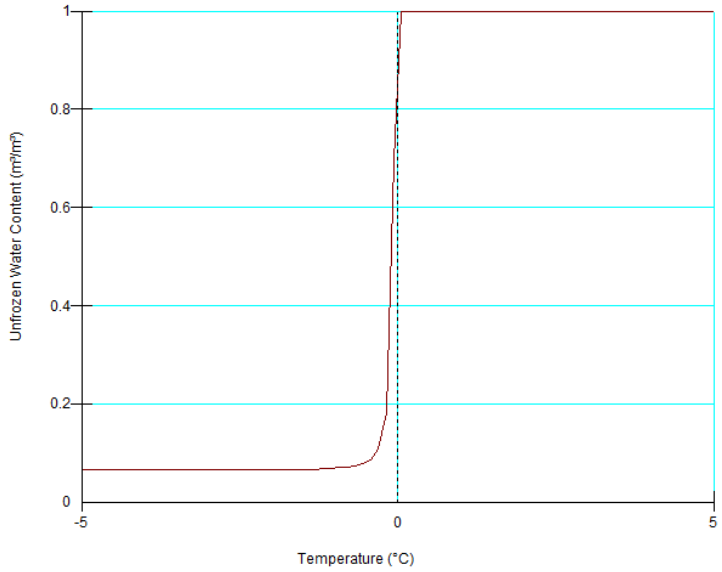

Figure 6-9: Unfrozen Water Content Function for Peat.
Function shown applied in Temp/W thermal model software. Unfrozen water content function values obtained from (Nagare, et al., 2012).

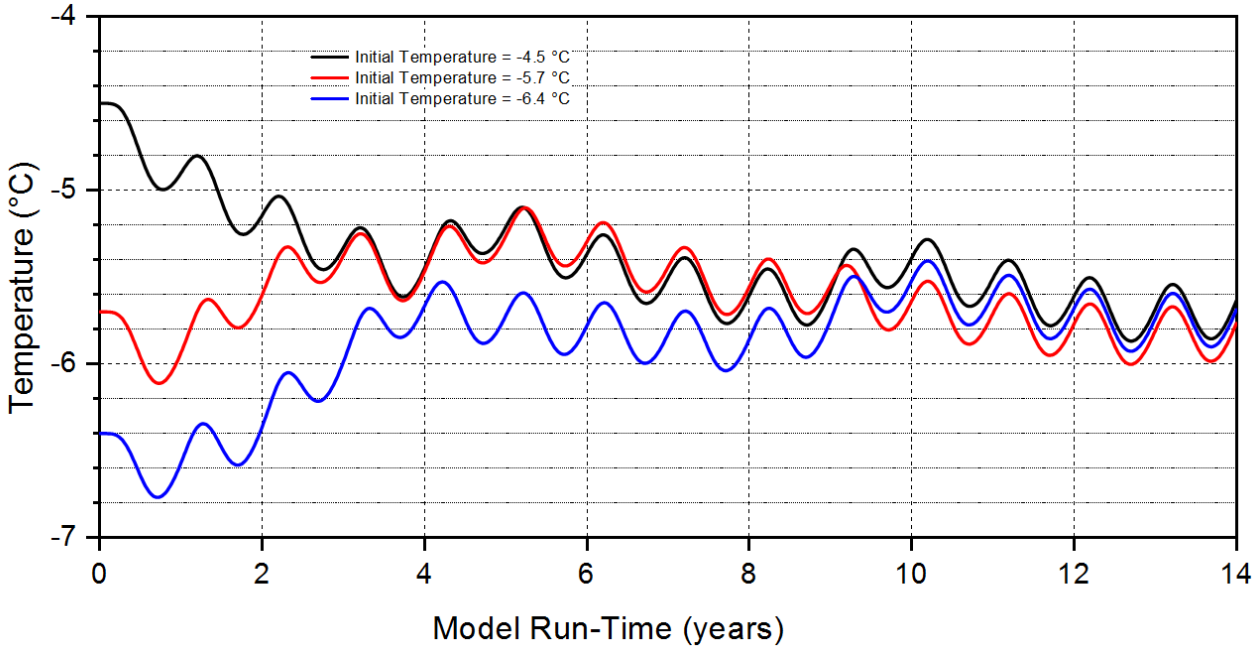

Figure 6-10: Stabilization of Initial Temperatures in Pre-Construction Thermal Model

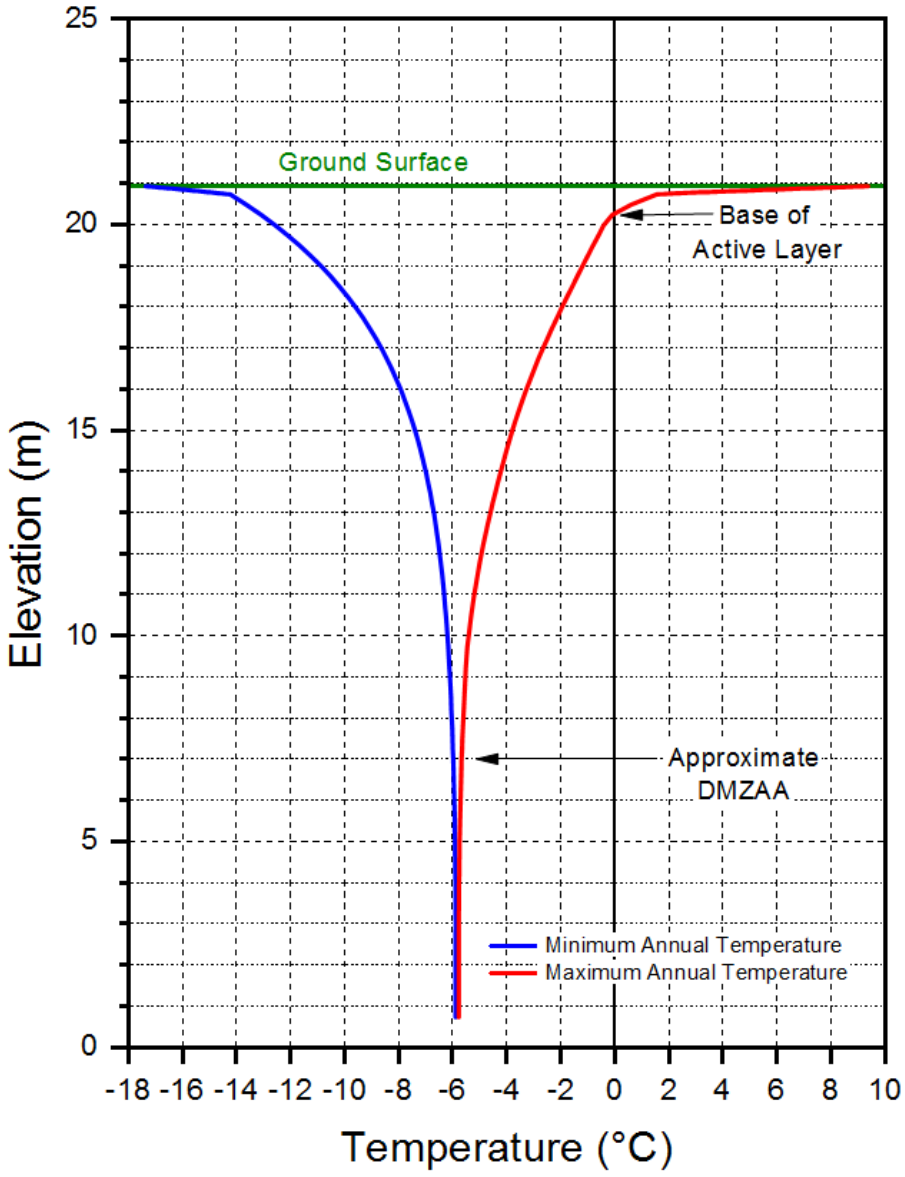

Figure 6-11: Pre-Construction Model Ground Temperature Profile

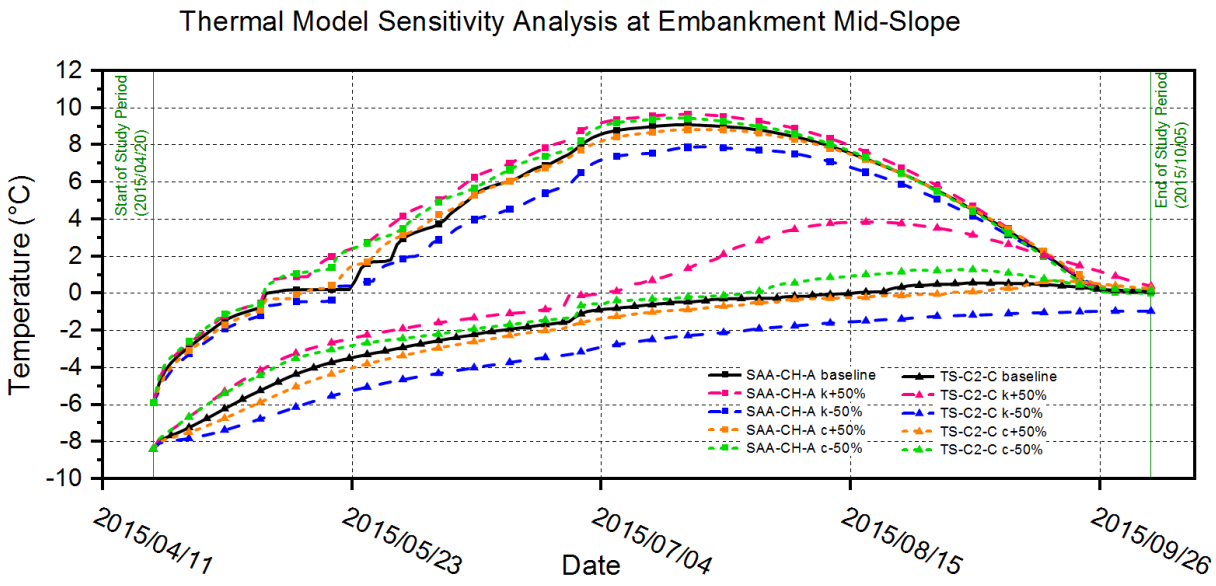

Figure 6-12: Thermal Model Sensitivity Analysis Results
Results shown for selected nodes at embankment mid-slope. Modified parameters are thermal conductivity, k, and heat capacity, c.

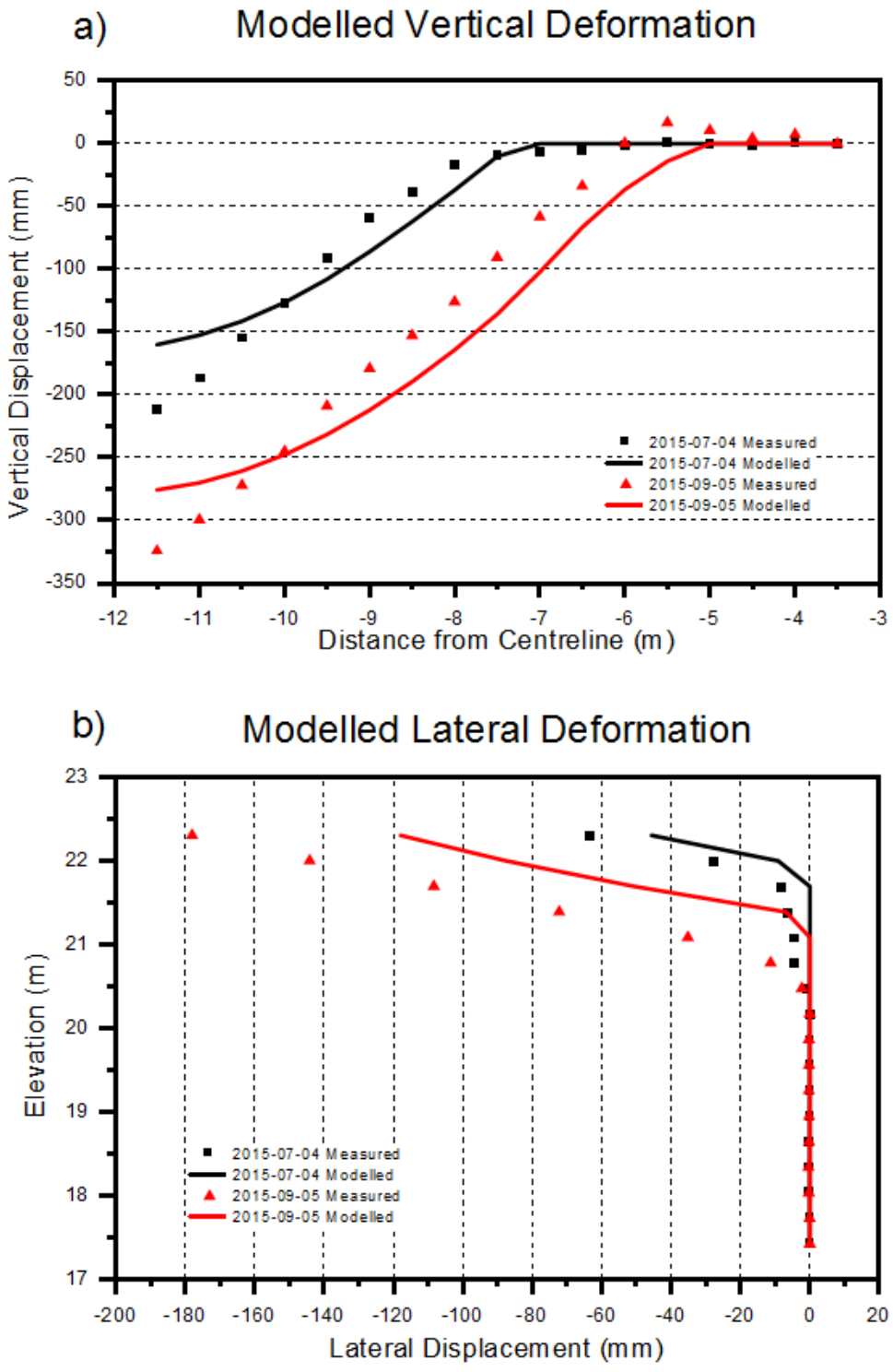

Figure 6-13: Deformation Model Results
at locations of a) SAA-CH, and b) SAA-CV; at selected times corresponding to early stage and maximum stage of thaw penetration

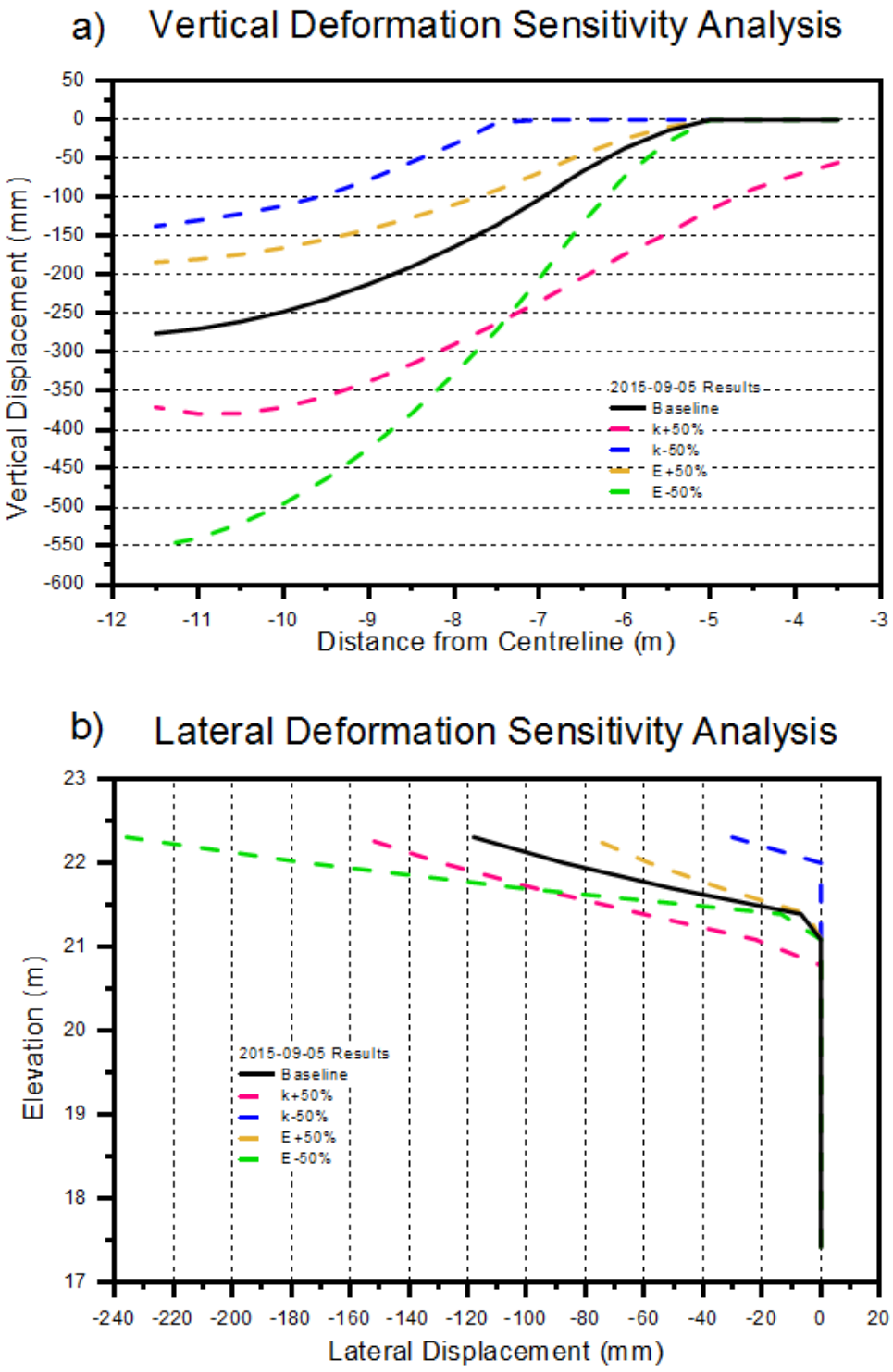

Figure 6-14: Deformation Model Sensitivity Analysis Results
at locations of a) SAA-CH, and b) SAA-CV. Modified parameters are thermal conductivity, k, and elastic modulus, E.

7 Summary, Conclusions, and Future Research Recommendations

7.1 Summary

The primary goal of this study was to improve on the understanding of the processes related to the performance of embankments constructed using compacted frozen fill, in regions of continuous permafrost.

The research conducted consisted of establishment of a test site on the Inuvik-Tuktoyaktuk Highway in the Northwest Territories. This thesis focuses on an area of the test site which comprises a 20 m long section of highway embankment, approximately 6 m high. Instrumentation installed at the test embankment included thermistors, SAAs, and piezometers. Temperatures and deformations were recorded and analysed over the first thawing season following the embankment construction.

An estimate for the dry unit weight of the embankment fill compacted in a frozen state was made, using observations made during construction, along with review of laboratory testing results for samples collected from the test site, and laboratory test results on frozen soil published in literature. A background review of the project setting including physiography and geology, climate, and ground temperature data was also conducted.

Thermal and deformation modelling of the embankment over the first thawing season following construction was conducted. The models were calibrated using the field measurements, and sensitivity analyses were run to identify the relative importance of selected parameters in the thermal and deformation models. Discussion of the thermal and deformation modelling processes and results identify important factors affecting the performance of the embankment during and shortly after construction.

7.2 Conclusions

From the research conducted, the following conclusions are provided:

1) The dry unit weight of the embankment fill compacted in a frozen state was estimated at 14.59 kN/m³. This was based on literature review of the compaction

of frozen soils, laboratory testing of embankment fill from the test site, and observations made during construction of the embankment.

2) Temperature monitoring showed warming along the exterior surface of the embankment, with the progression of the thawing front advancing deeper into the embankment throughout the thawing season. The embankment core and foundation soils remained frozen throughout the entire thawing season, as expected. The measured temperature results throughout the embankment were generally well replicated in the thermal models using reasonable thermal parameters. Sensitivity analysis of the thermal model parameters showed that thermal conductivity was most sensitive parameter.
3) Deformation monitoring showed deformations constrained to the thawed exterior portions of the embankment, with very little movement occurring within the frozen zones of the embankment. Settlement originated at the outside of the embankment at the early stages of the thawing season, and advanced towards the centre of the embankment as the thawing front penetrated deeper into the embankment. Lateral spreading (away from the embankment centerline) was observed, also consistent with the longitudinal cracking observed along the embankment crest.
4) The linear-elastic model was considered only marginally successful in its ability to accurately model vertical and lateral deformations within the embankment. The embankment fill soil structure consists of a skeleton of ice-rich lumps of soil, separated by air voids, as well as unbonded and poorly ice-bonded soil particles. The presented model, along with alternative thaw-consolidation models do not capture the mechanisms of thaw-settlement for this type of frozen soil structure. Further research into modeling the mechanism of collapse of the frozen soil skeleton in unsaturated frozen soils is required. Sensitivity analyses were still able to highlight the importance of accurate thermal modeling when using to sequentially model deformation.
5) A better understanding of the magnitude of volumetric strain over the first thawing season following construction is invaluable in estimating required fill quantities in new highway construction. Compressive volumetric strain within the

thawed zone over the first thawing season was measured as 18.5%, using geometry obtained from the calibrated thermal model to establish the embankment thaw penetration, and topographic survey data to establish the ground surface settlement. The magnitude of volumetric strain is related to the frozen dry unit weight obtained during construction.

7.3 Future Research Recommendations

Based on the findings and conclusions obtained from the current research, the following areas of further research are recommended:

1) Improve characterization of soil structure. Literature reviewed by the author suggests frozen dry density is a key parameter in the thaw consolidation of embankments constructed with frozen fill. Field density tests on the embankment fill prior to and after thawing would provide a much-improved understanding on the processes of thaw consolidation of the unsaturated frozen soil. Field density testing such as use of a sand cone or rubber balloon could provide valuable field density data. Additional characterization of soil structure could include gradation of the frozen soil lumps. This information could be used to better understand the field compaction procedure and mechanisms involved during thaw consolidation of the unsaturated frozen soil. With improved characterization of the soil structure, it may be possible to apply existing theories of soil-mechanics to the study problem.
2) Expand thermal modelling. While the current model simulated only the first thawing season following construction, future modelling of long-term embankment performance should incorporate climate projection models. Considerations should also be made for the densification and associated changes in thermal properties that would have occurred over the first thawing season. Finally, impacts of advection should be considered in future studies of the highway embankment, as surface drainage can significantly affect the degradation of permafrost soils.

3) Extend deformation modelling. The current linear-elastic modelling was considered only marginally successful its ability to accurately model vertical and lateral deformations within the embankment. The existing models do not appropriately capture the mechanisms of thaw-settlement. With improved characterization of the frozen soil (specifically dry unit weight), selection of a more appropriate constitutive model for the deformation modelling would be possible. The selected deformation model should consider initial frozen dry unit weight, the immediate settlement related to ice phase change and collapse of the unsaturated frozen soil skeleton, and be capable of coupling temperature and deformation.

References

Alkire, B., Haas, W. & Kaderabek, T., 1975. Improving Low Temperature Compaction of a Granular Soil. *Canadian Geotechnical Journal,* 12(4), pp. 527-530.

Allen, D. M., Michel, F. A. & Judge, A. S., 1988. The permafrost regime in the Mackenzie Delta, Beaufort Sea region, N.W.T. and its significance to the reconstruction of the palaeoclimatic history. *Journal of Quaternary Science,* 3(1), pp. 3-13.

Amec Foster Wheeler, 2016. *Northern Transportation Infrastructure: Improving Maintenance Procedures for Highways in Permafrost Regions,* s.l.: s.n.

Andersland, O. B. & Landanyi, B., 2004. *Frozen Ground Engineering.* 2nd ed. Hoboken(New Jersey): John Wiley & Sons, Inc..

ASTM, 2007. *ASTM Standard D422-63 (2007) Standard Test Method for Particle-Size Analysis of Soils.* West Conshohocken, PA: ASTM International.

ASTM, 2007. *ASTM Standard D4718-87 Standard Practice for Correction of Unit Weight and Water Content for Soils Containing Oversize Particles.* West Conshohocken, PA: ASTM International.

ASTM, 2009. *ASTM D2488-09a Standard Practice for Description and Identification of Soils (Visual-Manual Procedure).* West Consohocken, PA: ASTM International.

ASTM, 2010. *ASTM Standard D2216-10 Standard Test Methods for Laboratory Determination of Water (Moisture) Content of Soil and Rock by Mass.* West Conshohocken, PA: ASTM International.

ASTM, 2012. *ASTM D698-12 Standard Test Methods for Laboratory Compaction Characteristics of Soil Using Standard Effort (12 400 ft-lbf/ft³ (600 kN-m/m³)).* West Conshohocken, PA: ASTM International.

ASTM, 2016. *ASTM Standard D4083-89 (2016) Standard Practice for Description of Frozen Soils (Visual-Manual Procedure).* West Conshohocken, PA: ASTM International.

BGC Engineering Inc., 2016. *Mike Zubko Airport Climate Change Vulnerability Assessment,* Vancouver, BC: BGC Engineering Inc..

Bonsal, B. R. & Kochtubajda, B., 2009. An assessment of present and future climate in the Mackenzie Delta and the near-shore Beaufort Sea region of Canada. *International Journal of Climatology,* Issue 29, pp. 1780-1795.

Botz, J. & Haas, W., 1980. *The Construction of an Embankment with Frozen Soil,* Hanover, New Hampshire: U.S. Army Cold Regions Research and Engineering Laboratory.

Budhu, M., 2007. *Soil Mechanics and Foundations.* 2nd ed. New York: John Wiley & Sons, Inc..

Burn, C., 2015. *The geocryological bibliography of J. Ross Mackay (1915-2014).* Québec, Canada, Canadian Geotechnical Society.

Burn, C. R. & Kokelj, S. V., 2009. The Environment and Permafrost of the Mackenzie Delta Area. *Permafrost and Periglacial Processes,* 20(2), pp. 83-105.

Burwash, W. & Clark, J., 1981. *Compaction of Soils in Freezing Conditions.* Fredericton, 34th Canadian Geotechnical Conference.

Caterpillar Inc., 2016. *Caterpillar Products and Services.* [Online]
Available at: http://www.cat.com/en_US/products.html
[Accessed 9 February 2017].

Cheng, G., Zhang, J., Sheng, Y. & Chen, J., 2004. Principle of thermal insulation for permafrost protection. *Cold Regions Science and Technology,* 40(1-2), pp. 71-79.

Clark, J., 1970. *Cold Weather Compaction of Soils.* Banff, Alberta, Canadian Geotechnical Society.

Darrow, M. M., 2011. Thermal modeling of roadway embankments over permafrost. *Cold Regions Science and Technology,* 65(3), pp. 474-487.

De Grandpré, I., Fortier, D. & Stephani, E., 2012. Degradation of permafrost beneath a road embankment enhanced by heat advected in groundwater. *Canadian Journal of Earth Sciences,* 49(8), pp. 953-962.

De Guzman, E. M., Alfaro, M., Doré, G. & Arenson, L. U., 2017. *Performance of instrumented sections along a highway in the Canadian arctic, 19th International Conference on Soil Mechanics and Geotechnical Engineering.* Seoul, International Society for Soil Mechanics and Geotechnical Engineering.

De Guzman, E. M. et al., 2015. *Initial Monitoring of Instrumented Test Sections along the Inuvik-Tuktoyaktuk Highway.* Québec, 68th Canadian Geotechnical Conference.

De Guzman, E. M. et al., 2018. Large-scale direct shear testing of compacted frozen soil under freezing and thawing conditions. *Cold Regions Science and Technology,* Volume 151, pp. 138-147.

Doré, G., Niu, F. & Brooks, H., 2016. Adaptation Methods for Transportation Infrastructure Built on Degrading Permafrost. *Permafrost and Periglacial Processes,* 27(4), pp. 352-364.

Dumais, S. & Konrad, J.-M., 2015. *Laying the Foundations for the Development of an Extension to the Theory of Thaw Consolidation, 16th International Conference on Cold Regions Engineering.* Salt Lake City, Utah, American Society of Civil Engineers.

Dyke, L., 2000. *The Physical Environment of the Mackenzie valley: A Baseline fo the Assessment of Environmental Change, Chapter 2.* Ottawa: Geological Survey of Canada, Bulletin 547.

Farouki, O. T., 1986. *Thermal Properties of Soils.* Clausthal-Zellerfeld, Germany: Trans Tech Publications.

Flynn, D. et al., 2016. Forecasting Ground Temperatures under a Highway Embankment on Degrading Permafrost. *Journal of Cold Regions Engineering,* 30(4).

Fortier, D., Allard, M. & Shur, Y., 2007. Observation of Rapid Drainage System Development by Thermal Erosion of Ice Wedges on Bylot Island, Canadian Arctic Archipelago. *Permafrost and Periglacial Processes,* 18(3), p. 229–243.

French, H. M., 1996. *The Periglacial Environment.* 2nd ed. Essex, England: Addison Wesley Longman Limited.

Geological Survey of Canada, 2000. *Ground Temperature Database for Northern Canada,* s.l.: Natural Resources Canada.

Geo-Slope International Ltd., 2010. *Stress-Deformation Modeling with SIGMA/W 2007,* Calgary, Alberta: Geo-Slope International Ltd..

Geo-Slope International Ltd., 2010. *Thermal Modeling with TEMP/W 2007,* Calgary, Alberta: Geo-Slope International Ltd..

Google Maps, 2018. *Google Maps.* [Online]
Available at: https://www.google.ca/maps/@68.9670765,-133.6235024,32016m/data=!3m1!1e3
[Accessed 1 March 2018].

Government of Canada National Climate Services, 2016. *Historical Climate Data.* [Online]
Available at: http://climate.weather.gc.ca/
[Accessed 6 October 2016].

Government of Northwest Territories, 2017. *Inuvik Tuktoyaktuk Mackenzie Valley Highway.* [Online]
Available at: ith.dot.gov.nt.ca
[Accessed 21 November 2017].

Gowan, R. & Dallimore, S., 1990. *Ground Ice Associated with Granular Deposits in the Tuktoyaktuk Coastlands Area, N.W.T., Proceedings of the Fifth Canadian Permafrost Conference.* Québec, Québec, Centre d'études nordiques, Université Laval.

Graham, J., Fensury, H. & Shields, D. H., 1988. The Thawed Strength of Soil Compacted While Frozen: An Introductory Study. *Geotechnical Testing Journal,* 11(2), pp. 125-131.

Haas, W. M., Alkire, B. D. & Kaderabek, T. J., 1978. *Increasing the Effectiveness of Soil Compaction at Below-Freezing Temperatures,* Hanover, New Hampshire: U.S. Army Cold Regions Research and Engineering Laboratory.

Harlan, R. & Nixon, J. F., 1978. Ground Thermal Regime. In: O. B. Andersland & D. M. Anderson, eds. *Geotechnical Engineering for Cold Regions.* New York: McGraw-Hill Book Company, pp. 103-163.

Johansen, O., 1975. *Thermal Conductivity of Soils, Ph.D. thesis ,* Trondheim, Norway: (CRREL Draft Translation 637, 1977).

Johnson, A. & Sallberg, J., 1962. *Factors Influcencing Compaction Test Results,* Washington, D.C.: National Research Council Highway Research Board, Bulletin 319.

Johnston, G., 1981. *Permafrost Engineering Design and Construction.* Toronto: John Wiley & Sons.

Karunaratne, K. & Burn, C., 2003. *Freezing n-factors in discontinuous permafrost terrain, Takhini River, Yukon Territory, Canada.* Zurich, Taylor & Francis Group, pp. 519-524.

Keune, R. & Hoekstra, P., 1967. *Calculating the Amount of Unfrozen Water in Frozen Ground from Moisture Characteristic Curves, Special Report 114,* Hanover, New Hampshire: U.S. Army Materiel Command Cold Regions Research & Engineering Laboratory.

Klene, A. E., Nelson, F. E., Shiklomanov, N. I. & Hinkel, K. M., 2001. The N-Factor in Natural Landscapes: Variability of Air and Soil-Surface Temperatures, Kuparuk River Basin, Alaska, U.S.A.. *Arctic, Antarctic, and Alpine Research,* 33(2), pp. 140-148.

Kurz, D. et al., 2018. Seasonal deformations under a road embankment on degrading permafrost in Northern Canada. *Environmental Geotechnics,* pp. 1-12.

Lachenbruch, A. H. & Marshall, B. V., 1986. Changing climate: geothermal evidence from permafrost in the Alaskan Arctic. *Science,* 234(4777), pp. 689-696.

Lingnau, B., 1985. *Observation of the Design and Performance of the Dempster Highway,* Edmonton: Master of Engineering Thesis, University of Alberta.

Lunardini, V., 1978. *Theory of N-Factor and Correlation of Data.* Edmonton, Alberta, Proceeding of the Third International Conference on Permafrost, National Research Council of Canada.

Lunardini, V., 1988. *Heat Conduction with Freezing or Thawing, Monograph 88-1,* Hanover, New Hampshire: U.S. Army Cold Regions Research and Engineering Laboratory.

Luscher, U. & Afifi, S. S., 1973. *Thaw Consolidation of Alaskan Silts and Granular Soils.* Yakutsk, Siberia, National Research Council of Canada, Proceedings of the 2nd International Conference on Permafrost.

Mackay, J. R., 1963. *The Mackenzie Delta Area, N.W.T.*. Ottawa, Canada: Department of Mines and Technical Surveys.

Mackay, J. R., 1974. Seismic Shot Holes and Ground Temperatures, Mackenzie Delta Area, Northwest Territories. *Geological Survey of Canada, Report of Activities Part A. April to October 1973,* Volume Paper 74-1 Part A, pp. 389-392.

Measurand, 2017. *Measurand SAAF Manual, User Manual.* [Online]
Available at: https://userfiles-kb.s3.amazonaws.com/userfiles/5656/7692/manual.pdf
[Accessed 11 August 2017].

Meteorological Service of Canada, Environment and Climate Change Canada, 2017. *Tuktoyaktuk A Temperature and Precipitation Graph for 1981 to 2010 Canadian Climate Normals.* [Online]
Available at:
http://climate.weather.gc.ca/climate_normals/results_1981_2010_e.html?searchType=stnProx&txtRadius=100&selCity=&selPark=&optProxType=custom&txtCentralLatDeg=69&txtCentralLatMin=1&txtCentralLatSec=5&txtCentralLongDeg=133&txtCentralLongMin=16&txtCentralLong
[Accessed 4 July 2017].

Morgenstern, N. R. & Nixon, J. F., 1971. One-dimensional Consolidation of Thawing Soils. *Canadian Geotechnical Journal,* 8(4), pp. 558-565.

Nagare, R. M., Schincariol, R. A., Quinton, W. L. & and Hayashi, M., 2012. Effects of Freezing on Soil Temperature, Freezing Front Propagation and Moisture Redistribution in Peat: Laboratory Investigations. *Hydrology and Earth System Sciences,* 16(2), pp. 501-515.

Pavon, G. J., 2018. *Evaluating the Thermal Properties of Soils Based on Measured Ground Temperatures, M.Sc. Thesis,* Winnipeg, Manitoba: University of Manitoba.

Pollack, H. R., 1993. Climate change inferred from borehole temperatures. *Global and Planetary Change,* 7(1-3), pp. 173-179.

Qi, J., Yao, X., Yu, F. & Liu, Y., 2012. Study on thaw consolidation of permafrost under roadway embankment. *Cold Regions Science and Technology,* Issue 81, pp. 48-54.

Rampton, V., 1987. *Map 1647A, scale 1:500 000, Surficial geology, Tuktoyaktuk Coastlands, Northwest Territories.* s.l.:Geological Survey of Canada.

Rampton, V., 1988. *Quaternary Geology of the Tuktoyaktuk Coastlands, Northwest Territories.* Ottawa, Canada: Geological Survey of Canada.

Schulson, E. M., 1999. The structure and mechanical behavior of ice. *JOM,* 51(2), pp. 21-27.

Serreze, M. et al., 2000. Observational Evidence of Recent Change in the Northern High-Latitude Environment. *Climatic Change,* 46(1-2), pp. 159-207.

Speer, T., Watson, G. & Rowley, R., 1973. *Effects of Ground-Ice Variability and Resulting Thaw Settlements on Buried Warm-Oil Pipelines.* Yakutsk, Siberia, National Research Council of Canada, Proceedings of the 2nd International Conference on Permafrost.

Taylor, A. E., 1995. Field measurements of n-factors for natural forest areas, Mackenzie Valley, Northwest Territories. In: *Current Research 1995-B.* s.l.:Geological Survey of Canada, pp. 89-98.

Tsytovich, N., 1975. *The Mechanics of Frozen Ground.* Washington, D.C.: Scripta Book Company.

Williams, S. H. et al., 2005. Mechanical Properties of Foods Used in Experimental Studies of Primate Masticatory Function. *American Journal of Primatology ,* 3(67), pp. 329-346.

Yao, X., Qi, J. & Wu, W., 2012. Three dimensional analysis of large strain thaw consolidation in permafrost. *Acta Geotechnica,* Volume 7, pp. 193-202.

Yorath, C. N. D. Y. F. P. B., 1980. *Map 1509A, Geology, The Beaufort-Mackenzie Basin, District of Mackenzie and Yukon Territory.* Ottawa, Ontario: The Geological Survey of Canada.

Youd, T., 1973. *Factors Controlling Maximum and Minimum Densities of Sands.* Los Angeles, California, American Society for Testing and Materials, Symposium on Evaluation of Relative Density and its Role in Geotechnical Projects Involving Cohesionless Soils.

APPENDIX A:

ITH CONSTRUCTION ATLAS

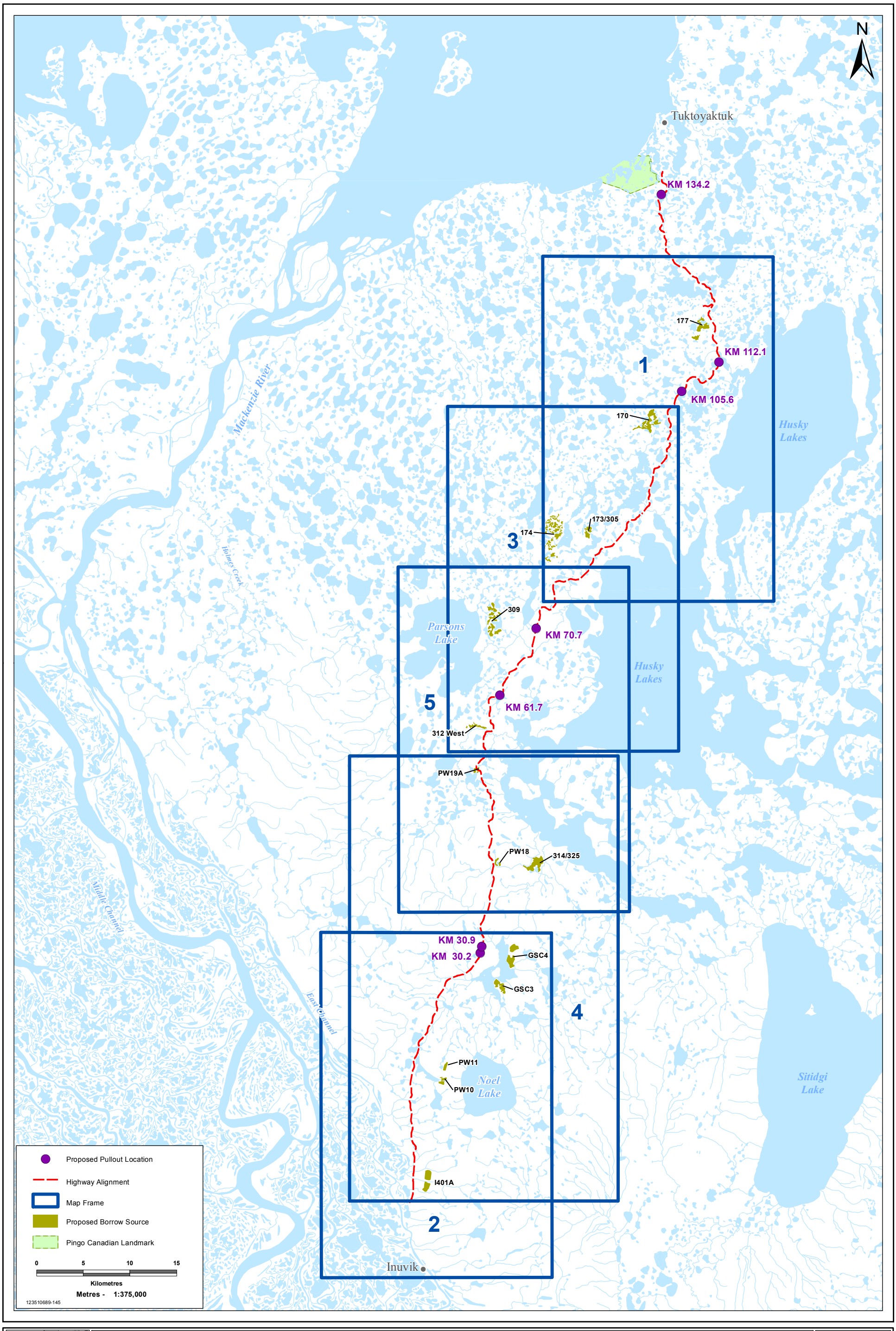

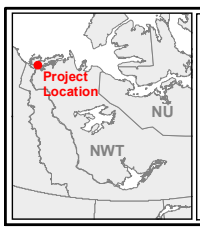

INUVIK - TUKTOYAKTUK GEOTECHNIOCAL INVESTIGATIONS PROGRAM

Construction Plan Overview Atlas
Index

Acknowledgements: Original Drawing by Jacques Whitford - AXYS Ltd.

PREPARED BY Northwest Territories Transportation

PREPARED FOR KAVIK-STANTEC

FIGURE NO. **INDEX**

Last Modified: September 13, 2013 By: jpetho

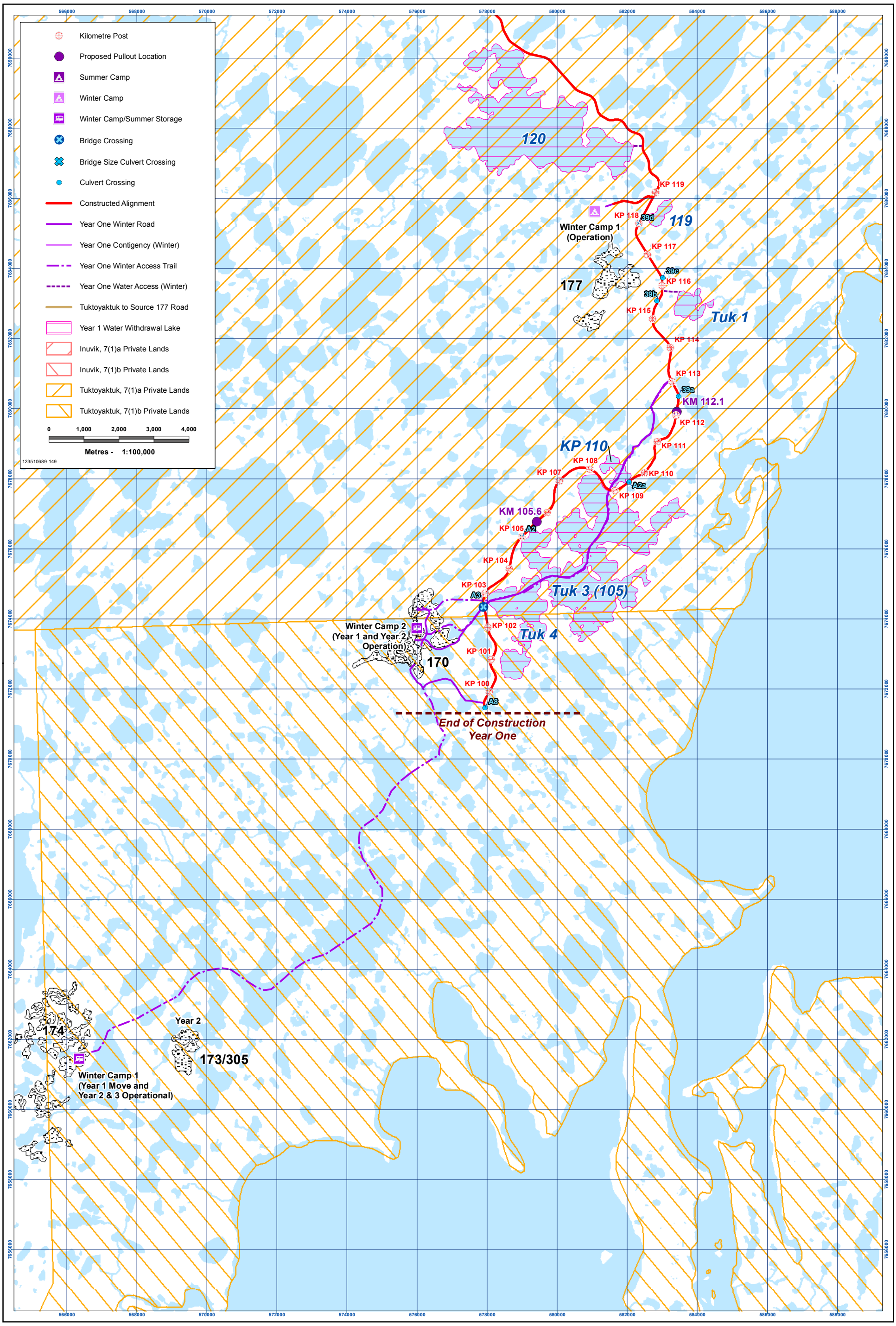

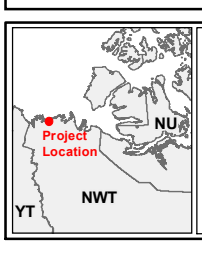

INUVIK - TUKTOYAKTUK HIGHWAY CONSTRUCTION PLAN

Year One (North)

Acknowledgements: Original Drawing by KAVIK-STANTEC LTD: Base Data: Government of Canada

DISCLAIMER: All locations are approximate, please refer to the Highway Final Design for specific locations.

PREPARED BY
Northwest Territories Transportation

PREPARED FOR
KAVIK-STANTEC

FIGURE NO.
01 of 05

Last Modified: September 13, 2013 By: pethe

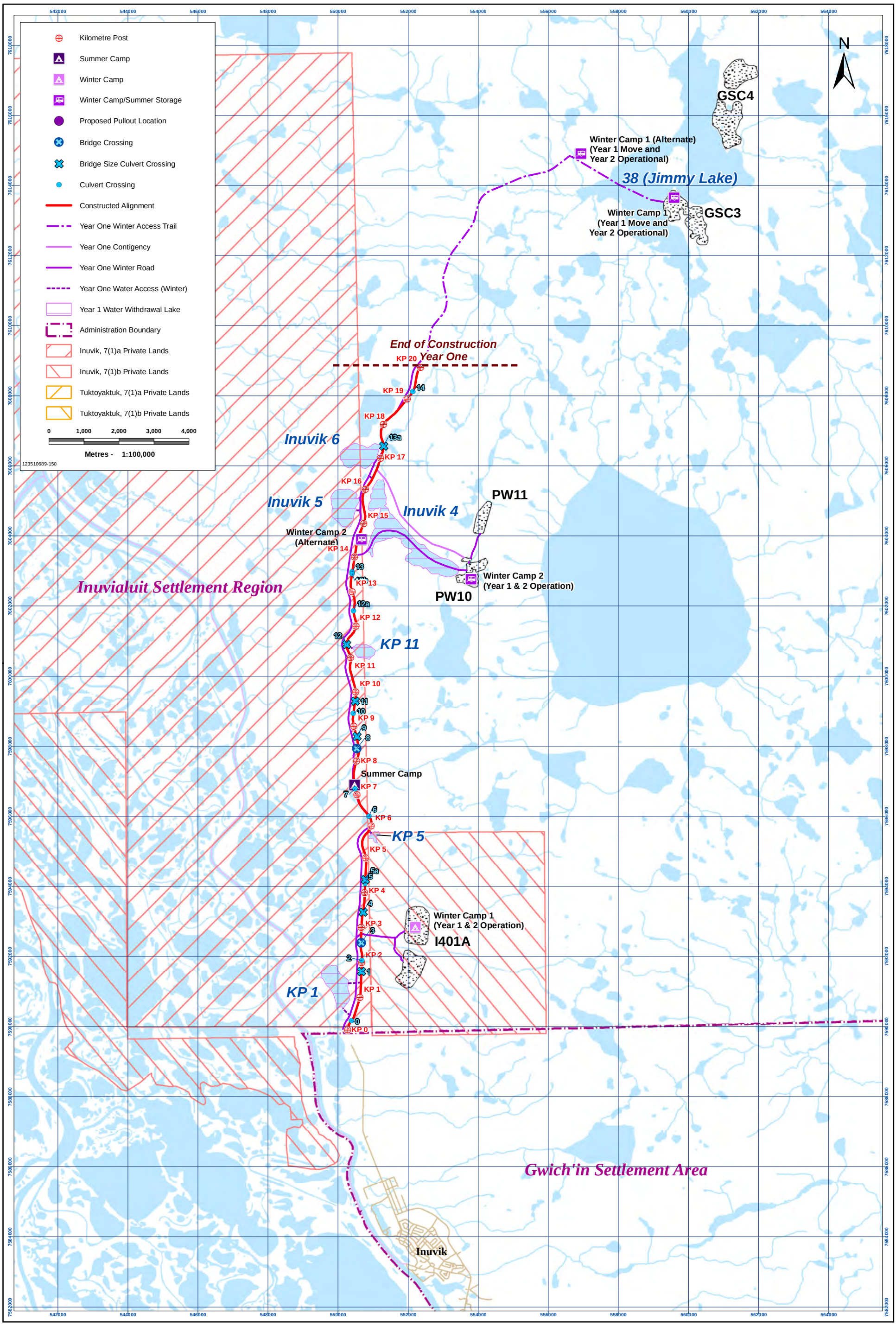

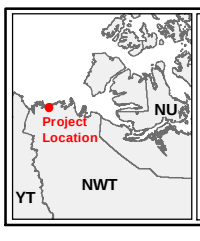

INUVIK - TUKTOYAKTUK HIGHWAY CONSTRUCTION PLAN

Year One (South)

Acknowledgements: Original Drawing by KAVIK-STANTEC LTD: Base Data: Government of Canada

DISCLAIMER: All locations are approximate, please refer to the Highway Final Design for specific locations.

PREPARED BY
Northwest Territories Transportation

PREPARED FOR
KAVIK-STANTEC

FIGURE NO.
02 of 05

Last Modified: September 20, 2013 By: cthibodeau

Kilometre Post
Bridge Crossing
Bridge Size Culvert Crossing
Culvert Crossing
Summer Camp
Winter Camp/Summer Storage
Proposed Pullout Location
Constructed Alignment
Year Two Winter Road
Year Two Winter Access Trail
Year Two Water Access (Winter)
Year 2 Water Withdrawal Lake
Inuvik, 7(1)a Private Lands
Inuvik, 7(1)b Private Lands
Tuktoyaktuk, 7(1)a Private Lands
Tuktoyaktuk, 7(1)b Private Lands

0 1,000 2,000 3,000 4,000

Metres - 1:100,000

123510689-151

N

KP 103
KP 102
KP 101
KP 100
KP 99
KP 98
KP 97
KP 96
KP 95
KP 94
KP 93
KP 92
KP 91
KP 90
KP 89
KP 88
KP 87
KP 86
KP 85
KP 84
KP 83
KP 82
KP 81
KP 80

Winter Camp 2
(Year 1 and Year 2 Operation)
170

Summer Camp

A9
A10
A11
A12
A13
35a
34c
34b
34a2
34a

KP 86
KP 91
KP 85
KP 82A
KP 82B
KP 101
KP 100

Year 2
173/305

174
Winter Camp 1
(Year 1 Move and
Year 2 & 3 Operational)

Summer Camp

End of Construction
Year Two

309
Winter Camp 2
(Year 2 Move and
Year 3 Operation)

312 West
Winter Camp 1
(Year 2 Move and
Year 3 & 4 Operation)

556000 558000 560000 562000 564000 566000 568000 570000 572000 574000 576000 578000

7674000 7672000 7670000 7668000 7666000 7664000 7662000 7660000 7658000 7656000 7654000 7652000 7650000 7648000 7646000 7644000 7642000 7640000

Project Location
NU
NWT
YT

INUVIK - TUKTOYAKTUK HIGHWAY CONSTRUCTION PLAN

Year Two (North)

Acknowledgements: Original Drawing by KAVIK-STANTEC LTD: Base Data: Government of Canada

DISCLAIMER: All locations are approximate, please refer to the Highway Final Design for specific locations.

PREPARED BY
Northwest Territories Transportation

PREPARED FOR
KAVIK-STANTEC

FIGURE NO.
03 of 05

Last Modified: September 19, 2013 By: jpetho

Kilometre Post
Summer Camp
Winter Camp/Summer Storage
Proposed Pullout Location
Bridge Crossing
Bridge Size Culvert Crossing
Culvert Crossing
Constructed Alignment
Year Two Water Access (Winter)
Year Two Winter Road
Year Two Winter Access Trail
Year 2 Water Withdrawal Lake
Inuvik, 7(1)a Private Lands
Inuvik, 7(1)b Private Lands
Tuktoyaktuk, 7(1)a Private Lands
Tuktoyaktuk, 7(1)b Private Lands

0 1,250 2,500 3,750 5,000

Metres - 1:130,000

123510689-152

N

PW19A
Camp 3 (Year 2 Move and Year 3 Operational)
PW18
Winter Camp 2 (Year 2 and Year 3 Operational)
314/325
End of Construction Year Two
KP 40
KP 39
KP 38
KP 37
22b
KP 36
KP 35
Summer Camp
KP 34
KP 33
35
KP 32
22a
KP 31
37
KM 30.9
KM 30.2
29B
KP 30
21a
GSC4
29A
KP 29
KP 28
Winter Camp 1 (Alternate) (Year 1 Move and Year 2 Operational)
KP 27
21
KP 26
20a
19
18
13a
20
28 (Jimmy Lake)
KP 25
17a
Winter Camp 1 (Year 1 Move and Year 2 Operational)
GSC3
KP 24
KP 24
17
KP 23
16
15C
15B
15A
KP 22
KP 21
KP 20
KP 19
KP 18
Summer Camp
KP 17
KP 16
PW11
KP 15
Camp 2 (Alternate)
KP 14
Camp 2 (Year 1 and 2)
KP 13
PW10
KP 12
KP 11
KP 10
KP 9
KP 8
KP 7
KP 6
KP 5
KP 4
KP 3
I401A
KP 2
(Year 2 Operation)
KP 1

544000 546000 548000 550000 552000 554000 556000 558000 560000 562000 564000 566000 568000 570000 572000 574000

7636000 7634000 7632000 7630000 7628000 7626000 7624000 7622000 7620000 7618000 7616000 7614000 7612000 7610000 7608000 7606000 7604000 7602000 7600000 7598000 7596000 7594000 7592000 7590000

Project Location
NU
NWT
YT

INUVIK - TUKTOYAKTUK HIGHWAY CONSTRUCTION PLAN

Year Two (South)

Acknowledgements: Original Drawing by KAVIK-STANTEC LTD: Base Data: Government of Canada

DISCLAIMER: All locations are approximate, please refer to the Highway Final Design for specific locations.

PREPARED BY Northwest Territories Transportation

PREPARED FOR KAVIK-STANTEC

FIGURE NO. 04 of 05

Last Modified: September 20, 2013 By: dbrown

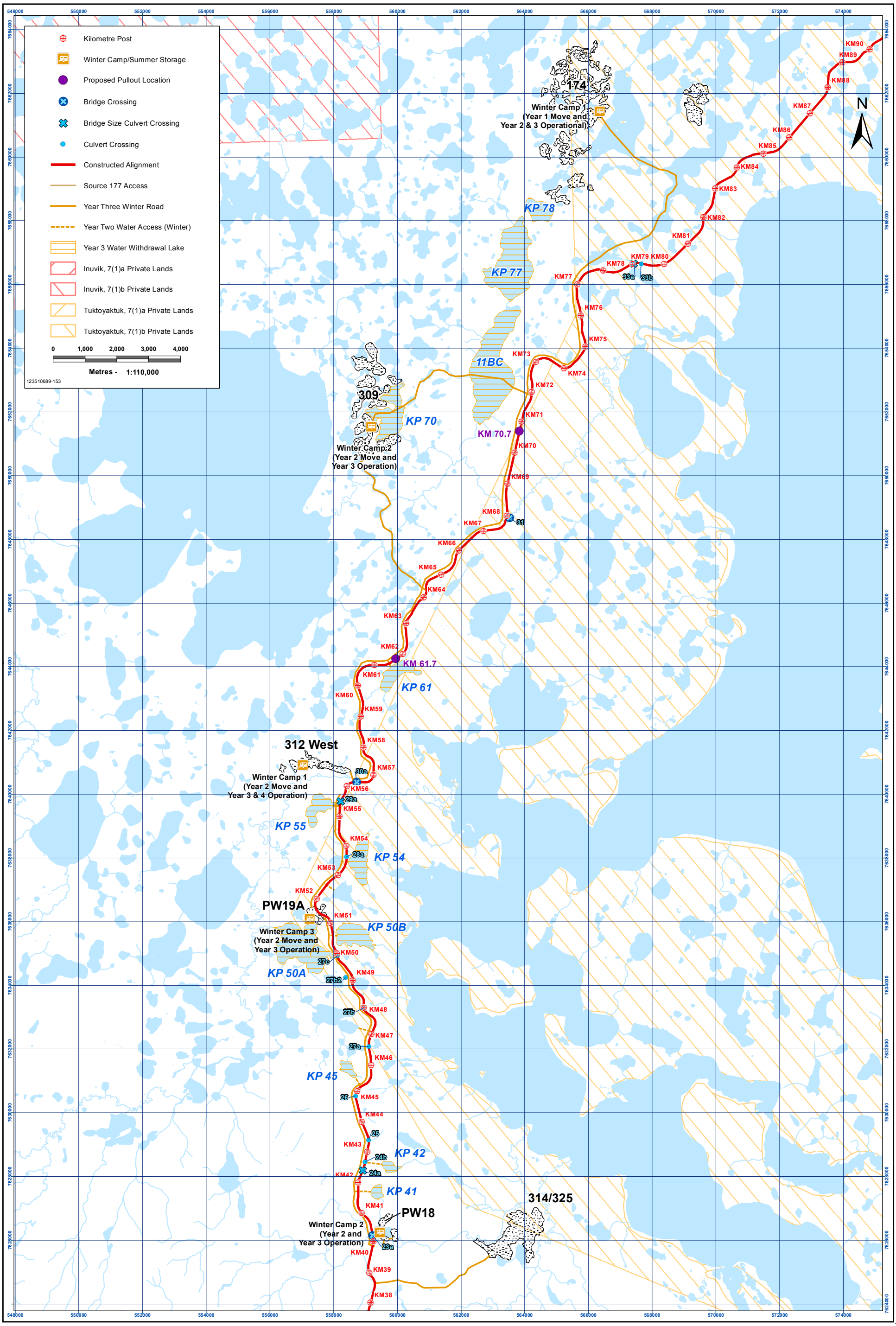

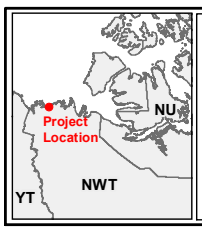

INUVIK - TUKTOYAKTUK HIGHWAY CONSTRUCTION PLAN

Year Three (North, South)

Acknowledgements: Original Drawing by KAVIK-STANTEC LTD: Base Data: Government of Canada

DISCLAIMER: All locations are approximate, please refer to the Highway Final Design for specific locations.

PREPARED BY
Northwest Territories Transportation

PREPARED FOR
KAVIK-STANTEC

FIGURE NO.
05 of 05

Last Modified: September 20, 2013 By: CThibodeau

APPENDIX B:

SITE PHOTOGRAPHS

Photo 1: Preparation for blasting within an area of Borrow Source #174

Photo 2: Drilling of blast holes in frozen granular fill at Borrow Source #174

Photo 3: Collection of bulk frozen granular fill sample at Borrow Source # 174

Photo 4: Hauling of frozen granular fill with rock truck from borrow source

Photo 5: Test site prior to start of construction (looking north)

Photo 6: Placement of fill over thermistor string TS-C2

Photo 7: End-dumping of loose lifts of frozen granular fill

Photo 8: Breakdown and compaction of frozen granular fill with dozer and vibratory roller

Photo 9: Compaction of frozen granular fill with vibratory roller

Photo 10: Preparation for SAA instrumentation installation. (embankment construction progress visible in background)

Photo 11: DTH drill rig used for drilling of holes for vertical SAA and vertical thermistor string installation

Photo 12: Materials jettisoned to surface by forced air during drilling with DTH rig

Photo 13: Materials adjacent to drill hole following DTH drilling

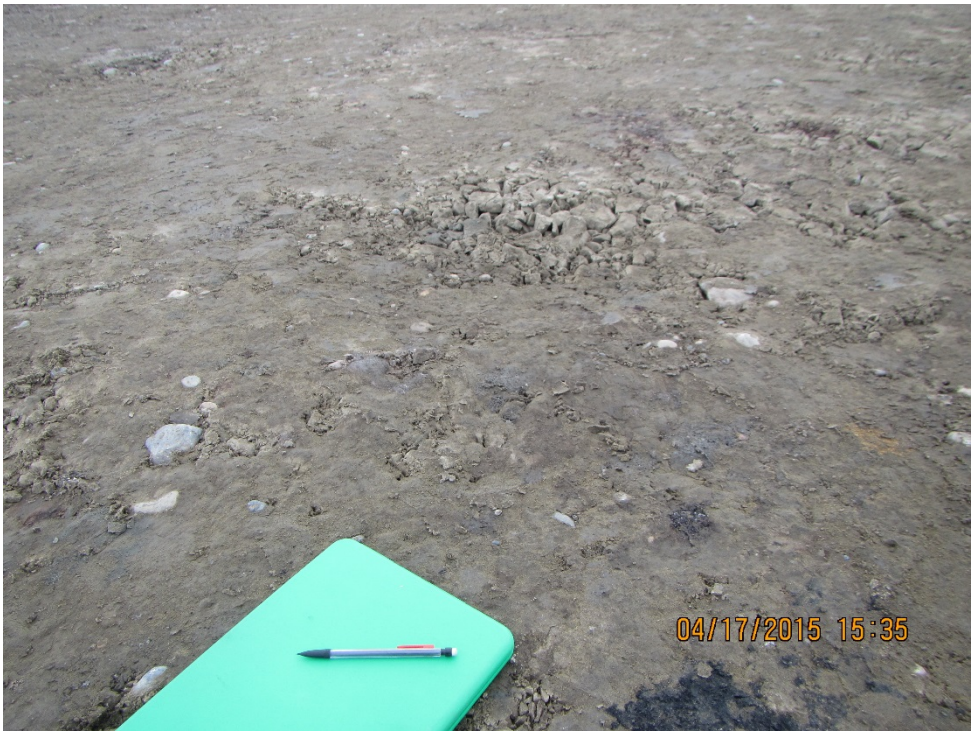

Photo 14: Typical surface of frozen granular fill lift following compaction (notebook shown for scale)

Photo 15: Typical type Nf (non-visible ice, poorly bonded or friable) frozen soils, as delivered to site

Photo 16: Typical type Nbe (Non-visible ice, well-bonded, excess ice) and Nbn (Non-visible ice, well-bonded, no excess ice), as delivered to site

Photo 17: Supernatant water at soil surface following thawing at end of construction

Photo 18: Typical type Nbn (non-visible ice, well-bonded, no excess ice) soil chunk following thawing

Photo 19: Typical type Vx (visible ice) frozen soil (see visible ice crystal inclusion)

Photo 20: Thawing of exposed compacted fill surface on April 19

Photo 21: Protective conduits for instrumentation being covered with protective fill layer

Photo 22: Completed test embankment, see instrument data acquisition boxes in right foreground

Photo 23: Overall view of test embankment looking east 2015/07/03, (photograph courtesy of Lukas Arenson)

Photo 24: Overall view of test embankment looking southeast 2015/07/03, (photograph courtesy of Lukas Arenson)

Photo 25: Overall view of test embankment looking south 2015/07/03, (photograph courtesy of Lukas Arenson)

Photo 26: Longitudinal cracking along crest of test embankment 2015/07/03, (photograph courtesy of Lukas Arenson)

APPENDIX C:

THERMAL MODEL OUTPUT FIGURES

Reference Guide for Figures C-01 to C-10

- Each figure corresponds to a specific date over the study period, as indicated in upper left-hand corner of each figure.

- Temperature-sensing nodes are shown as small black circles. Measured temperatures from the date referenced in the figure are shown in black text, adjacent to the node locations. Units are in °C.

- Coloured background represents results of the post-construction thermal model for the date referenced in the figure. Temperature contours range from blue (coldest) to red (warmest), separated by thin black contour lines shown at intervals of 2 °C. The contour line corresponding to the 0° C isotherm is shown as a dotted blue line for emphasis. Contour labels for the modelled temperatures are shown as black values within white boxes.

- Measured cumulative deformations from the SAAs are shown in each figure.

- The baseline readings are represented by a horizontal line for SAA-CH, and a vertical line for SAA-CV, representing the shape and location of the SAAs within the embankment cross-section. The measured cumulative deformations are shown to-scale as segmented black lines representing the deformed SAAs, with black dots representing the SAA temperature-sensing node locations.

Figure C-01

Measured Temperatures and Deformations,
and Thermal Model Contours for
2015/04/20

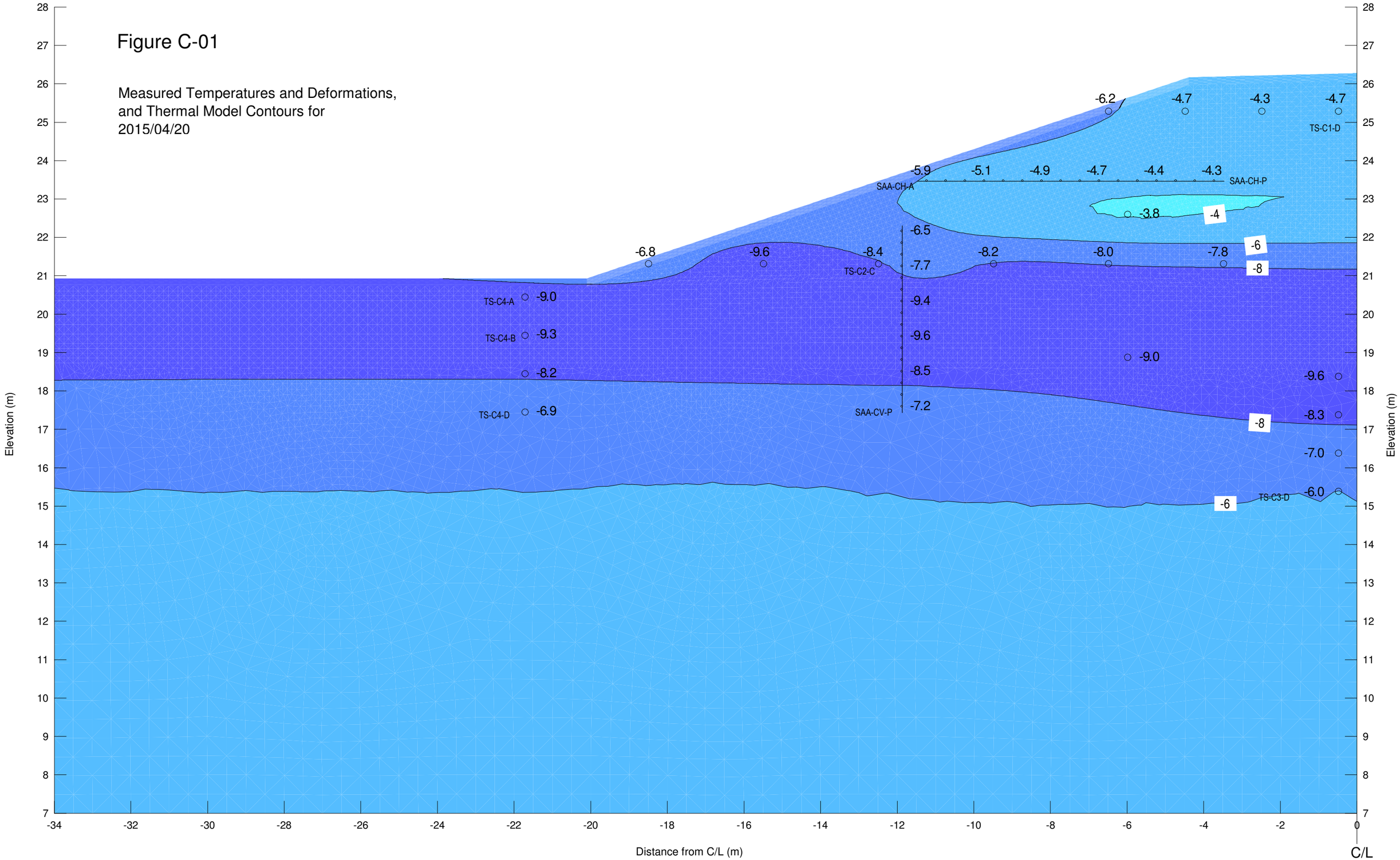

Figure C-02

Measured Temperatures and Deformations,
and Thermal Model Contours for
2015/05/02

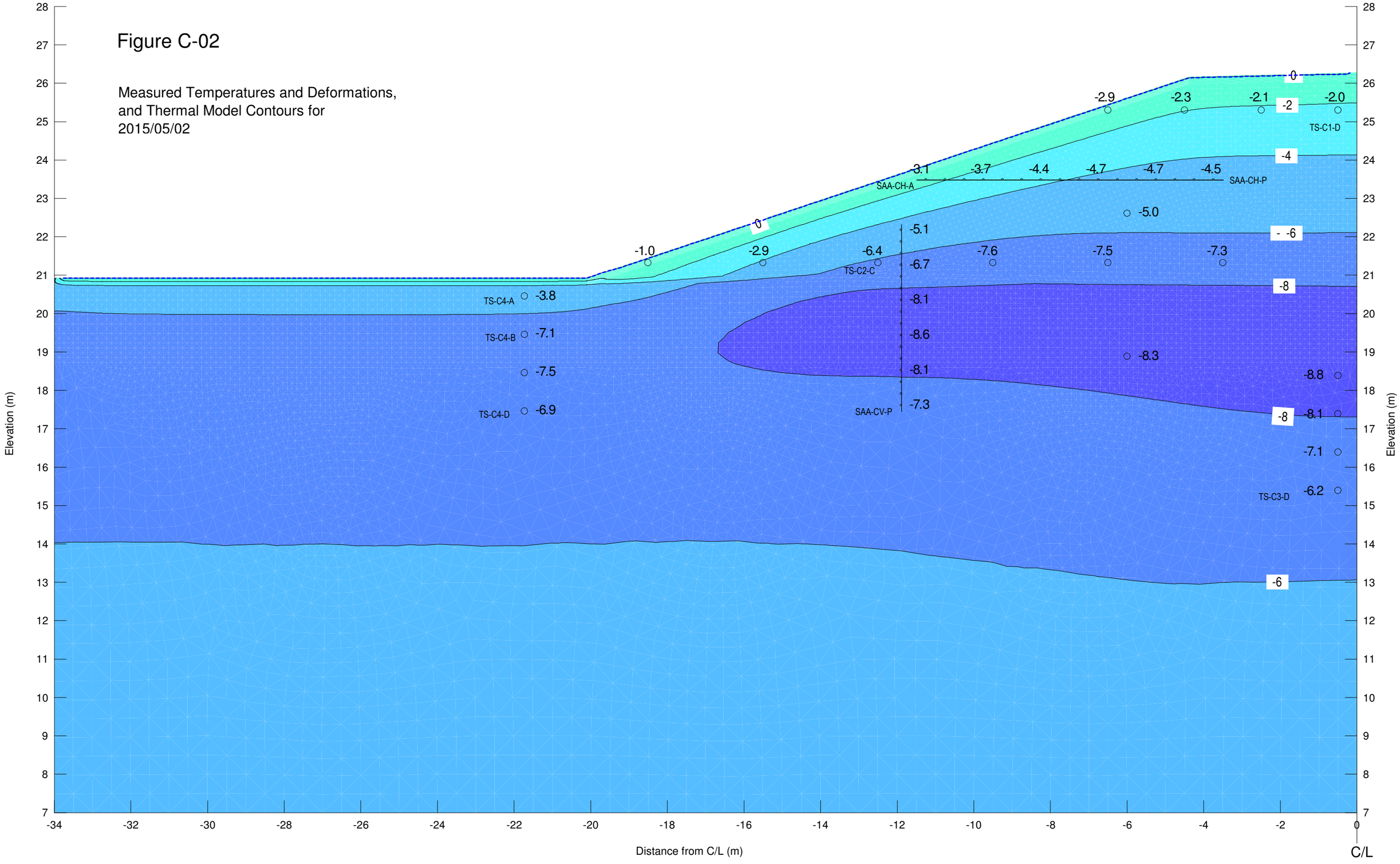

Figure C-03

Measured Temperatures and Deformations,
and Thermal Model Contours for
2015/05/23

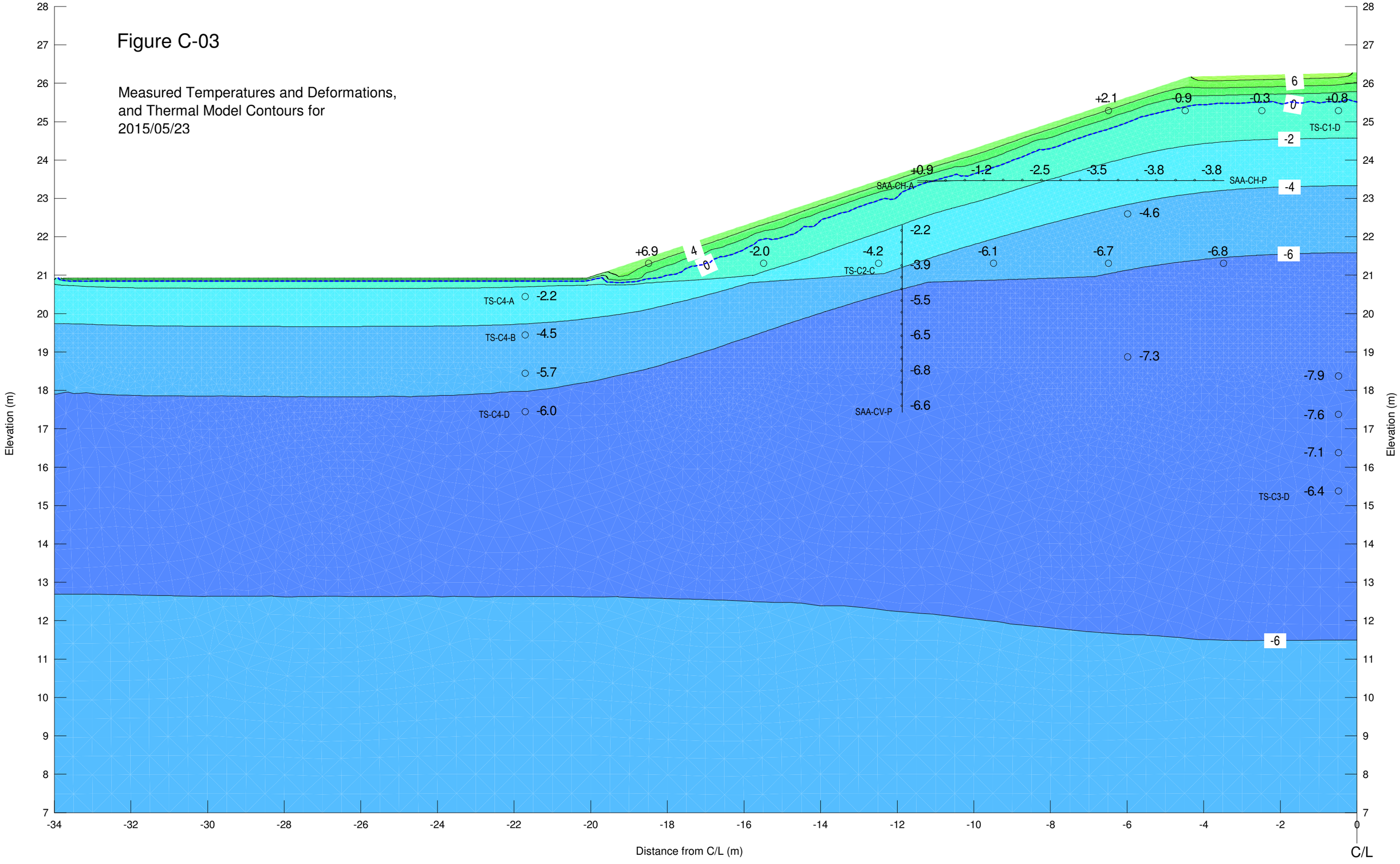

Figure C-04

Measured Temperatures and Deformations,
and Thermal Model Contours for
2015/06/13

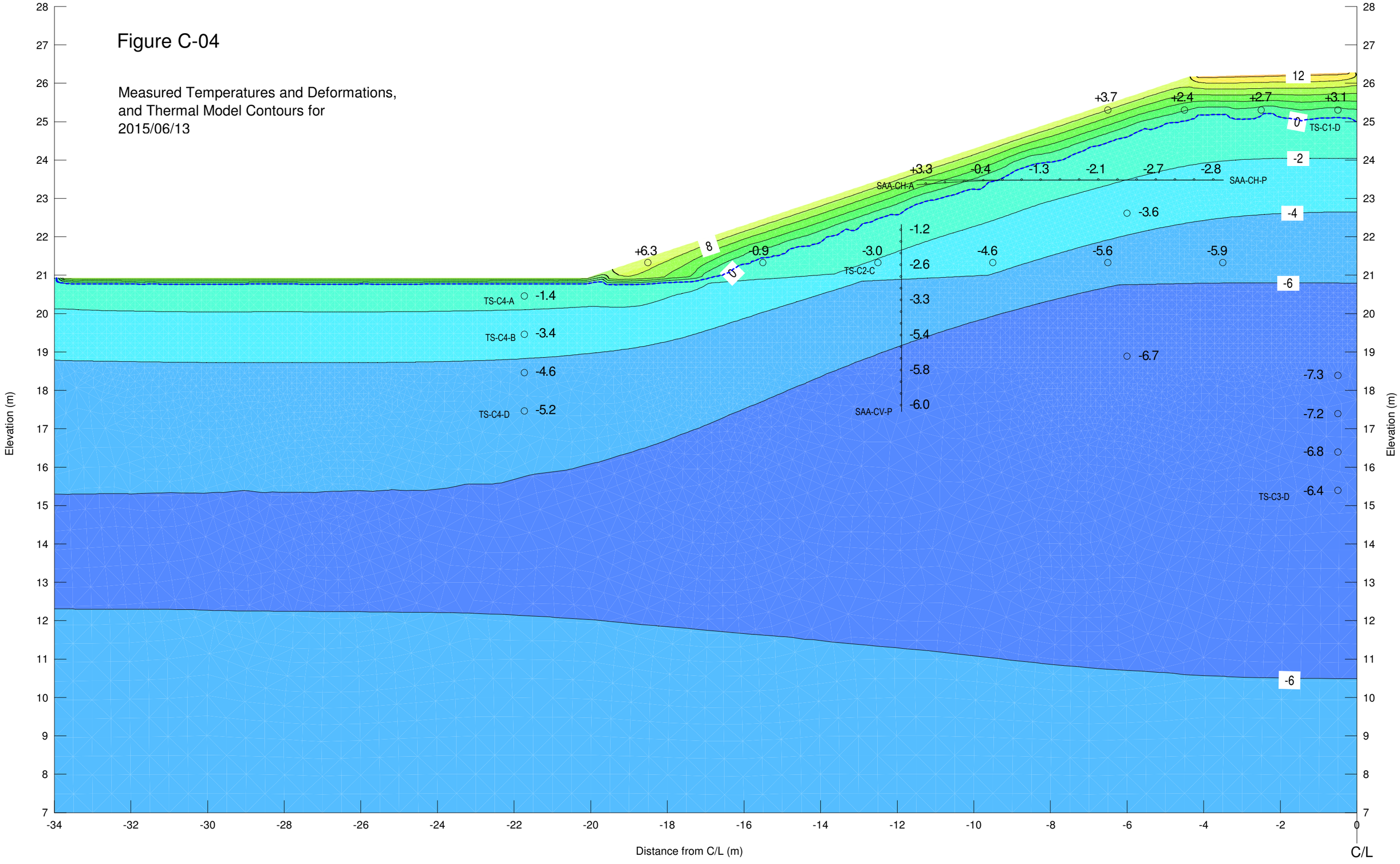

Figure C-05

Measured Temperatures and Deformations,
and Thermal Model Contours for
2015/07/04

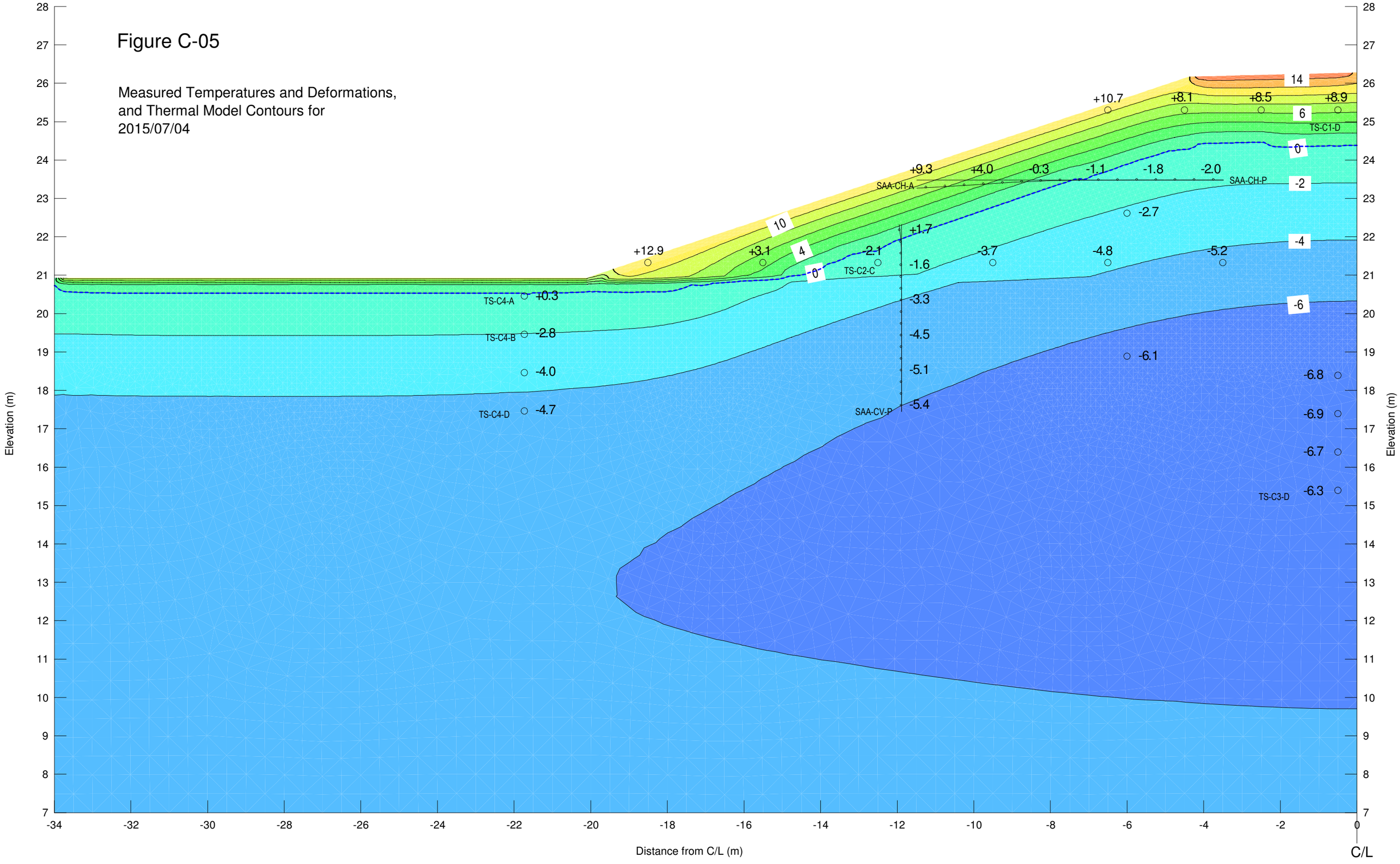

Figure C-06

Measured Temperatures and Deformations,
and Thermal Model Contours for
2015/07/25

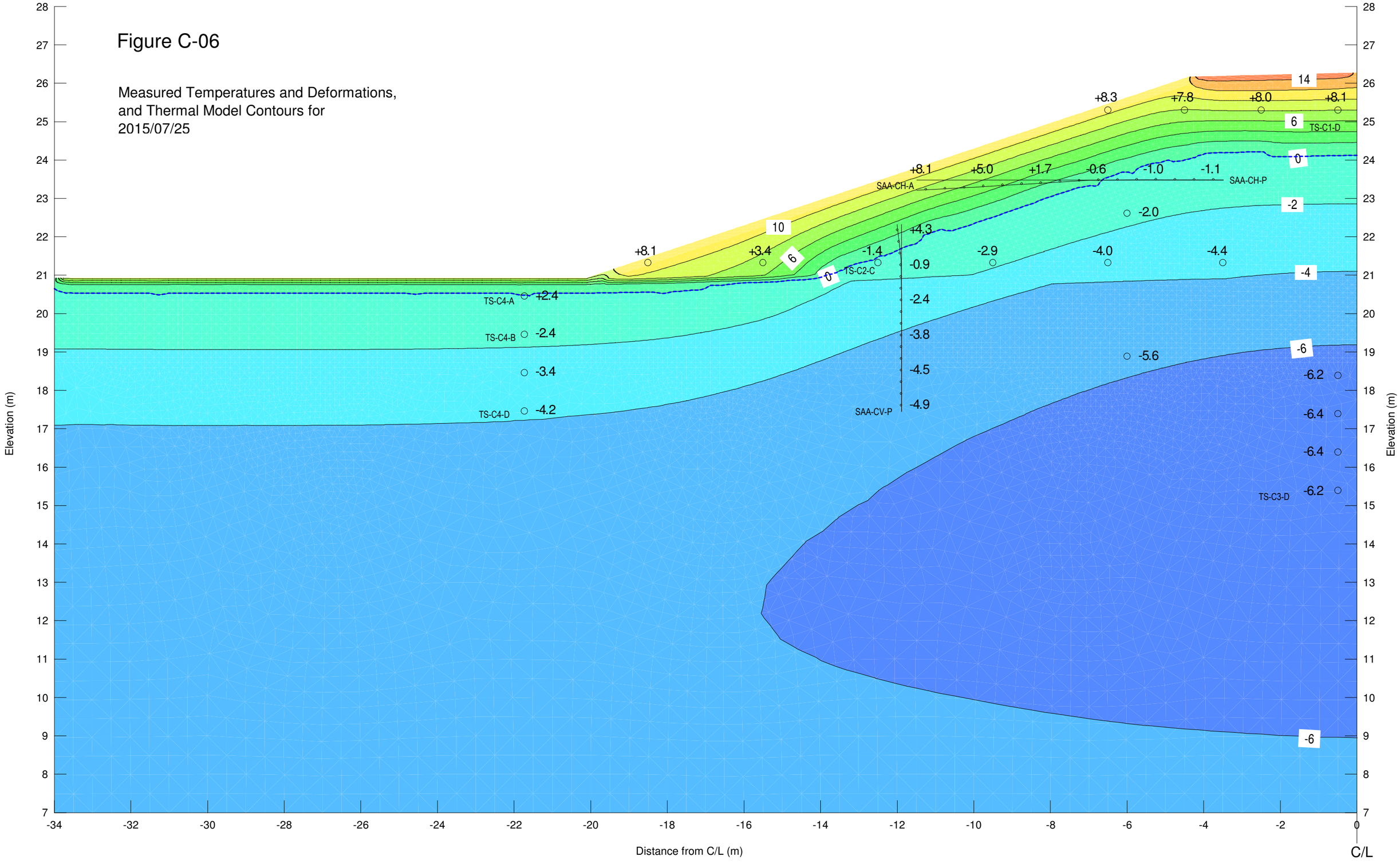

Figure C-07

Measured Temperatures and Deformations,
and Thermal Model Contours for
2015/08/15

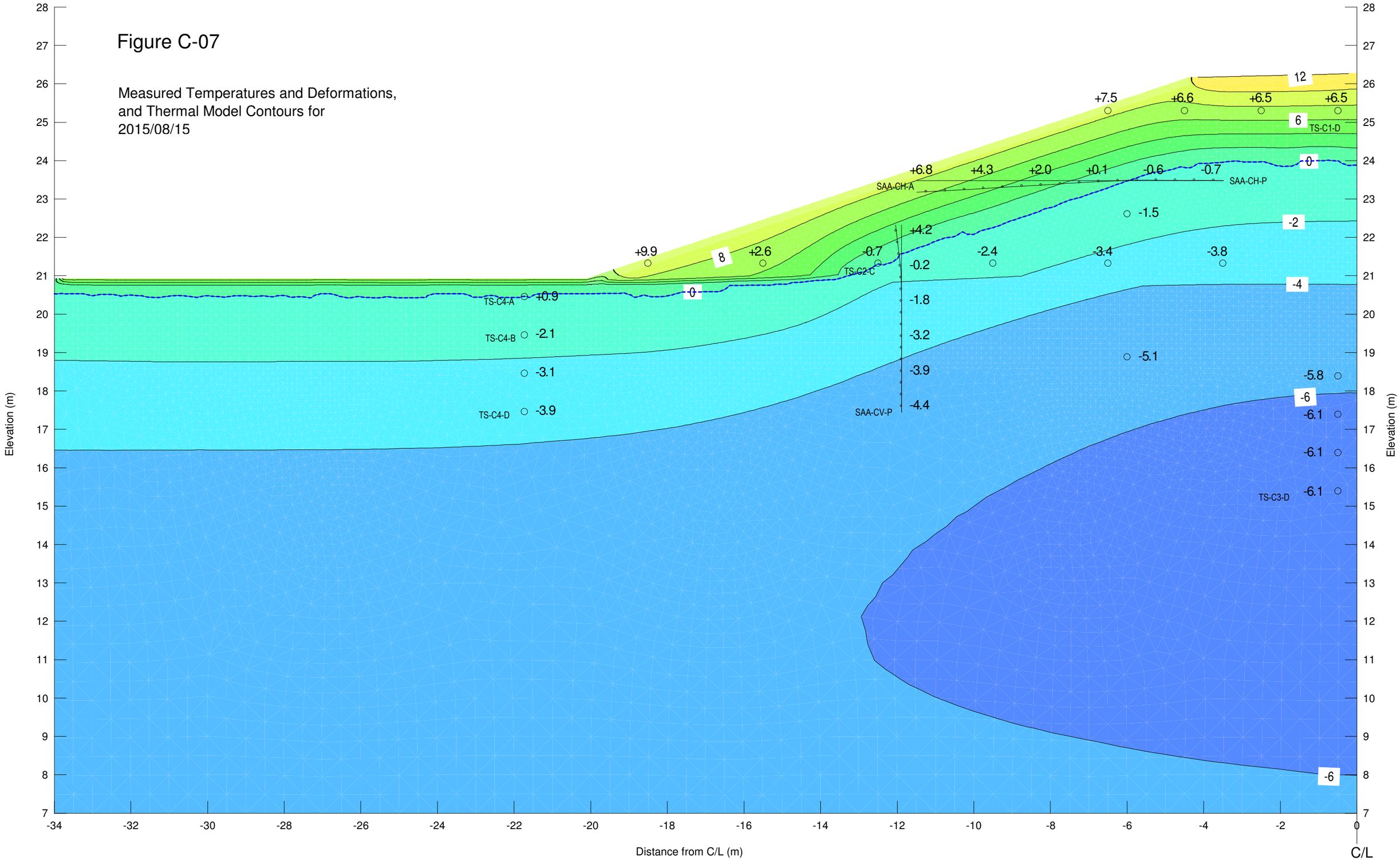

Figure C-08

Measured Temperatures and Deformations,
and Thermal Model Contours for
2015/09/05

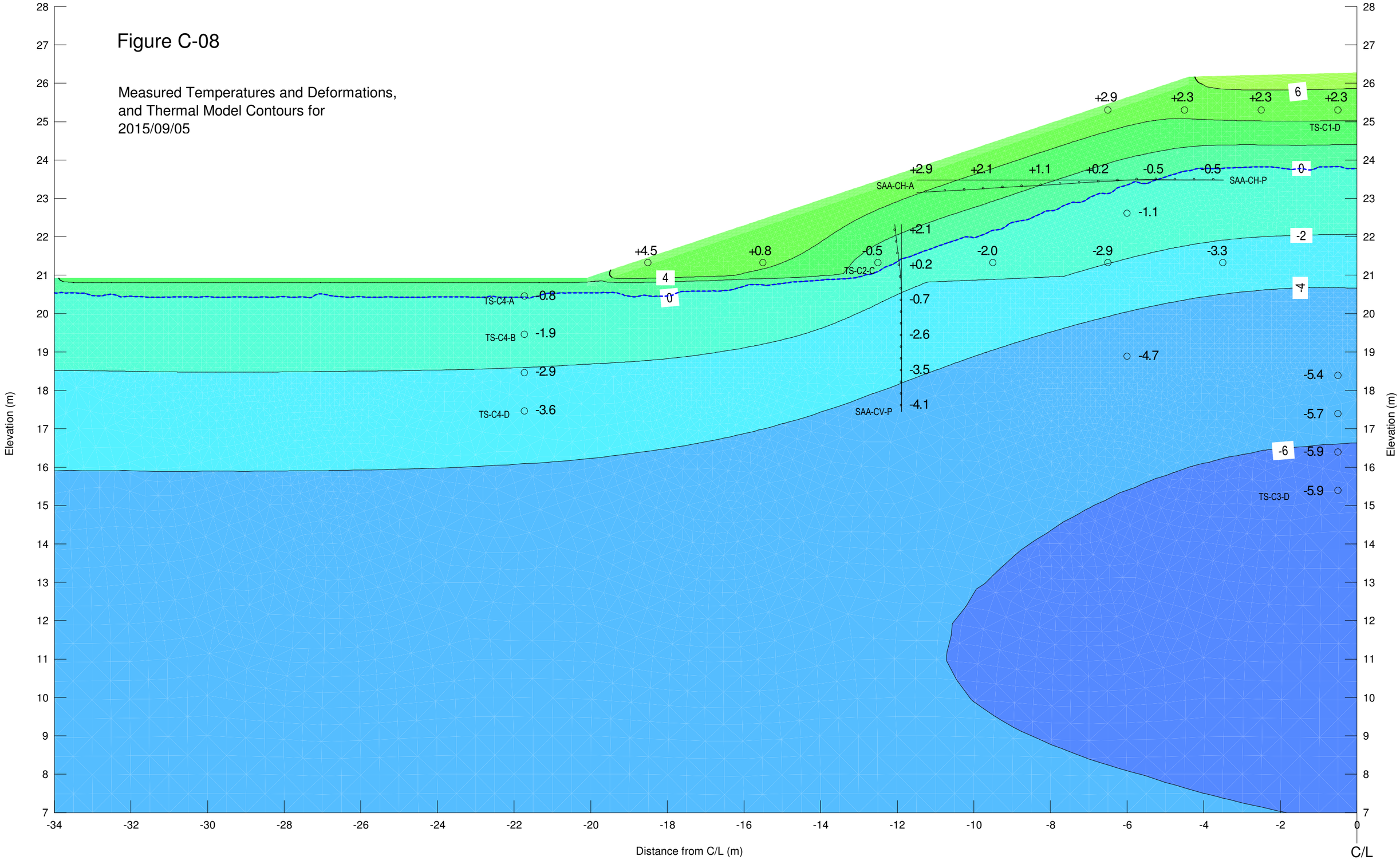

Figure C-09

Measured Temperatures and Deformations,
and Thermal Model Contours for
2015/09/26

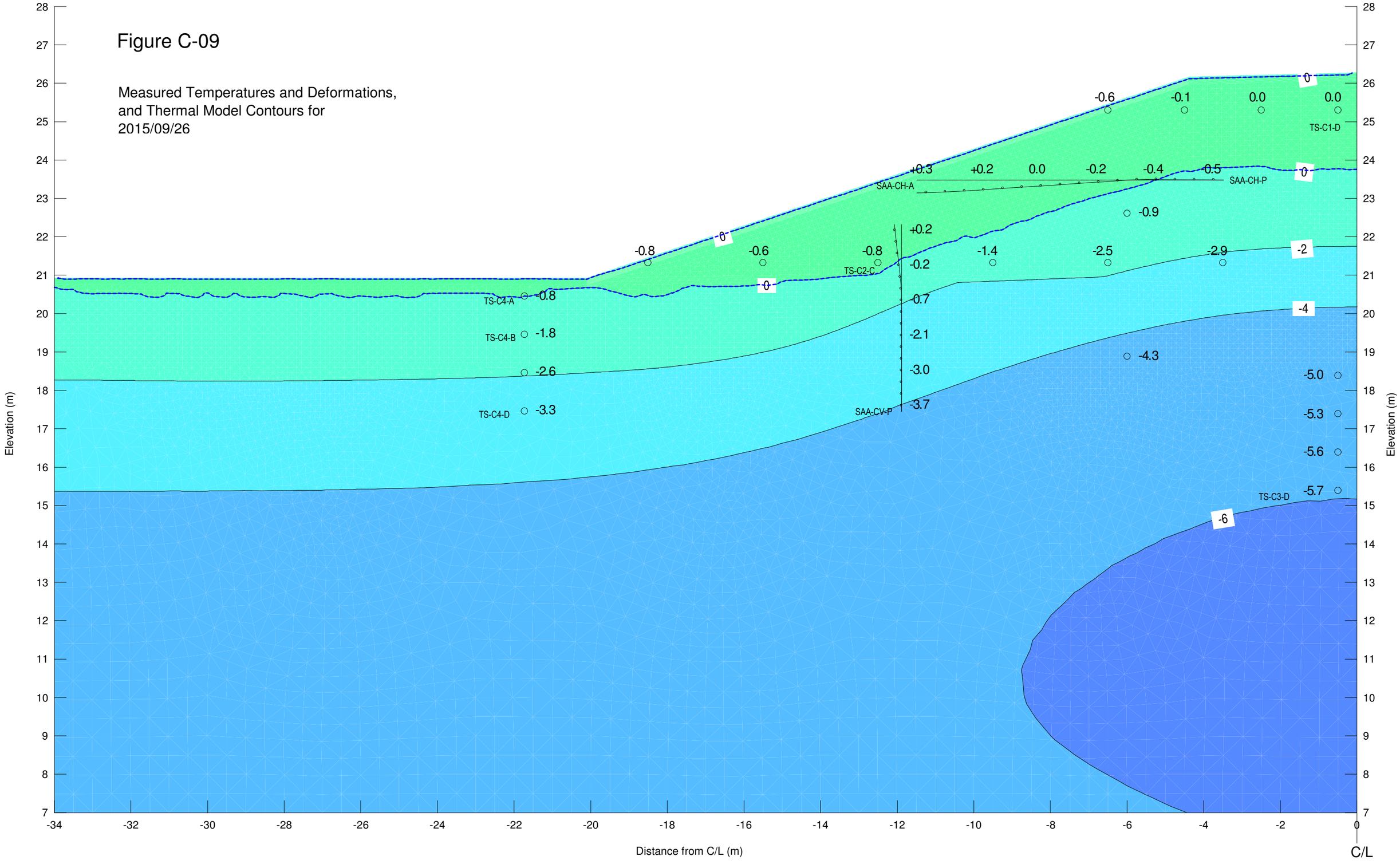

Figure C-10

Measured Temperatures and Deformations,
and Thermal Model Contours for
2015/10/05